

MODULES FOR EXPERIMENTS IN STELLAR ASTROPHYSICS (MESA): GIANT PLANETS, OSCILLATIONS, ROTATION, AND MASSIVE STARS

BILL PAXTON¹, MATTEO CANTIello¹, PHIL ARRAS², LARS BILDSTEN^{1,3}, EDWARD F. BROWN⁴, AARON DOTTER⁵, CHRISTOPHER MANKOVICH³, M. H. MONTGOMERY⁶, DENNIS STELLO⁷, F. X. TIMMES⁸, AND RICHARD TOWNSEND⁹

submitted to The Astrophysical Journal Supplement Series

ABSTRACT

We substantially update the capabilities of the open source software package Modules for Experiments in Stellar Astrophysics (MESA), and its one-dimensional stellar evolution module, MESA star. Improvements in MESA star's ability to model the evolution of giant planets now extends its applicability down to masses as low as one-tenth that of Jupiter. The dramatic improvement in asteroseismology enabled by the space-based *Kepler* and *CoRoT* missions motivates our full coupling of the ADIPLS adiabatic pulsation code with MESA star. This also motivates a numerical recasting of the Ledoux criterion that is more easily implemented when many nuclei are present at non-negligible abundances. This impacts the way in which MESA star calculates semi-convective and thermohaline mixing. We exhibit the evolution of 3–8 M_⊙ stars through the end of core He burning, the onset of He thermal pulses, and arrival on the white dwarf cooling sequence. We implement diffusion of angular momentum and chemical abundances that enable calculations of rotating-star models, which we compare thoroughly with earlier work. We introduce a new treatment of radiation-dominated envelopes that allows the uninterrupted evolution of massive stars to core collapse. This enables the generation of new sets of supernovae, long gamma-ray burst, and pair-instability progenitor models. We substantially modify the way in which MESA star solves the fully coupled stellar structure and composition equations, and we show how this has improved MESA's performance scaling on multi-core processors. Updates to the modules for equation of state, opacity, nuclear reaction rates, and atmospheric boundary conditions are also provided. We describe the MESA Software Development Kit (SDK) that packages all the required components needed to form a unified and maintained build environment for MESA. We also highlight a few tools developed by the community for rapid visualization of MESA star results.

Keywords: asteroseismology — methods: numerical — planets and satellites: physical evolution — stars: evolution — stars: massive — stars: rotation

Contents

1. Introduction	2	3.1. The Solar Sound Speed Profile	6
2. Giant Planets and Low-Mass Stars	3	3.2. New Asteroseismic Capabilities in MESA	7
2.1. Construction of Starting Models	4	3.3. The Effect of Composition Gradients on the Brunt-Väisälä Frequency	9
2.2. Evolutionary Calculations	4	4. Mixing Mechanisms Involving Composition Gradients	10
2.3. Implementation of Inert Cores	5	4.1. Semiconvection	10
2.4. Irradiation	5	4.2. Thermohaline Mixing	10
2.5. Low-Mass Main Sequence Stars	6	4.3. Impact of Mixing on Convective Core Hydrogen and Helium Burning	11
3. Asteroseismology	6	5. Evolution beyond the Main Sequence and White Dwarfs	11
		5.1. Code Comparisons during Helium Core Burning	11
		5.2. Making and Cooling White Dwarfs	12
		5.3. Compressional Heating and Accretion	16
		6. Rotation	17
		6.1. Implementation of Shellular Rotation	17
		6.2. Magnetic Fields	18
		6.3. Rotationally-Enhanced Mass Loss	18
		6.4. Test Cases: 15 M _⊙ and 25 M _⊙	18
		6.5. Rapidly Rotating Massive Stars	19
		7. Massive Stellar Evolution	19
		7.1. Evolution of Massive Stars with MESA	19
		7.2. Treatment of Superadiabatic Convection in Radiation-Dominated Regions	25

matteo@kitp.ucsb.edu

¹ Kavli Institute for Theoretical Physics, University of California, Santa Barbara, CA 93106, USA

² Department of Astronomy, University of Virginia, P.O. Box 400325, Charlottesville, VA 22904-4325, USA

³ Department of Physics, University of California, Santa Barbara, CA 93106, USA

⁴ Department of Physics and Astronomy, National Superconducting Cyclotron Laboratory, and Joint Institute for Nuclear Astrophysics, Michigan State University, East Lansing, MI 48864, USA

⁵ Research School of Astronomy and Astrophysics, The Australian National University, Weston, ACT 2611, Australia

⁶ Department of Astronomy and McDonald Observatory, University of Texas, Austin, TX 78712, USA

⁷ Sydney Institute for Astronomy (SIfA), School of Physics, University of Sydney, NSW 2006, Australia

⁸ School of Earth and Space Exploration, Arizona State University, Tempe, AZ 85287, USA

⁹ Department of Astronomy, University of Wisconsin-Madison, Madison, WI 53706, USA

7.3. Core-Collapse Progenitor Models	26
7.4. Radial Instability of Red Supergiants	27
8. Summary and Conclusions	28
A. Updates to Input Physics Modules	29
A.1. Atomic and Nuclear Data	29
A.2. Equation of State	30
A.3. Opacities	30
A.4. Nuclear Reactions	31
A.5. Atmosphere Boundary Conditions	32
B. Nuts and Bolts	32
B.1. Evolve a Step	32
B.2. Solving the Coupled Structure, Burn, and Mix Equations	33
B.3. Timestep Controls	34
B.4. Mesh Controls	35
B.5. Mass Adjustment	36
B.6. Evolving the Angular Velocity	36
B.7. Nuclear Reactions	37
B.8. Multicore Performance	37
B.9. Operating System and Compiler Considerations	38
B.10. Visualization	39
C. The MESA Software Development Kit	39

1. INTRODUCTION

As the most commonly observed objects, stars remain at the forefront of astrophysical research. Advances in optical detector technology, computer processing power, and data storage capability have enabled new sky surveys (e.g., the Sloan Digital Sky Survey; York et al. 2000); triggered many new optical transient surveys, such as the Palomar Transient Factory (Law et al. 2009) and Pan-STARRS1 (Kaiser et al. 2010); and allowed for space missions (e.g., *Kepler*; Koch et al. 2010) that continuously monitor more than 100,000 stars. The stellar discoveries from these surveys include revelations about rare stars, unusual explosive outcomes, and remarkably complex binaries. The immediate future holds tremendous promise, as both the space-based survey *Gaia* (de Bruijne 2012; Liu et al. 2012) and the ground based Large Synoptic Survey Telescope (LSST; Ivezić et al. 2008) come to fruition.

These developments have created a new demand for a reliable and publicly available research and education tool in computational stellar astrophysics. We introduced the open source community tool MESA (Paxton et al. 2010, hereafter Paper I) to meet these new demands. This first “instrument” paper described the design and implementation of MESA modules for numerics, microphysics, and macrophysics, and introduced the stellar evolution module, MESA star. We presented a multitude of tests and code comparisons that served as our initial verification and demonstrated MESA star’s initial capabilities. Since Paper I, MESA has attracted over 500 registered users, witnessed over 5,000 downloads from <http://mesa.sourceforge.net/>, started an annual Summer School program, and provided a portal (<http://mesastar.org>) for the community to openly share knowledge (e.g., the specific settings for a published MESA star run), codes, and publications.

This paper describes the major new MESA capabilities for modeling giant planets, asteroseismology, and the treatment of rotation and evolution of massive stars. We also describe

numerous advances since Paper I. These include the incorporation of composition gradients in the determination of convective mixing and additional verification for evolution of intermediate mass stars and the white dwarfs they create.

Our improvements to MESA star for gas giant planets were motivated by the dramatic growth in this field. Over 800 exoplanets have been confirmed, and their study has prompted enormous progress in our understanding of the formation and migration of giant planets, and of the importance of factors such as stellar mass (Laughlin et al. 2004; Alibert et al. 2011; Boss 2011), composition (Fischer & Valenti 2005; Young et al. 2012), and binarity (Patience et al. 2002; Mugrauer & Neuhäuser 2009; Roell et al. 2012). Puzzles remain, though, both in our solar system and in the studies of the plethora of these newly discovered exoplanets, including the characteristics of the planet-hosting stars and the interiors, atmospheres, surface gravities, temperatures, and compositions of the planets (e.g., Udry & Santos 2007; Seager & Deming 2010). Many of these variations can now be numerically explored, as can the incorporation of an inert core in an otherwise regular gas giant and the impact of irradiation.

The ability to infer stellar properties (e.g., mass, radius, internal state, and rotation) from measurements of the radial and non-radial oscillation modes has been dramatically improved by two space-based optical telescopes (Convection Rotation and Planetary Transits, *CoRoT*; Baglin et al. 2009 and *Kepler*; Borucki et al. 2009). The high cadences and precision (often better than ten parts per million) reveal and accurately measure multitudes of oscillation frequencies for over 10,000 stars, substantially raising the need for accurate and efficient computations of stellar mode frequencies and the resulting eigenfunctions. The intrinsic flexibility of MESA star allows for the exploration of model-space required to precisely infer stellar properties from the observed frequencies.

An important new addition to MESA is the incorporation of stellar rotation and magnetic fields in radiative regions. As stars are not solid bodies, they undergo radial differential rotation (Thompson et al. 2003; Balbus et al. 2012) and also rotate at different angular velocities at different latitudes (Ruediger et al. 1998; Bonanno et al. 2007; Küker et al. 2011). These rotational shears have a significant impact on the evolution of the stellar magnetic field. Despite the resulting 3D nature of magnetism and rotation, the stellar evolution community has come a long way in understanding stars with 1D simulations (Meynet & Maeder 1997; Langer et al. 1999; Maeder & Meynet 2000b; Heger & Langer 2000; Hirschi et al. 2004; Cantiello & Langer 2010), thus motivating our need to fully incorporate rotation within MESA. The new flexibility in angular momentum transport mechanisms allows for numerical exploration of alternate rotational outcomes should the observations (e.g., asteroseismology) require it.

The paper is outlined as follows. Section 2 describes the new capability of MESA to evolve models of giant planets, while §3 discusses the new asteroseismology capabilities. The MESA implementation of composition gradients in stellar interiors and their impact on convective mixing is described in §4. The status of the evolution of intermediate mass stars and the MESA star construction and evolution of white dwarfs is described in §5. The new capabilities for evolving rotating stars is described in §6. The onset of near Eddington luminosities and radiation pressure dominance in the envelopes of evolving massive stars has been a challenge for many stellar evolution codes ever since the realization of the iron opacity bump at $\log T \approx 5.3$ (Iglesias et al. 1992). We discuss

in §7 the resulting improvements for evolving massive stars. This allows for the uninterrupted evolution of rotating massive stars to the onset of core collapse. We conclude in §8 by highlighting where additional improvements to MESA are likely to occur in the near future. Appendix A describes the many improvements to the physics modules since Paper I; Appendix B presents “nuts and bolts” information on the primary components of evolution calculations; and Appendix C presents the MESA Software Development Kit (SDK). All of our symbols are defined in Table 1. We denote components of MESA, such as modules and routines, in Courier font, e.g., `evolve_star`.

Table 1
Variable Index.

Name	Description	First Appears
<i>A</i>	atomic mass number	Section A.1
Δ_i	mass excess of the <i>i</i> th isotope	Section A.1
η	wind mass loss coefficient	Section 5.2
F_\star	day-side flux incident on an irradiated planet	Section 2.4
Γ	Coulomb coupling parameter	Section 5.2
<i>i</i>	specific angular momentum	Section B.6
κ	opacity	Section 2.1
<i>L</i>	stellar luminosity	Section 3.2
<i>m</i>	Lagrangian mass coordinate	Section 2.1
<i>M</i>	stellar mass	Section 2.1
<i>N</i>	Brunt-Väisälä frequency	Section 3.3
n_i	number density of the <i>i</i> th isotope	Section A.1
ν	turbulent viscosity	Section B.6
<i>r</i>	radial coordinate	Section 2.4
<i>R</i>	total stellar radius	Section 2.1
ρ	baryon mass density	Section A.1
<i>S</i>	specific entropy	Section 2.1
Σ	mass column	Section 2.4
Σ_\star	depth for heating from irradiation	Section 2.4
τ	optical depth	Section 5.2
ν_c	magnitude of changes during a timestep	Section B.3
ν_t	target value for ν_c	Section B.3
<i>W</i>	atomic weight	Section A.1
<i>X</i>	H mass fraction	Section 3.2
X_i	baryon mass fraction of the <i>i</i> th isotope	Section 3.3
<i>Y</i>	He mass fraction	Section 2
Y_e	electrons per baryon (\bar{Z}/\bar{A})	Section A.1
Y_i	abundance of the <i>i</i> th isotope	Section A.1
<i>Z</i>	metallicity	Section 2
<i>Z</i>	atomic number	Section A.1
α_{MLT}	mixing length parameter	Section 2.2
α_{sc}	semiconvection efficiency parameter	Section 4.1
α_{th}	thermohaline efficiency parameter	Section 4.2
α_{∇}	smoothing parameter for MLT++	Section 7.2
$\bar{\alpha}_{\nabla}$	MLT++ parameter used in construction of α_{∇}	Section 7.2
β_{min}	$\min(P/P_{\text{gas}})$	Section 7.2
χ_ρ	$(\partial \ln P / \partial \ln \rho)_T$	Section 3.3
χ_T	$(\partial \ln P / \partial \ln T)_\rho$	Section 3.3
C_p	specific heat at constant pressure	Section 4.1
c_s	adiabatic sound speed	Section 3
$\Delta\nu$	large frequency separation of pulsation modes	Section 3.2
D_{ov}	overshoot diffusion coefficient	Section 3.3
D_{th}	thermohaline diffusion coefficient	Section 4.2
$E_{\text{F,c}}$	Fermi energy at center	Section 2.2
ϵ_{grav}	gravitational heating rate	Section 5.2
ϵ_{nuc}	nuclear heating rate	Section A.4
F_{conv}	convective flux	Section 7.1
f_{ov}	convective overshoot parameter	Section 3.2
F_{rad}	radiative flux	Section 7.1
f_{∇}	reduction factor for δ_{∇}	Section 7.2
Γ_1	$(\partial \ln P / \partial \ln \rho)_S$	Section 3
κ_{th}	opacity for thermal radiation orig. in planet	Section 2.4
κ_{ν}	opacity for irradiation from star	Section 2.4
k_{B}	Boltzmann constant	Section 2.2
L_{acc}	accretion luminosity	Section 5.3
λ_{max}	$\max(L_{\text{rad}}/L_{\text{Edd}})$	Section 7.2
L_{c}	core luminosity	Section 2.3
L_{Edd}	Eddington Luminosity	Section 6.3
$\log g$	log surface gravity	Section A.5
L_{onset}	lum. at onset of convection	Section 7.1

Table 1 — *Continued*

Name	Description	First Appears
L_{rad}	radiative luminosity	Section 7.1
L_{inv}	lum. at which density inversion occurs	Section 7.1
m_{u}	atomic mass unit	Section A.1
M_{c}	core mass	Section 2.3
\dot{M}	mass-loss rate	Section 5.3
M_{m}	modeled mass	Section B.4
N_{A}	Avogadro number	Section 2.2
∇_{ad}	adiabatic temperature gradient	Section 3.3
∇_{L}	Ledoux criterion	Section 4.1
∇_{rad}	radiative temperature gradient	Section 3.3
∇_T	actual temperature gradient	Section 3.3
n_{B}	baryon density	Section A.1
ν_{max}	frequency of maximum power	Section 3.2
Ω	surface angular velocity	Section 6.3
ω	angular velocity	Section 6.1
Ω_{crit}	surface critical angular velocity	Section 6.3
P_{c}	central pressure	Section 2.1
P_{gas}	gas pressure	Section 5.3
P_{rad}	radiation pressure	Section 5.3
R_{c}	core radius	Section 2.3
ρ_{c}	central density	Section 2.1
λ_P	pressure scale height	Section 3.3
σ_{SB}	Stefan-Boltzmann constant	Section 2.1
S_{ℓ}	Lamb frequency	Section 3
δ_{∇}	superadiabaticity, $\nabla_T - \nabla_{\text{ad}}$	Section 7.2
$\delta_{\nabla, \text{thresh}}$	controls when MLT++ is applied	Section 7.2
T_{c}	central temperature	Section 2.1
T_{eff}	effective temperature	Section 2.1
δt	numerical timestep	Section 5.3
τ_{KH}	thermal (Kelvin-Helmholtz) timescale	Section 6.3
v_{eq}	equatorial velocity	Section 6

2. GIANT PLANETS AND LOW-MASS STARS

Evolutionary models of giant planets and low-mass stars differ from their higher-mass stellar counterparts in both the microphysics needed to describe the interior and the role of stellar irradiation in the outer boundary condition. For masses $M \lesssim 84 M_{\text{J}}$, hydrogen burning is insufficient to prevent cooling and contraction. Deuterium burning can briefly slow the cooling for $M \gtrsim 13 M_{\text{J}}$, where $M_{\text{J}} = 9.54 \times 10^{-4} M_{\odot}$ is Jupiter’s mass, but has a negligible influence on the cooling for smaller masses. Hence nuclear burning can be ignored in the planetary mass regime.

For hydrogen-helium rich objects with $M \gg M_{\text{J}}$, an ideal gas equation of state (EOS), with arbitrary degeneracy, is a good approximation while for $M \lesssim M_{\text{J}}$ particle interactions play an important role. Specifically, pressure ionization of hydrogen at $\rho \simeq 1 \text{ g cm}^{-3}$ and $T \simeq 10^4 \text{ K}$ causes a sudden change from a H_2 -dominated phase to an ionized phase. MESA employs the Saumon et al. (1995) equation of state (SCVH EOS), smoothly interpolated from the low to high pressure phase, for this complicated region of parameter space where thermal, Fermi, and electrostatic energies may all be comparable. At the low temperatures in planetary atmospheres, abundant species such as CNO atoms will be in molecular form, and may condense into clouds. MESA does not follow the transition from atomic to molecular form for these species in the EOS—they are currently included by increasing the helium abundance from Y to $Y + Z$ when calling the SCVH EOS. MESA does, however, include the effect of molecules in the Rosseland opacities. Currently, the Ferguson et al. (2005) and Freedman et al. (2008) tables, which include the opacity from molecules, but ignore condensates, are available.

Lastly, for planets in close-in orbits about their parent star, the external irradiation flux may be orders of magnitude larger

than the cooling flux from the planet’s interior. This may dramatically increase the surface temperature and affect the outer boundary condition. MESA now implements several options for this surface heating, including the flexibility to include user-supplied prescriptions.

In the following subsections, we discuss a new MESA module that creates initial models in the planetary mass range $M \approx 0.1\text{--}10 M_J$, and present a suite of evolutionary calculations. We discuss how surface irradiation may be included, as well as an inert core at the center of the planet. We also show what MESA star yields for the mass-radius relation for sub-solar mass stars in §2.5.

2.1. Construction of Starting Models

For stellar mass objects, the `pre_ms_model` routine constructs pre-main-sequence (PMS) models assuming $L(r) \propto m$, where $L(r)$ is the luminosity at radius r , by iterating on the starting conditions at the center to find a model with a given M and central temperature T_c . This PMS routine works well for $M \gtrsim 0.03 M_\odot$, but lower masses may not converge when the guess for central density ρ_c and luminosity are not close enough to the (unknown) true values. As a result, it is difficult and time consuming to create models with $M < 0.03 M_\odot$ using the same routine for giant planets as for stars.

A new routine called `create_initial_model` builds a model of given M and radius R using an adiabatic temperature profile. Given the central pressure P_c and specific entropy S , the equation of hydrostatic balance is integrated outward, and the temperature at each step determined from the equation of state using $T = T(P, S)$. The values of P_c and S are iterated to attain the desired M and R . The luminosity profile is then derived treating S as constant in space for the fully convective planet (e.g., Ushomirsky et al. 1998), so

$$\int_0^m dm' T(m') \frac{dS}{dt} \approx \frac{dS}{dt} \int_0^m dm' T(m') = -L(m). \quad (1)$$

The luminosity at the surface, $L(M)$, is estimated using the radius R and temperature T_{eff} at the $\tau = \kappa P/g = 2/3$ point as $L(M) = 4\pi R^2 \sigma_{\text{SB}} T_{\text{eff}}^4$. Given $L(M)$, the luminosity at interior points is found by

$$L(m) = L(M) \left(\frac{\int_0^m dm' T(m')}{\int_0^M dm' T(m')} \right). \quad (2)$$

This procedure works well for M down to $\sim 0.1 M_J$ and over a range of initial radii.

2.2. Evolutionary Calculations

Figures 1 and 2 show evolutionary calculations for models with masses $M = 0.2\text{--}20 M_J$. All models were evolved for 20 Gyr. The initial models from `create_initial_model` had a large radius $R = 5 R_J$, where $R_J = 7.192 \times 10^9$ cm is the equatorial radius of Jupiter. The other parameters used are $Y = 0.27$, $Z = 0.02$ and $\alpha_{\text{MLT}} = 2$. The opacity and EOS tables used are `eos_file_prefix = mesa`, `kappa_file_prefix = gs98` and `kappa_lowT_prefix = lowT_Freedman11`. The atmosphere model is `which_atm_option = simple_photosphere`.

Figure 1 is a low mass extension of Figure 16 from Paper I, showing evolution in the $\rho_c\text{--}T_c$ plane. Each track (solid black curve) is labeled on the left by the planet’s mass, and evolution goes from left to right. Initially the planet is non-degenerate and contraction increases both $\rho_c \propto R^{-3}$ and

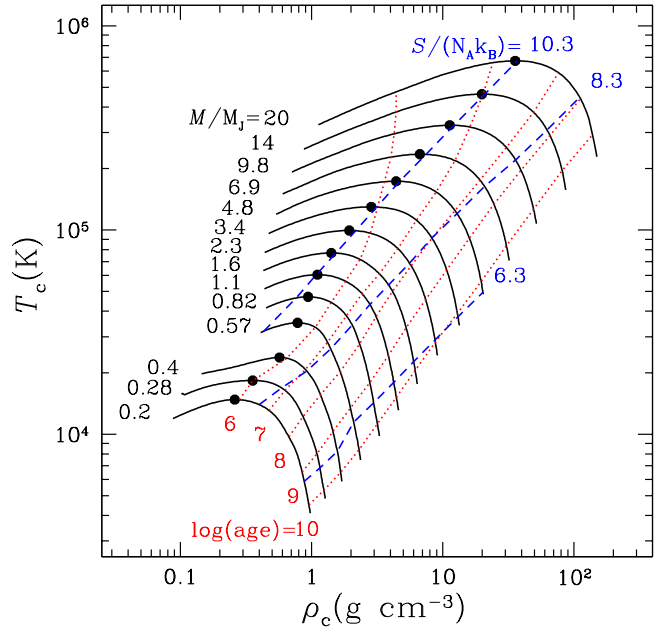


Figure 1. The solid black lines show T_c versus ρ_c during the evolution. Each line is labeled on the left by the mass in units of M_J . The dotted red lines show constant values of $\log(\text{age}[\text{yr}])$, labeled at the base of each line. The blue dashed lines show fixed values of $S/(N_A k_B)$, labeled at the top of each line. The large black dots show the position of maximum T_c along the evolutionary track.

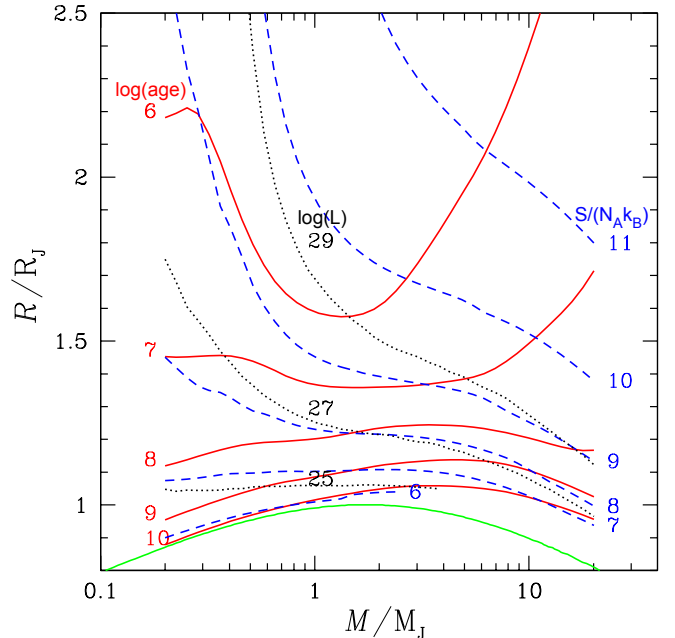


Figure 2. Radius versus mass iso-contours from a suite of evolutionary calculations. The solid red lines show R/R_J versus M/M_J at fixed values of $\log(\text{age}[\text{yr}])$, labeled on the left of each curve. The dashed blue curves are for fixed entropy, with each curve labeled by $S/(N_A k_B)$ on the right. The dotted black curves are for fixed luminosity, with each curve labeled by $\log(L[\text{erg s}^{-1}])$ above $M = 1 M_J$. The green curve at the bottom is the $T = 0$ $M\text{--}R$ relation from Zapolsky & Salpeter (1969) for a solar mixture of H and He.

$T_c \propto R^{-1} \propto \rho_c^{1/3}$. A maximum T_c is reached when $k_B T_c \sim E_{F,c}$, where $E_{F,c}$ is the electron Fermi energy at the center, beyond which ρ_c approaches a constant as T_c decreases further. Ignoring Coulomb interactions in the EOS, S is a function of the electron degeneracy parameter $\mu_e/k_B T$, where μ_e is the electron chemical potential and all models should have maximum $k_B T_c \sim E_{F,c}$ at the same S . The line labeled $S/(N_A k_B) = 10.3$ indeed coincides with maximum T_c down to $M \simeq 1 M_J$, but at smaller masses where non-ideal effects are more important, maximum T_c occurs when $S/(N_A k_B) < 10.3$. Also shown in Figure 1 are lines of constant age, shown as dotted red lines, and labeled on the bottom of the plot.

The same evolutionary calculations are used in Figure 2 to show radius versus mass at fixed values of age, entropy or luminosity. At late times, or low entropy and luminosity, the radius approaches the zero-temperature value (green curve; Zapolsky & Salpeter 1969) for which thermal support is insignificant. The maximum radius occurs where gravitational and Coulomb energies, per ion, are comparable. The solid red lines, labeled by age on the left, show that contraction down to $R \simeq 1.5 R_J$ is rapid, taking less than 10 Myr for $M \lesssim 10 M_J$. This initial rapid cooling phase occurs because the initial luminosity is orders of magnitude higher than the luminosity around one Gyr. This can be seen in the black dotted contours of constant $\log(L)$, where L is larger by a factor of 100 for $R = 1.3 R_J$ and 10^4 for $R = 1.7 R_J$, as compared to $R = 1.1 R_J$. The blue dashed lines show contours of constant entropy, labeled on the right by $S/(N_A k_B)$.

2.3. Implementation of Inert Cores

In the core accretion model of planet formation (e.g., Pollack et al. 1996; Hubickyj et al. 2005), a rock/ice core is first assembled. Once this core grows to ~ 10 Earth masses, it can initiate rapid accretion of nebular gas, which could then dominate the mass of the planet. For studies of planetary radii, a central core composed of high mean molecular weight material can decrease the radius of the planet by a significant amount ($\simeq 0.1\text{--}0.2 R_J$). The MESA star inert core feature allows one to add a core of specified mass M_c and radius R_c , or more conveniently, density ρ_c . A luminosity L_c may also be specified, although the high mean molecular weight of the core, as compared to the overlying H/He envelope, implies that even large cores will tend to have small heat content (Fortney et al. 2006). This inert core is not presently evolved in any way, and changes in P_c during evolution are neglected as R changes.

2.4. Irradiation

Surface heating by stellar irradiation changes the boundary condition for the planet’s cooling and contraction. This modifies the planetary radius versus age for exoplanets at orbital separation $\lesssim 0.1$ AU. MESA provides several ways to implement surface heating with varying degrees of fidelity to the true solution. These presently include:

a) An energy generation rate $\epsilon = F_\star/4\Sigma_\star$ applied in the outer mass column $\Sigma \leq \Sigma_\star$. Here F_\star is the day-side flux from the star, and $\Sigma(r) = \int_r^R dr' \rho(r')$ is the mass column. In steady-state, this generates an outward flux $F_\star/4$, which is meant to simulate the angle-averaged flux over the planetary surface. The parameters F_\star and Σ_\star are specified through the user-specified variables `irradiation_flux` and

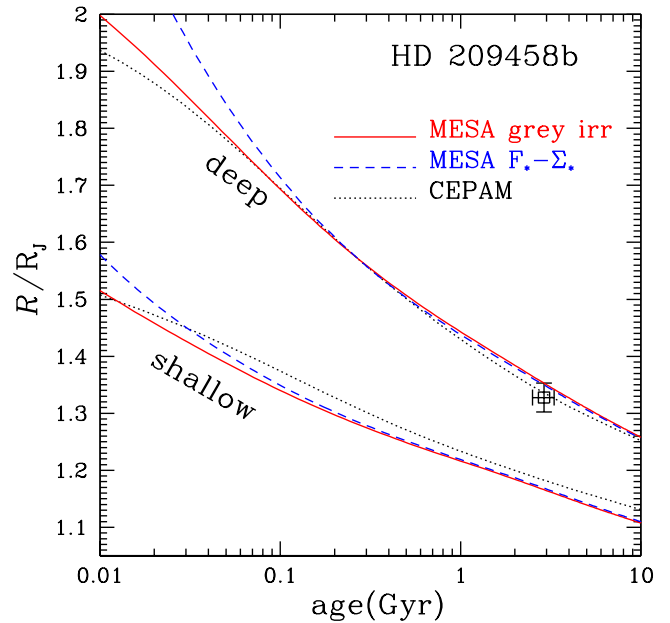


Figure 3. Radius versus age for the planet HD 209458b. The solid red lines are for MESA, using the `grey_irradiated` atmosphere model. The dotted black lines show the CEPAM code results. The dashed blue lines show the MESA calculation using the $F_\star\text{--}\Sigma_\star$ surface heat source. The data point with error bars is the observed value of the radius for HD 209458b quoted in Guillot (2010). The two sets of curves are deep heating (upper three curves) and shallow heating (lower three curves).

`column_depth_for_irradiation`, making this the simplest method to use. This heating mechanism represents absorption of stellar optical radiation well below the photosphere of the planet’s thermal radiation and gives rise to greenhouse heating of the atmosphere where $\epsilon \neq 0$.

b) MESA’s `grey_irradiated` atmosphere model (see also §A.5) implements the angle-averaged temperature profile of Guillot (2010). This approximate solution to the transfer equation assumes two frequency bands: optical radiation from the star (with user-specified opacity κ_*) and thermal radiation originating in the planet (with user-specified opacity κ_{th}). The temperature profile is derived using the Eddington approximation, assuming an external flux from the star as well as a flux from the planetary interior. This is the only MESA atmosphere model that uses pressure instead of optical depth to determine the surface boundary condition. As this pressure may be relatively deep in the atmosphere, a correction to the radius may be required to give either the vertical thermal photosphere, or the optical photosphere in transit along a chord. Lastly, the `relax_irradiation` routine improves initial convergence by providing a starting model closer to the irradiated one.

c) Finally, MESA allows user-specified heating functions (e.g., $F_\star\text{--}\Sigma_\star$ surface heating) or atmosphere models (e.g., `grey_irradiated`). User-supplied routines may be easily implemented by using the `other_energy` module.

Figure 3 shows radius versus age for the planet HD 209458b (Guillot 2010). The two groupings of lines are for different heating depths, and within each grouping of lines, there are three calculations: MESA using `grey_irradiated`

surface boundary condition (solid red line), MESA using the $F_{\star}-\Sigma_{\star}$ surface heating profile (dashed blue line), and CEPAM (Guillot & Morel 1995) using the same grey irradiated boundary condition (dotted black line; kindly provided by Tristan Guillot). The lower curves, corresponding to shallow heating, use fiducial values $(\kappa_{\text{th}}, \kappa_{\text{v}}) = (10^{-2}, 6 \times 10^{-3}) \text{ cm}^2 \text{ g}^{-1}$ and give a model radius significantly smaller than the observed radius. The upper curves, corresponding to deep heating, use $(\kappa_{\text{th}}, \kappa_{\text{v}}) = (10^{-2}, 6 \times 10^{-4}) \text{ cm}^2 \text{ g}^{-1}$, yielding significantly hotter temperatures deep in the surface radiative zone, which slow the cooling enough to agree with the observed radius. The choice $\Sigma_{\star} = 2/\kappa_{\text{v}}$ gives agreement between the grey irradiated and $F_{\star}-\Sigma_{\star}$ methods, where the factor of 2 accounts for the fact that the grey irradiated boundary condition has some heating below $\Sigma = 1/\kappa_{\text{v}}$. The radii are at the $\tau_{\text{th}} = 2/3$ photosphere for a vertical path into the atmosphere.

The agreement between all three methods is excellent, at the 1–2% level after 100 Myr. The remaining discrepancy between the MESA and CEPAM grey irradiated results are likely due to different opacity tables, with the MESA result using an update of Freedman et al. (2008) (Freedman 2011, priv. comm.) while the CEPAM run uses the Allard et al. (2001) COND table. The differences at ages ≤ 100 Myr are due to different starting conditions. The CEPAM calculation started with initial radius $2R_{\text{J}}$, whereas the MESA calculations started with $5R_{\text{J}}$. The MESA grey irradiated and $F_{\star}-\Sigma_{\star}$ calculations differ at ≤ 100 Myr, likely because the former has a fixed thermal opacity while the latter allows the opacity to change.

2.5. Low-Mass Main Sequence Stars

Most of MESA star’s capability to evolve low-mass ($M < 2M_{\odot}$) stars was demonstrated in Section 7.1 of Paper I. MESA has seen use in the asteroseismology of helium core flashing stars (Bildsten et al. 2012) and the discovery of a new instability from the onset of ${}^3\text{He}$ burning (van Saders & Pinsonneault 2012). We expect the future use of MESA star for asteroseismic investigations of these stars to be substantial (see §3).

The derivation of accurate planetary radii based on transits requires accurate radii of the host stars; this motivates MESA star investigations of low-mass stars (Lloyd 2011). Figure 4 shows 1 and 5 Gyr isochrones at solar composition ($Y = 0.27, Z = 0.019$) from MESA star (solid lines) and Dotter et al. (2008, dashed lines) in the mass-radius diagram. Data points shown in Figure 4 are taken from Torres et al. (2010), Carter et al. (2011), Irwin et al. (2011), and Bass et al. (2012). This figure is a reproduction of the upper panel of Figure 11 from Bass et al. (2012). Figure 4 indicates that MESA star is capable of producing mass-radius relations for main sequence stars that are consistent with other widely-used models as well as observational data. The MESA star models were computed using, as much as possible, the same physical assumptions as the models used by Dotter et al. (2008). The main difference is the equation of state, for which Dotter et al. (2008) used FreeEOS¹⁰ and MESA star uses a combination of the OPAL (Rogers & Nayfonov 2002) and SCVH EOS for thermodynamic parameters relevant to this diagram.

3. ASTEROSEISMOLOGY

With its highly configurable output options, and its ability to calculate asteroseismic variables, MESA star can read-

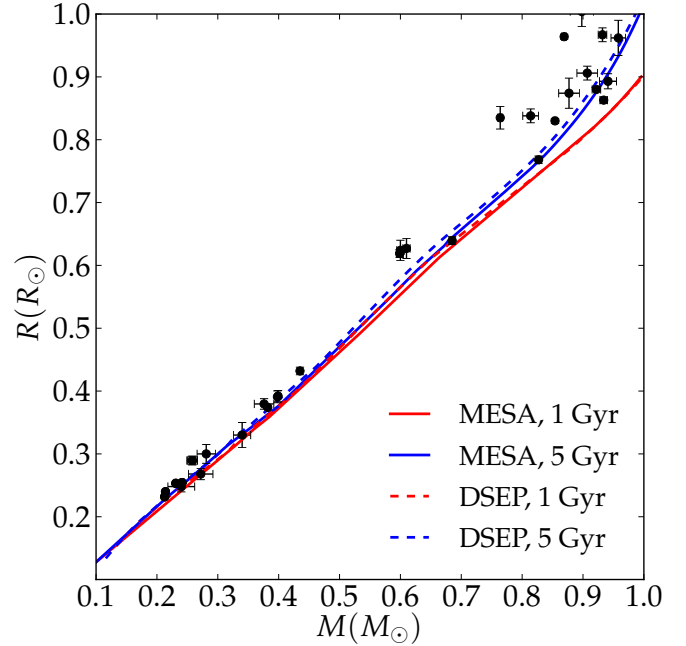


Figure 4. Stellar isochrones at solar composition spanning 0.1 to $1 M_{\odot}$ from MESA star (solid lines) and Dotter et al. (2008, dashed lines) in the mass-radius plane. The data points plotted are the same as shown by Bass et al. (2012).

ily produce models suitable for use with a range of oscillation codes. In addition to its own text output files, MESA can produce outputs in formats widely used by stellar oscillation codes, such as `fgong` and `osc` (Monteiro 2009).

In Figure 5 we show the evolution of a $1M_{\odot}$ model in the Hertzsprung-Russell Diagram (HRD) and in $T_c-\rho_c$ space. These were evolved following the test case found in `1M_pre_ms_to_wd`, which was modified to include diffusion. This runs without user intervention from pre-main sequence to white dwarf. To demonstrate the changing stellar structure as the model evolves from the main sequence to post helium-core burning on the Asymptotic Giant Branch (AGB), we show in Figure 6 some of the fundamental quantities extracted from the corresponding `profile.data` files for the models marked in Figure 5. These include the Lamb and Brunt-Väisälä frequencies defined respectively by

$$S_{\ell}^2 = \frac{\ell(\ell+1)c_s^2}{r^2}, \quad (3)$$

$$N^2 = \frac{g}{r} \left[\frac{1}{\Gamma_1} \frac{d \ln P}{d \ln r} - \frac{d \ln \rho}{d \ln r} \right], \quad (4)$$

where c_s is the adiabatic sound speed and ℓ is the spherical harmonic degree.

3.1. The Solar Sound Speed Profile

The seismic properties of the Sun provide a test of stellar evolution models, and an opportunity to calibrate α_{MLT} for any particular set of input physics and other assumptions. The MESA star test case `solar_calibration` produces a calibrated Standard Solar Model. Figure 7 shows the difference between the helioseismically-inferred solar sound speed profile and this model. We also show “Model S” from Christensen-Dalsgaard et al. (1996). Both models employ comparable input physics and assume solar abundances from Grevesse & Noels (1993) and Grevesse & Sauval (1998). One

¹⁰ <http://freeeos.sourceforge.net>

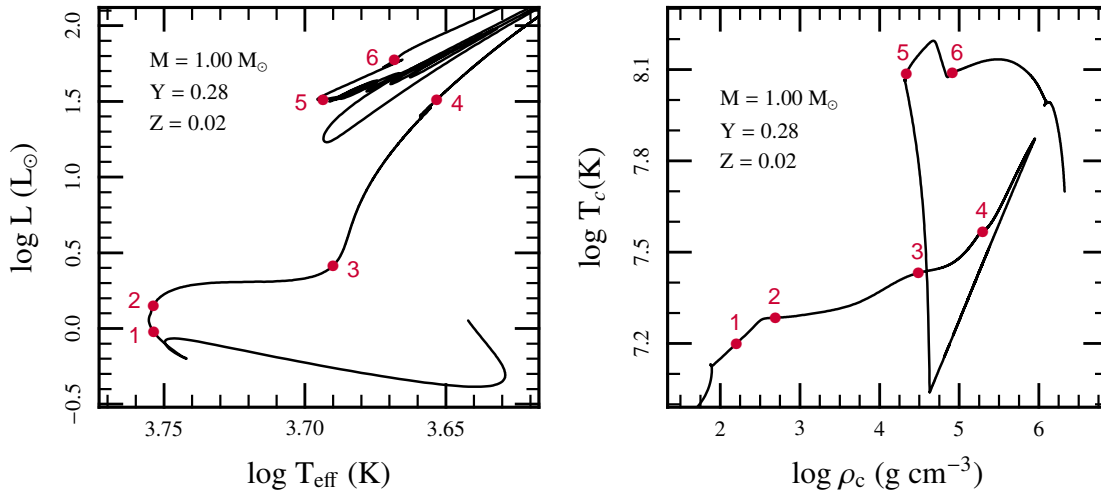


Figure 5. Hertzsprung-Russell diagram and T_c - ρ_c evolution of a $1 M_{\odot}$ model evolving from pre-main sequence to the white dwarf cooling sequence. The number labels denote selected models, for which we show internal profiles in Fig. 6.

clear improvement since Paper I is a smoother sound speed profile at small r/R , which is primarily due to improvements in the diffusion module. This is particularly important for asteroseismology, where sharp features in the sound speed profile can influence the stellar oscillation frequencies. The results are based on the solar calibration test case compiled with the GNU Fortran compiler version 4.7.2 on Mac OS X 10.7.5; Appendix B.9 provides information about how the solar calibration results may depend on different operating systems and compilers.

3.2. New Asteroseismic Capabilities in MESA

The “astero” extension to MESA star implements an integrated approach that passes results automatically between MESA star and the new MESA module based on the adiabatic code ADIPLS (Christensen-Dalsgaard 2008a, June 2011 release). The MESA module ADIPLS also supports independent use for post-processing.

This astero extension enables calculation of selected pulsation frequencies by MESA star during the evolution of the model. This allows fitting to the observations that can include spectroscopic constraints (e.g., $[\text{Fe}/\text{H}]$ and T_{eff}), asteroseismic constraints, such as the large frequency separation ($\Delta\nu$) and the frequency of maximum power (ν_{max}), and even individual frequencies. A variety of approaches for finding a best-fitting model are available, including grid searches and automatic χ^2 minimization by the Hooke-Jeeves algorithm (Hooke & Jeeves 1961) or by the “Bound Optimization BY Quadratic Approximation” (BOBYQA; Powell 2009) technique. These searches are user controlled through a number of parameter bounds and step sizes. Users also have full control over the relative weight assigned to the seismic and spectroscopic parts of the χ^2 statistic.

For the automated χ^2 minimization, astero will evolve a pre-main sequence model from a user defined starting point, and find the best match along that single evolutionary track. The code then recalculates the track, again initiated at the pre-main sequence, with different initial parameters such as mass, composition, mixing length parameter and overshoot, and repeats until the lowest χ^2 has been found.

Calculating specific mode frequencies is computationally intensive. Hence, a number of options exist to improve the efficiency of the minimization when individual frequencies

are included. Bounds can be established on stellar parameters (e.g., T_{eff} , central H mass fraction, $\Delta\nu$), so that ADIPLS is invoked only when the model falls within these bounds. This enables certain evolutionary stages to be skipped when other observational diagnostics rule them out—if a star is known to be a red giant, for instance, there is no sense in invoking ADIPLS when models are on the main sequence. The large frequency separation, $\Delta\nu$, of the model is calculated as the inverse of the sound travel time through the star, $\Delta\nu = [2 \int dr/c_s]^{-1}$ (Tassoul 1980; Gough 1986). There is also the option to derive $\Delta\nu$ using simple solar scaling: $\Delta\nu \propto (M/R^3)^{0.5}$ (Kjeldsen & Bedding 1995).

Moreover, hierarchical approaches to the frequency fitting can be selected, saving large amounts of computational time. In one case the radial modes are first calculated, and only when they match reasonably well are the non-radial mode frequencies derived and included in the χ^2 . This is particularly beneficial for red giants where the calculation of the non-radial frequencies is extremely time consuming. Another example is when the time steps in the stellar evolution calculations are too large to find an accurate minimum of χ^2 . Hence, as a further option to increase efficiency while attaining accuracy, the time steps can be set to automatically reduce when the model comes close to the “target box” of the observational constraints. As for other modules used in MESA star, astero offers a range of graphical outputs including an échelle diagram where the fitting process can be followed in real time.

There is also an option for including corrections to the model frequencies on-the-fly to compensate for the inadequate modelling of the near surface layers of the star. The effect, known as the “surface term,” is seen as a frequency dependent offset between the modelled and observed acoustic frequencies of the Sun (e.g. Christensen-Dalsgaard & Thompson 1997). The offset increases towards higher frequencies and is well described by a power law (Kjeldsen et al. 2008). MESA star follows the approach described by Kjeldsen et al. (2008) for correcting the surface term.

To illustrate the performance of astero, we show here a fit to the star HD43985. The input frequencies and the spectroscopic constraints are from Deheuvels et al. (2010). We first ran a wide-range grid search over M , α_{MLT} , $[\text{Fe}/\text{H}]$, and Y , including only $[\text{Fe}/\text{H}]$, T_{eff} , and $\Delta\nu$ as observational constraints. The results of this initial search guided our starting param-

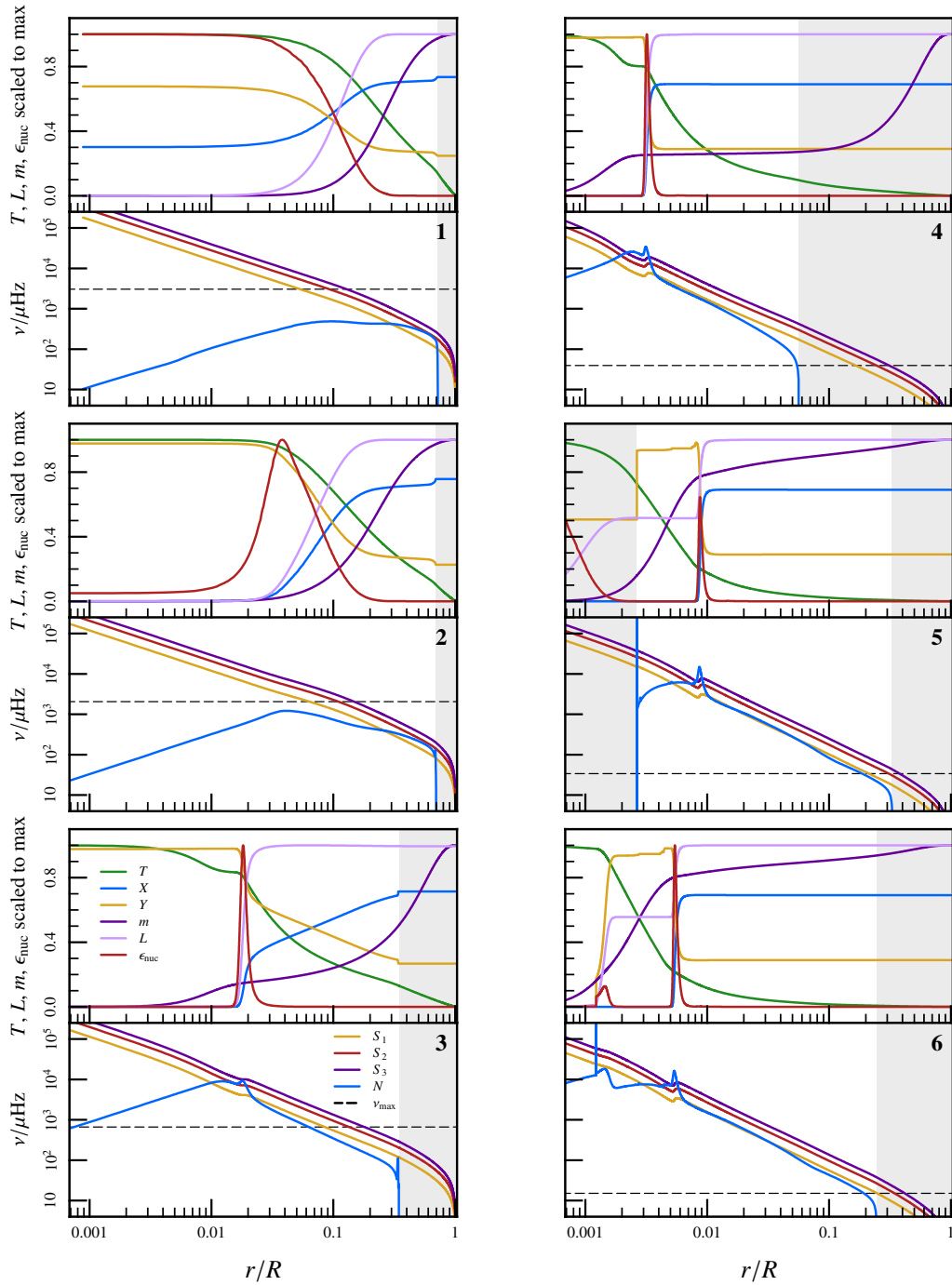


Figure 6. Internal structure of the six points (indicated by the numbers in each panel) marked in Figure 5. The top panel for each points shows luminosity, temperature, mass, nuclear energy generation rate, and hydrogen and helium mass fractions. Grey areas mark convective regions according to the Schwarzschild criterion. Bottom panels show N and S_ℓ for harmonic degrees $\ell = 1, 2,$ and 3 . The dashed line indicates the frequency of maximum power, ν_{\max} of the stochastically excited solar-like modes.

ters and ranges for the next automatic χ^2 minimization. We first compare our grid results with those of the RADIUS grid search routine (Stello et al. 2009), which is based on a grid of ASTEC models (Christensen-Dalsgaard 2008b) and find agreement within uncertainties.

We then include the individual oscillation frequencies and use the Hooke-Jeeves algorithm for the χ^2 minimization. Model frequencies were corrected for the surface term, and the part of the χ^2 coming from the frequencies was given 2/3 of the weight in the final χ^2 , similar to that used by Metcalfe

et al. (2012). To ensure we adequately sample the parameter space, we initiate the search at several initial values within a broad range.

Each ‘‘Hooke’’ search generates several stellar evolution tracks, each with a best χ^2 value. We then combine the data from about 1400 tracks to estimate the $1\text{-}\sigma$ uncertainties in the varied parameters following the approach by Deheuvels et al. (2010). The lowest (reduced) χ^2 value we obtained was 2.4 with a few tens of models in the 2.4–4.0 range, which all fit the frequencies similarly well. Among these models there are

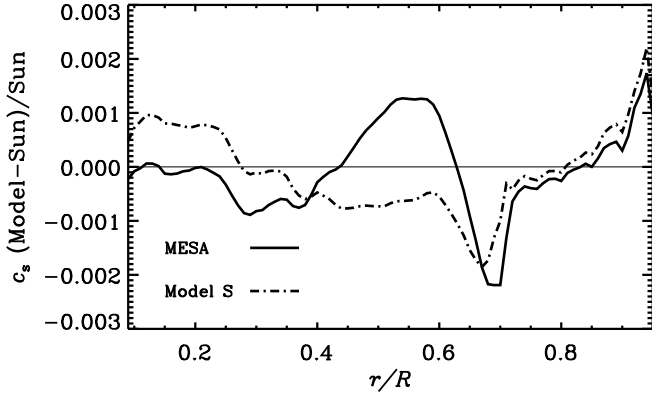


Figure 7. Comparison of the difference between the helioseismically-inferred sound speed profile (Bahcall et al. 1998) to that of a MESA star model and Model S (Christensen-Dalsgaard et al. 1996).

two families of results, one of which has slightly lower $[\text{Fe}/\text{H}]$ and Y , and a slightly increased value for the spectroscopic part of the χ^2 .

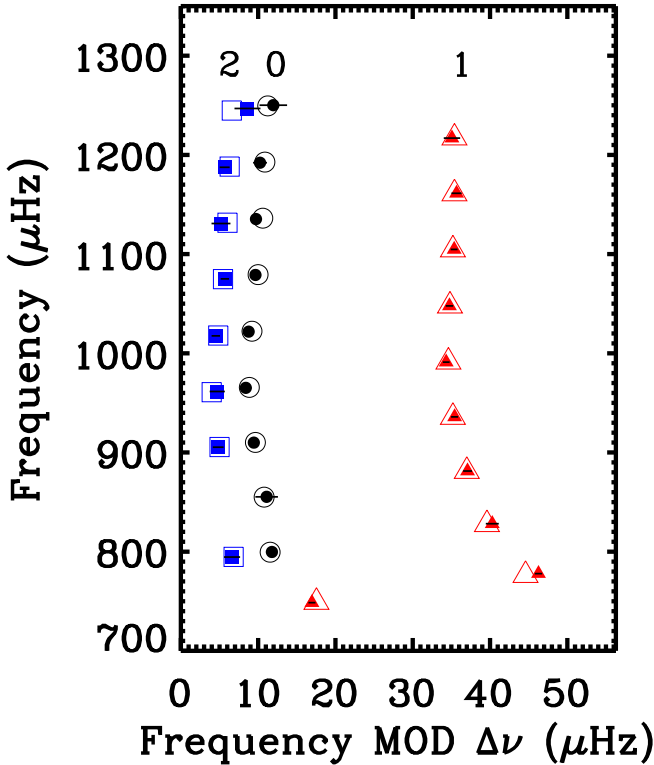


Figure 8. Échelle diagram of the oscillation frequencies of the subgiant HD49385. Observed frequencies are shown with filled symbols as blue squares ($\ell = 2$), black circles ($\ell = 0$), and red triangles ($\ell = 1$), and the matched model frequencies are shown with open symbols. Black horizontal lines indicate 1- σ error bars.

The comparison of the observed and modeled frequencies for the realization with the lowest χ^2 is shown in the échelle diagram format in Figure 8. A plot of the internal structure including the Brunt-Väisälä and Lamb frequencies is shown in Figure 9, and the parameters of the model are listed in Table 2. We set $f_{\text{ov}} = 0.015$ and use the GN98 solar abundances. Our results can be best compared to those listed as “low α_{ov} ” and “GN93” in Table 4 of Deheuvels & Michel (2011) and agree within the uncertainties.

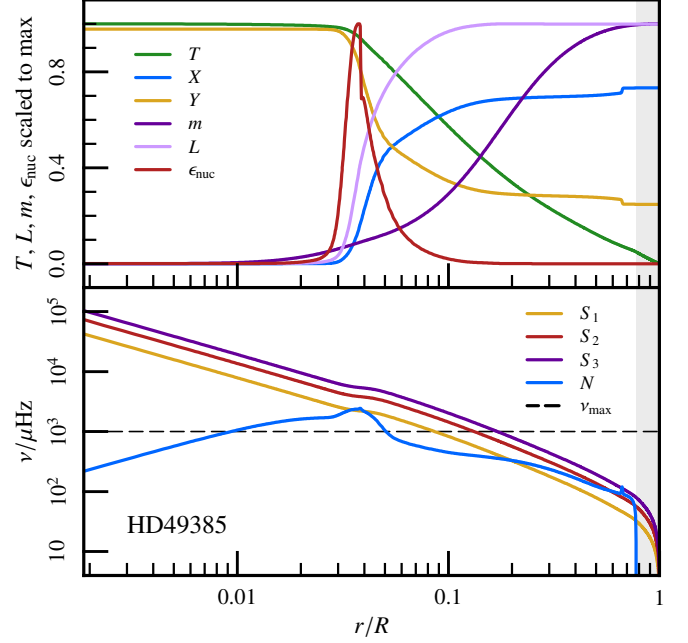


Figure 9. Same format as in Figure 6, but for the best-fitting model of HD49385 (see also Table 2).

Table 2
Properties of best fitting model to HD49385

Quantity	Value
M/M_{\odot}	1.30 ± 0.04
R/R_{\odot}	1.972 ± 0.016
L/L_{\odot}	4.9 ± 0.4
$\log g$	3.962 ± 0.003
T_{eff}/K	6115 ± 125
Age/Gyr	4.1 ± 0.4
α_{MLT}	1.9 ± 0.1
$[\text{Fe}/\text{H}]_i$	0.15 ± 0.04
$[\text{Fe}/\text{H}]_s^a$	0.063
Y_{initial}	0.29 ± 0.02
Z_{initial}	0.0222
χ^2	2.40

^a $[\text{Fe}/\text{H}]_s$ is the log of the ratio of the surface (Z/X) relative to the solar value of 0.02293.

3.3. The Effect of Composition Gradients on the Brunt-Väisälä Frequency

For g-modes, the most important quantity is the Brunt-Väisälä or buoyancy frequency N . It is crucial for pulsation studies that a smooth and accurate method is available for calculating N^2 . In a highly degenerate environment, the pressure is nearly independent of temperature and $P \propto \rho^{\Gamma_1}$, so from eq. (4) we see that N^2 depends on the difference of two large and nearly equal quantities. This can lead to a loss of precision and a noisy N^2 . To eliminate this problem, N^2 is rewritten into a form that depends on the difference of the adiabatic and true temperature gradients and on the composition gradient:

$$N^2 = \frac{g^2 \rho \chi_T}{P \chi_{\rho}} (\nabla_{\text{ad}} - \nabla_T + B). \quad (5)$$

The term B explicitly takes into account the effect of composition gradients and is commonly called the Ledoux term

(e.g., Unno et al. 1989; Brassard et al. 1991). For the general case of an N -component plasma with mass fractions $\{X_i\}$, the standard formula for B is (e.g., Unno et al. 1989)

$$B = -\frac{1}{\chi_T} \sum_{i=1}^{N-1} \left(\frac{\partial \ln P}{\partial \ln X_i} \right)_{\rho, T, \{X_{j \neq i}\}} \frac{d \ln X_i}{d \ln P}. \quad (6)$$

Since $\sum_{i=1}^N X_i = 1$, one of the mass fractions can be eliminated, so that the sum in eq. (6) runs from 1 to $N-1$. We note that the partial derivatives in eq. (6) hold all the $\{X_j\}$ constant except for X_i and X_N , where X_N is varied so as to maintain $\sum_{i=1}^N X_i = 1$.

Although eq. (6) is formally correct, we have developed a new prescription that is both numerically robust and simple to implement. We define a new Ledoux term by taking a variation along the radial composition gradient in the model space,

$$B \equiv -\frac{1}{\chi_T} \lim_{\delta \ln P \rightarrow 0} \frac{\ln P(\rho, T, \vec{X} + (d\vec{X}/d \ln P) \delta \ln P) - \ln P(\rho, T, \vec{X})}{\delta \ln P}. \quad (7)$$

In a stellar model, the implementation of the derivatives involve differencing quantities on neighboring mesh points. Thus, using the subscript k to denote the value of a given quantity on the k th mesh point, we have

$$B = -\frac{1}{\chi_T} \frac{\ln P(\rho_k, T_k, \vec{X}_{k+1}) - \ln P(\rho_k, T_k, \vec{X}_k)}{\ln P_{k+1} - \ln P_k}. \quad (8)$$

This is the form of the Ledoux term that is implemented in MESA and we term it the ‘‘New Ledoux’’ formulation. Since MESA ensures that $\sum_{i=1}^N X_i = 1$ at each mesh point, this condition does not have to be separately enforced. This formulation requires just one numerical difference along \vec{X} that is consistent with the stellar model and equation of state and does not require derivatives with respect to individual mass fractions.

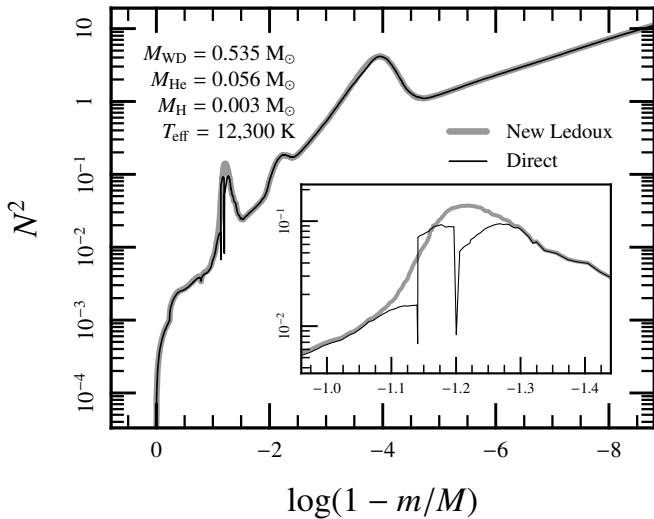


Figure 10. A comparison of the new Ledoux prescription for N^2 versus the direct numerical calculation. This calculation is for a $0.535 M_{\odot}$ white dwarf model at $T_{\text{eff}} = 12,300$ K.

In Figure 10 we compare N^2 obtained with the New Ledoux prescription (grey heavy curve) to that found from the direct numerical evaluation of eq. (4) using finite differences (thin black curve). For the $0.535 M_{\odot}$ white dwarf model presented

here it is evident that the new Ledoux criterion gives noticeably smoother results. In particular, the inset box highlights a region in which the direct calculation exhibits many noise that the new formulation does not.

4. MIXING MECHANISMS INVOLVING COMPOSITION GRADIENTS

We described the implementation of mixing-length theory (MLT) in Paper I, including the allowance for overshoot beyond the boundaries of the convective zones as determined by the standard Schwarzschild condition, $\nabla_{\text{rad}} > \nabla_{\text{ad}}$. Overshooting is implemented via an exponential decay of the convective diffusion coefficient beyond the boundary of full convection, following Herwig (2000):

$$D_{\text{ov}} = D_{\text{conv},0} \exp\left(-\frac{2\Delta r}{f_{\text{ov}} \lambda_P}\right), \quad (9)$$

where $D_{\text{conv},0}$ is the diffusion coefficient at the convective border, Δr is the distance from the start of overshoot, and λ_P is the local pressure scale height. The user-adjusted parameter f_{ov} then determines the extent of the overshooting region. MESA also allows for the adoption of a step-function overshooting model, where the mixing region extends a distance $f_{\text{ov}} \lambda_P$ beyond the convective boundary with a constant specified diffusion coefficient.

In Paper I we did not implement the influence of composition gradients on mixing and the resulting diffusion coefficients when instabilities are operative. The description of how MESA star calculates the Ledoux criterion is in §3.3. In this section, we describe the implementation of mixing due to composition gradients in stellar interiors.

4.1. Semiconvection

Semiconvection refers to mixing in regions unstable to Schwarzschild but stable to Ledoux, that is

$$\nabla_{\text{ad}} < \nabla_T < \nabla_L, \quad (10)$$

where ∇_L is the sum of the adiabatic gradient and the Brunt composition gradient term (see eq. [6]),

$$\nabla_L \equiv \nabla_{\text{ad}} + B. \quad (11)$$

Once ∇_L is calculated, regions satisfying equation (10) undergo mixing via a time-dependent diffusive process with a diffusion coefficient calculated by the `mlt` module following Langer et al. (1983),

$$D_{\text{sc}} = \alpha_{\text{sc}} \left(\frac{K}{6C_P \rho} \right) \frac{\nabla_T - \nabla_{\text{ad}}}{\nabla_L - \nabla_T}, \quad (12)$$

where $K = 4acT^3/(3\kappa\rho)$ is the radiative conductivity, C_P is the specific heat at constant pressure, and α_{sc} an efficiency parameter.

We stress that semiconvection and overshooting have distinct implementations in MESA. Both are time-dependent diffusive processes. As an example, in Figure 11 we display profiles of thermodynamic gradients and their resulting diffusion coefficients during core helium burning in a semiconvective model with $\alpha_{\text{sc}} = 0.02$ and in an exponentially overshooting model with $f_{\text{ov}} = 10^{-5}$.

4.2. Thermohaline Mixing

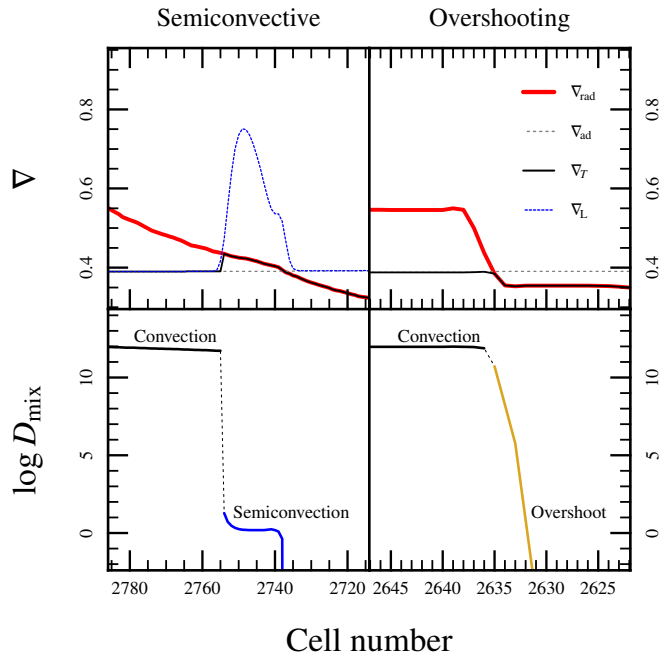


Figure 11. Sample profiles of semiconvective (left) and exponentially overshooting (right) $3M_{\odot}$ models undergoing core helium burning. Top panels show the radiative, adiabatic, temperature, and Ledoux gradients that determine mixing boundaries and diffusion coefficients. Bottom panels show the resulting diffusion coefficients for energy and chemical transport. In either case, a thin dotted line spanning a single intermediate cell joins the convective and semiconvective/overshoot curves. This is intended merely as a guide for the eye, as diffusion coefficients are defined only at the two boundaries of a cell. In particular, diffusion for this intermediate cell is governed by convection at its interior boundary and semiconvection/overshoot at the exterior. The semiconvective model shown here was run with $\alpha_{sc} = 0.01$; the exponentially overshooting model with $f_{ov} = 10^{-5}$. The profiles are taken at the points marked in Figure 15.

Thermohaline mixing arises in the presence of an inversion of the mean molecular weight in regions that are formally stable against convection according to the Ledoux criterion,

$$\nabla_T - \nabla_{ad} \leq B \leq 0, \quad (13)$$

In MESA thermohaline mixing is treated in a diffusion approximation, with a diffusion coefficient motivated by the linear stability analysis of Ulrich (1972) and Kippenhahn et al. (1980)

$$D_{th} = \alpha_{th} \frac{3K}{2\rho C_P} \frac{B}{(\nabla_T - \nabla_{ad})}. \quad (14)$$

The quantity α_{th} is an efficiency parameter. In the linear analysis it depends on the aspect ratio of the blobs/fingers arising from the instability. In the case of salt fingers such a value is calibrated using laboratory experiments in water (e.g. Krishnamurti 2003), where the fingers have an aspect ratio of ≈ 5 . In the stellar case the value of this parameter is vexatious (e.g. Charbonnel & Zahn 2007; Denissenkov & Pinsonneault 2008; Cantiello & Langer 2010; Wachlin et al. 2011), with recent 2D and 3D hydrodynamical calculations pointing toward a much reduced value of α_{th} relative to the salt fingers case (Denissenkov 2010; Traxler et al. 2011). Figure 12 shows a calculation including the effects of thermohaline mixing during the RGB phase of a $1M_{\odot}$ star after the luminosity bump (e.g. Charbonnel & Zahn 2007; Cantiello & Langer 2010).

4.3. Impact of Mixing on Convective Core Hydrogen and Helium Burning

The duration of the hydrogen and helium core burning depends on the extent of the convective core, so we focus here on exhibiting the MESA capabilities during these phases. As we noted above, there are many physical effects that change the size of the convective core, such as semiconvection, overshooting, and rotation-induced mixing. For example, the Schwarzschild criterion implies larger cores than the Ledoux criterion, but when using Ledoux alone, the region above the convective boundary is overstable and so semiconvection occurs (see §4.1).

We evolved a non-rotating $1.5M_{\odot}$ star with $(Y, Z) = (0.23, 0.02)$ through central hydrogen burning using Ledoux, Ledoux plus semiconvection, Schwarzschild, and Schwarzschild plus overshoot. As is evident in Figure 13, this set of physical processes leads to a large range of convective core masses and thereby main sequence lifetimes. For the parameters explored we found that overshooting increases the lifetime by a factor $\lesssim 1.2$ for Schwarzschild and $\lesssim 2.5$ for Ledoux. Figure 14 shows an HR diagram for each of the $1.5M_{\odot}$ models undergoing core hydrogen burning, showing the impact of convective core extent on main-sequence turnoff morphology.

We also evolved a non-rotating $3M_{\odot}$ star with $(Y, Z) = (0.25, 0.02)$ through central helium burning. Overshooting extends the burning lifetime by a factor $\lesssim 1.6$ for Schwarzschild and $\lesssim 2.8$ for Ledoux. Although this lengthening of the core burning phase is always true of convective overshoot, we find that the extension of the overshoot and convective regions is sensitive to the temporal resolution adopted. With sufficiently large values of f_{ov} the upper boundary develops oscillatory behavior which can also affect the lifetime. This behavior also occurs when the overshoot is implemented with the step-function implementation of overshoot. This instability is not seen in overshoot during hydrogen burning and has yet to be studied in detail.

5. EVOLUTION BEYOND THE MAIN SEQUENCE AND WHITE DWARFS

Extending the verification of Paper I, we now compare to other available codes for intermediate-mass stars, $3\text{--}8M_{\odot}$. We describe the techniques used by MESA star to evolve stars through the AGB phase to the white dwarf cooling sequence. We also demonstrate how MESA star incorporates compressional heating from accretion.

5.1. Code Comparisons during Helium Core Burning

We start by comparing the results of MESA star to those from the Dartmouth Stellar Evolution Program (DSEP; Dotter et al. 2008) for stars with $M = 3\text{--}8M_{\odot}$. In both cases, the models were evolved from the pre-main sequence to the depletion of helium in their cores. For completeness, the MESA star models were further evolved to the occurrence of the first helium thermal pulse.

All models have an initial composition $Y = 0.272$, $Z = 0.02$, and no mass loss or rotation was included. The boundaries of mixing zones are determined by the Schwarzschild criterion with $\alpha_{MLT} = 2$. In order to compare the codes, we do not allow overshooting or semiconvection. We adopt the Kunz et al. (2002) rate for $^{12}\text{C}(\alpha, \gamma)^{16}\text{O}$ and the Imbriani et al. (2004) rate for $^{14}\text{N}(p, \gamma)^{15}\text{O}$; for all other rates we use the NACRE compilation (Angulo et al. 1999). We use the OPAL Type 2 opacity tables (Iglesias & Rogers 1993) to account for the carbon- and oxygen-enhanced opacities during helium burning.

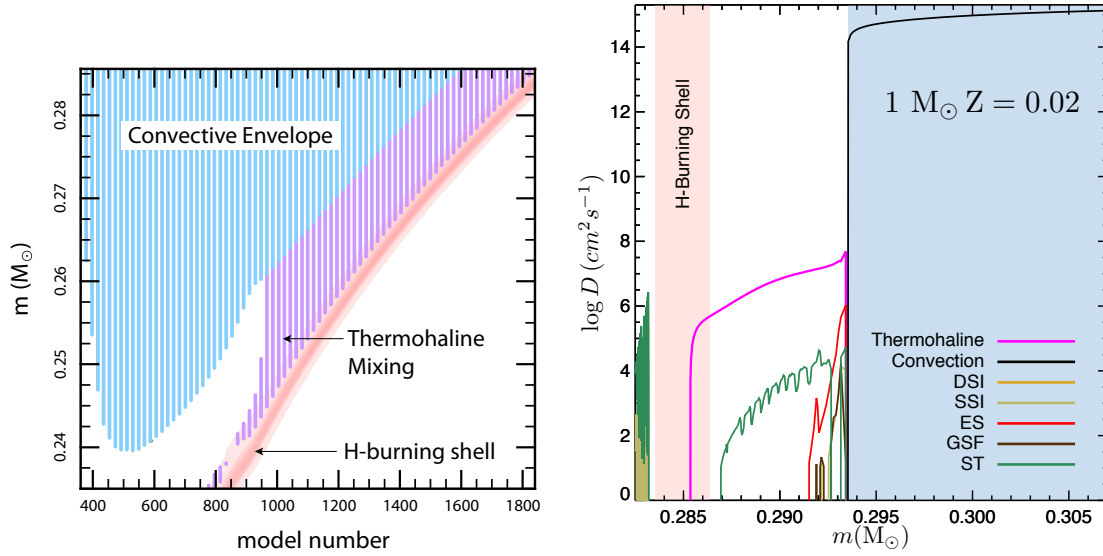


Figure 12. Thermohaline mixing during the RGB phase of a $Z = 0.02$, $1 M_{\odot}$ model, initially rotating with an equatorial velocity of 10 km s^{-1} . In the left panel a Kippenhahn diagram shows, in mass coordinate and as function of model number, the locations of the retreating convective envelope (blue), of the H-burning shell (red) and of the thermohaline mixing region (magenta). The right panel shows diffusion coefficient profiles extracted at model number 1849, which is the last model shown in the Kippenhahn plot. The H-burning shell and the convective envelope are shaded in red and blue, respectively. Thermohaline mixing (magenta line) transports chemicals between the burning shell and the convective envelope. Also shown are the diffusion coefficients resulting from Eddington-Sweet circulation (ES), magnetic torques by dynamo generated fields (ST), Dynamical Shear (DSI), Secular Shear (SSI) and Goldreich-Schubert-Fricke (GSF) instability (see §6 for details).

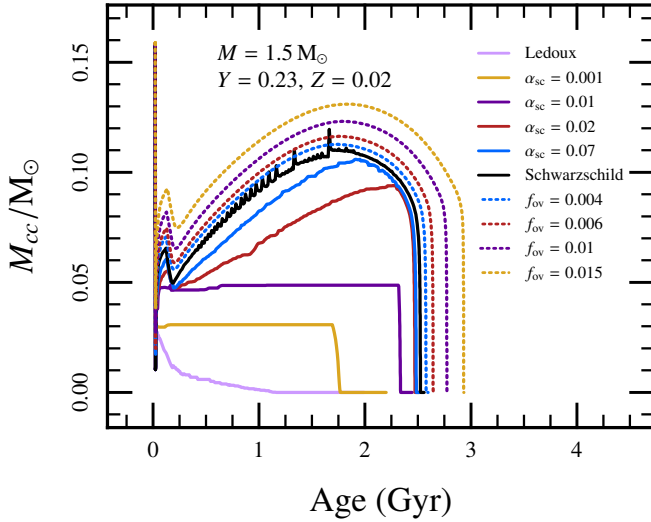


Figure 13. History of convective core extent during the main sequence for a non-rotating $1.5 M_{\odot}$ star with various mixing options. The plot shows the boundary of convection not including the extent of semiconvection or overshooting.

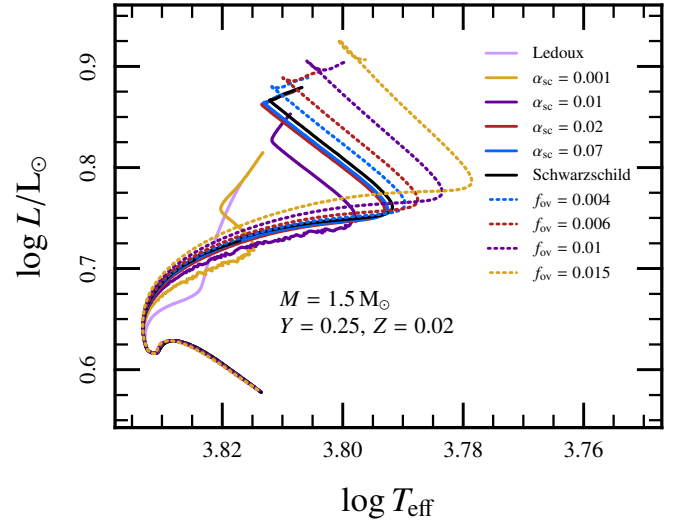


Figure 14. The HR diagram for the non-rotating $1 M_{\odot}$ star with various mixing options. Tracks are displayed from ZAMS until depletion of core hydrogen to $X = 10^{-5}$.

The resulting tracks in the HR diagram of Figure 16 and the evolution in the T_c - ρ_c plane of Figure 17 show excellent agreement between the codes. Figures 18 and 19 show the hydrogen-burning luminosity, the helium-burning luminosity, and the extent of the convective core during convective helium core burning for a $4 M_{\odot}$ model (Fig. 18) and a $6 M_{\odot}$ model (Fig. 19). Table 3 gives a summary of the core hydrogen burning lifetime, the core helium burning lifetime, the final extent of the convective core during central helium burning, and the final carbon mass fraction X_C in the core for each model. For the MESA models, we also show the maximum extent of the convective core during central hydrogen burning, the mass of the helium core before helium ignition, and the mass of the C/O core at the time of the first helium thermal pulse.

We close with an additional comparison of the helium core burning phase of a $M = 3 M_{\odot}$, $Z = 0.02$ model computed by MESA to that of Straniero et al. (2003). Both models were evolved using the Kunz et al. (2002) rate for $^{12}\text{C}(\alpha, \gamma)^{16}\text{O}$. The results for MESA star are a helium core burning lifetime of 83.6 Myr and final C/O mass fractions of $X_C = 0.43$, $X_O = 0.55$; Straniero et al. (2003) find a lifetime of 88 Myr and $X_C = 0.42$, $X_O = 0.56$.

5.2. Making and Cooling White Dwarfs

In the previous section, we discussed the evolution of 3–8 M_{\odot} stars up to the occurrence of the first He thermal pulse. In Paper I we showed detailed comparisons of the evolution of a $2 M_{\odot}$ star to the EVOL code (Herwig 2004), exhibiting the ability of MESA star to calculate multiple he-

Table 3

 Properties of the 3–8 M_{\odot} evolution (masses in solar units). Selected quantities are also shown from DSEP for comparison.

M/M_{\odot}	MESA							DSEP			
	$\Delta t_{\text{H}}^{(1)}$	$M_{\text{cc}}^{\text{max}(2)}$	$M_{\text{core}}^{\text{He}(3)}$	$\Delta t_{\text{He}}^{(4)}$	$M_{\text{cc}}^f{}^{(5)}$	$X_{\text{C}}^{(6)}$	$M_{\text{core}}^{\text{CO}(7)}$	$\Delta t_{\text{H}}^{(1)}$	$\Delta t_{\text{He}}^{(4)}$	$M_{\text{cc}}^f{}^{(5)}$	$X_{\text{C}}^{(6)}$
3.0	320.6	0.69	0.36	83.59	0.097	0.426	0.466	312.0	80.81	0.098	0.456
4.0	152.7	1.01	0.47	29.78	0.149	0.490	0.667	147.3	28.91	0.153	0.516
5.0	85.61	1.34	0.59	15.52	0.214	0.511	0.827	84.75	15.19	0.210	0.507
6.0	55.98	1.68	0.72	9.62	0.288	0.514	0.870	55.41	9.61	0.289	0.505
7.0	39.91	2.03	0.86	6.51	0.375	0.511	0.915	39.69	6.79	0.401	0.454
8.0	30.42	2.40	1.02	4.67	0.480	0.504	0.966	30.26	4.71	0.482	0.515

(1) Central H burning lifetime (Myr)

(2) Maximum extent of the convective core during core H burning

(3) Mass of the He core before central He ignition

(4) Central He burning lifetime (Myr)

(5) Stable final extent of the Schwarzschild convective core during core He burning

 (6) Central mass fraction of ^{12}C at the end of core He burning

(7) Mass of the C/O core at the time of the first thermal pulse

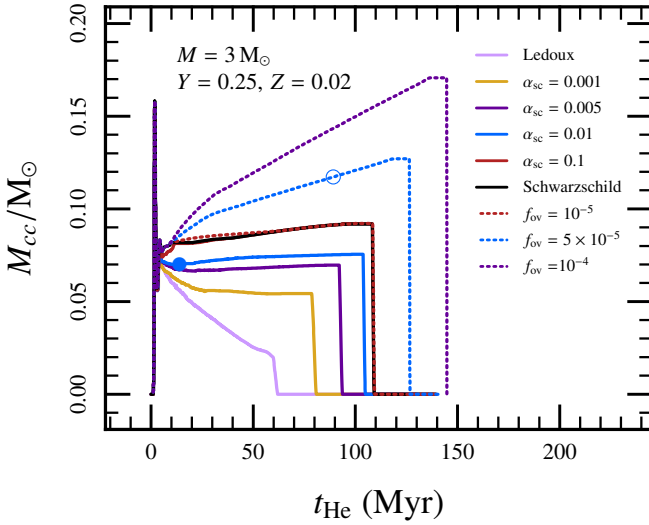


Figure 15. History of convective core extent during the core helium burning phase for a non-rotating $3 M_{\odot}$ star with various mixing options, as in Figure 13. Time is measured relative to the onset of the convective core burning. Efficient semiconvection ($\alpha_{\text{sc}} = 0.01$) and inefficient overshooting ($f_{\text{ov}} = 10^{-5}$) coincide with the pure Schwarzschild model. The filled (open) circle indicates the time for which we display a profile detailing semiconvection (overshooting) in Figure 11.

lium shell pulses. We now illustrate the final evolution of intermediate-mass stars, and how to construct white dwarfs (WDs) by using winds.

We evolve $3 M_{\odot}$, $5 M_{\odot}$, and $7 M_{\odot}$ stars from the ZAMS using the test suite case `make_co_wd`. This makes use of RGB mass loss following Reimers (1975) with an efficiency parameter $\eta = 0.5$ and AGB mass loss following Bloeker (1995) using $\eta = 0.1$ until the occurrence of the first helium shell flash. At that time, an increased Bloeker $\eta = 5$ is adopted to allow only a small number of thermal pulses before the wind mass loss eliminates the envelope. Such intervention allows MESA star to make a high-mass WD. To avoid shortening of timesteps due to radiation-dominated envelopes, these cases also use the MLT++ capability described in §7.2.

Figure 20 shows the resulting tracks on the HR diagram. The $3 M_{\odot}$ star underwent eight thermal pulses after the enhancement of Bloeker winds, while the $5 M_{\odot}$ and $7 M_{\odot}$ stars lost their envelopes so quickly that thermal pulses were immediately halted. The $5 M_{\odot}$ star ended up as an $M = 0.844 M_{\odot}$

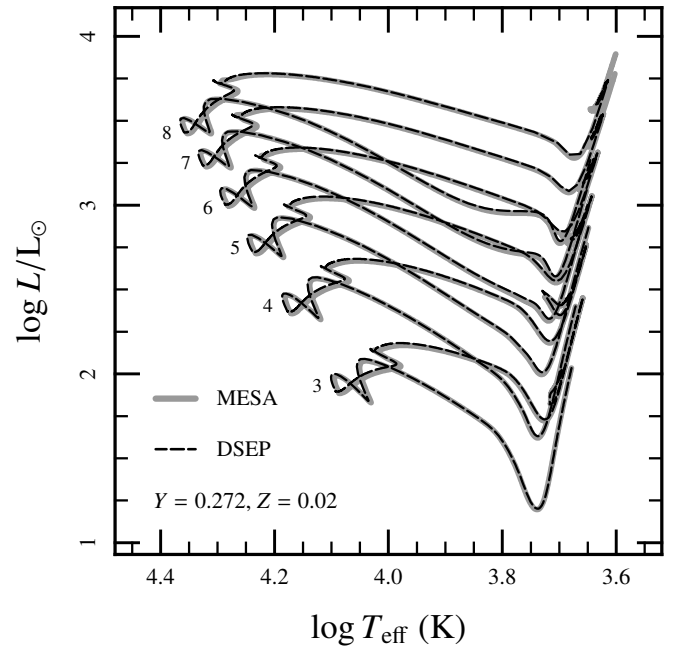


Figure 16. Hertzsprung-Russell diagram for evolution of 3–8 M_{\odot} stars from the pre-main sequence through core helium depletion. Models are from MESA (thick grey lines) and DSEP (dashed black lines). Each curve is labeled with its corresponding initial mass in solar units.

C/O WD with a helium shell of thickness $M_{\text{He}} = 0.009 M_{\odot}$ and a hydrogen envelope of $M_{\text{H}} = 2.3 \times 10^{-5} M_{\odot}$. Note that the C/O WD mass is only slightly larger than the C/O mass at the first thermal pulse ($0.827 M_{\odot}$) reported in Table 3.

After removal of the envelope, the evolution of the white dwarf is continued through its cooling phase past solidification. We include gravitational settling and chemical diffusion of the outermost layers. Figure 21 shows T – ρ profiles taken at various effective temperatures during the cooling of the $M = 0.844 M_{\odot}$ C/O WD made from the $5 M_{\odot}$ star. The growing depth of the convection zone is shown by the dashed line, and the open circles designate the H/He transition, while the filled circles denote the He/CO transition. Figure 22 illustrates the resulting L – T_{c} relation as these models cool.

The test suite case `wd_diffusion` uses the implementation of diffusion described in Paper I to evolve a WD of mass $0.611 M_{\odot}$ until the $M_{\text{H}} = 1.3 \times 10^{-4} M_{\odot}$ hydrogen layer and the $M_{\text{He}} = 4.6 \times 10^{-2} M_{\odot}$ helium layer approach diffusive

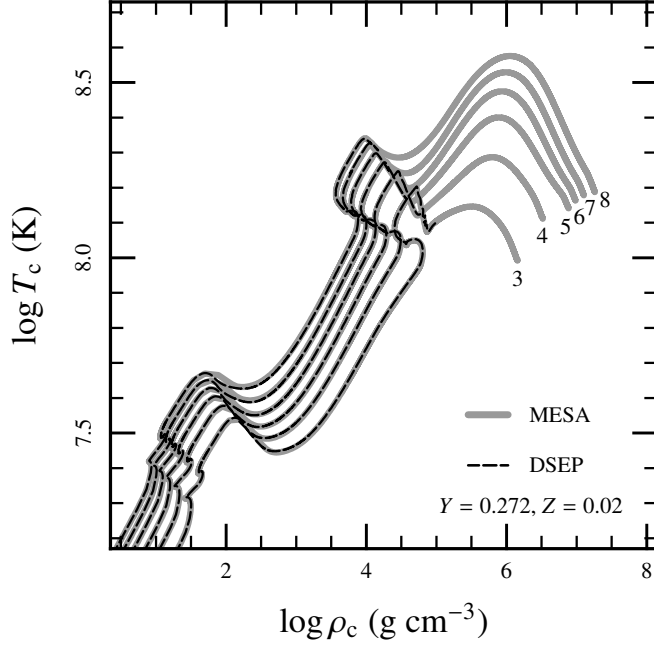


Figure 17. Same as Fig. 16, but in the T_c - ρ_c plane. The MESA models (thick grey lines) are evolved until the occurrence of the first thermal pulse.

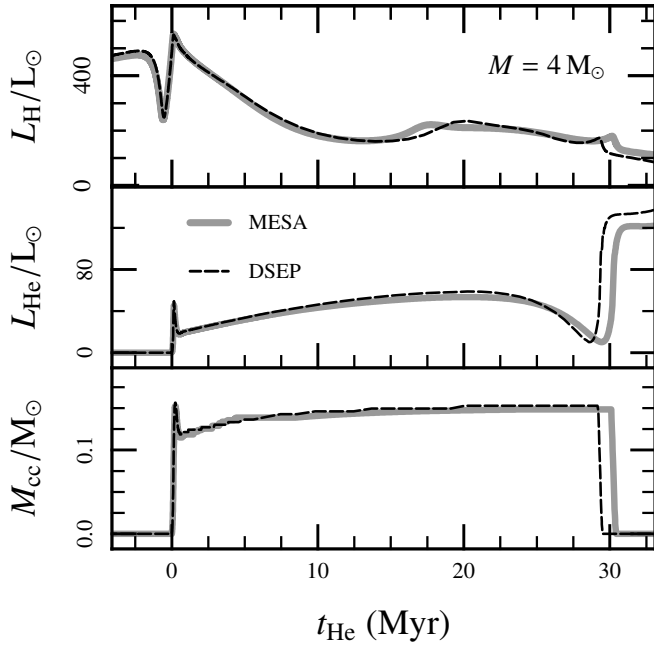


Figure 18. History of hydrogen burning luminosity (top), helium-burning luminosity (center), and convective core extent (bottom) during the core helium burning phase for the $4 M_\odot$ models. Time is measured relative to the onset of the convective core.

equilibrium. At this point, the WD has an effective temperature of $T_{\text{eff}} \approx 5,000$ K. We show the resulting abundance profiles in Figure 23, and, for comparison, the abundance profiles derived from the analytic form for diffusive equilibrium (eq. (22) of Althaus et al. 2003). This formula is obtained by integrating equation (A.5) of Arcoragi & Fontaine (1980) and assuming an ideal gas equation of state and complete ionization of both species.

The specific treatment of convection can also impact WD evolution. In Paper I, MESA used the Cox & Giuli (1968) pre-

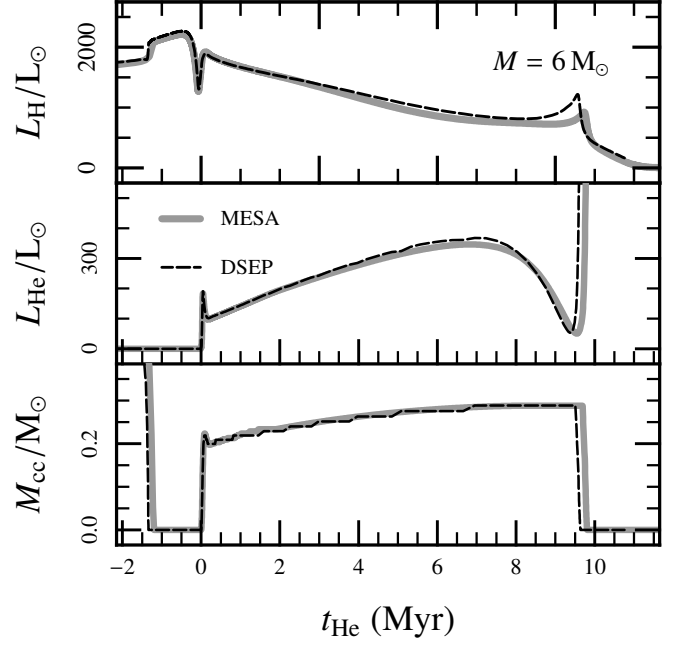


Figure 19. History of hydrogen burning luminosity (top), helium-burning luminosity (center), and convective core extent (bottom) during the core helium burning phase for the $6 M_\odot$ models. Time is measured relative to the onset of the convective core.

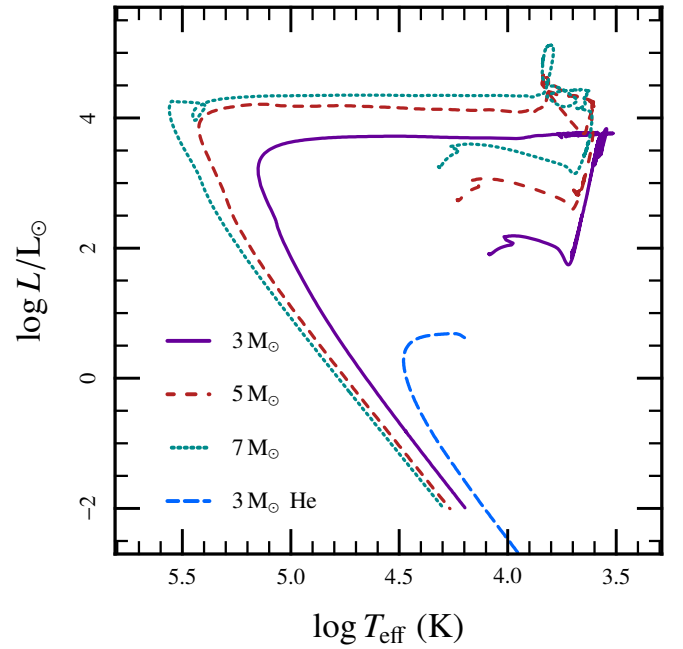


Figure 20. Evolution of $3, 5$ and $7 M_\odot$ models from zero-age main sequence to cooling white dwarfs. A Bloeker mass loss strips the stars of their envelopes on the thermally pulsing AGB to make the three C/O white dwarfs. The single $0.32 M_\odot$ He white dwarf was made with mass loss after the hydrogen main sequence for the $3 M_\odot$ model was completed.

scription for convection as its default convective MLT, with the optional extension of Henyey et al. (1965). Since Paper I, we have added support for the formulations of Böhm-Vitense (1958), Böhm & Cassinelli (1971), and Mihalas (1978). In particular, the Böhm & Cassinelli prescription, often referred to as “ML2,” is frequently employed in WD studies (e.g., Bergeron et al. 1995). In Figure 24 we show a comparison of the Brunt-Väisälä frequency calculated with MESA to that us-

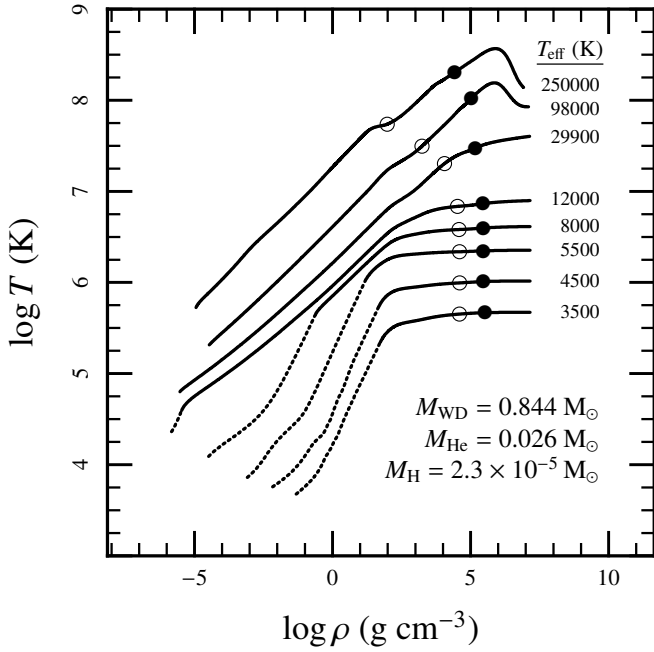


Figure 21. Profiles in $\log T$ - $\log \rho$ space of the cooling $0.844 M_{\odot}$ C/O white dwarf evolved from a $5 M_{\odot}$ progenitor. Each model is labeled to the right by T_{eff} . The outermost point of the model is at $\tau = 25$. Dotted curves denote convective regions. Going toward the interior, open circles designate the transition into the helium-rich shell, and filled circles designate the transition into the C/O core.

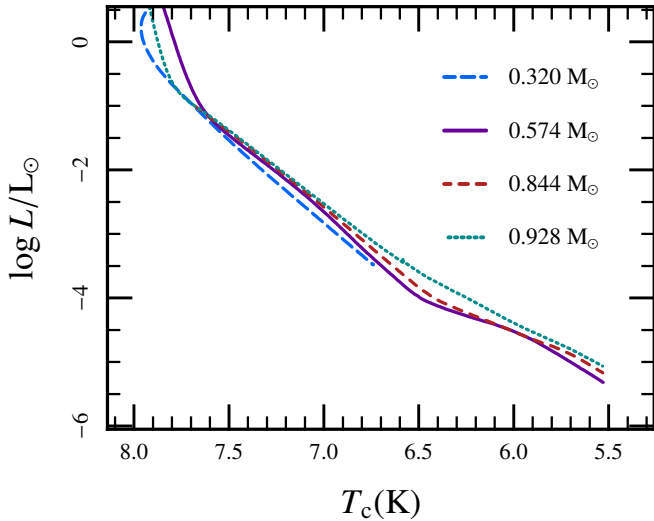


Figure 22. Surface luminosity as a function of central temperature for the cooling 0.32 , 0.574 , 0.844 , and $0.928 M_{\odot}$ WDs evolved from 3 , 5 , and $7 M_{\odot}$ progenitors.

ing the Warsaw envelope code (Paczynski 1969, 1970; Pamyatnykh 1999), assuming the ML2 prescription. This is the same WD as in Figure 23, but now at a lower $T_{\text{eff}} = 11,354$ K. To more accurately integrate these opaque but thin layers, we reduce τ at the boundary of the model by a factor of 1000 from its photospheric value of $2/3$. This calculation is a sensitive test of the envelope integrations because N^2 is a derivative of the envelope structure. The two codes give indistinguishable results for this case and all other cases that we have calculated.

MESA now includes atmospheric tables based on the non-grey model atmospheres for hydrogen-atmosphere WDs (Rohrman 2001; Rohrman et al. 2012). Such an approach is

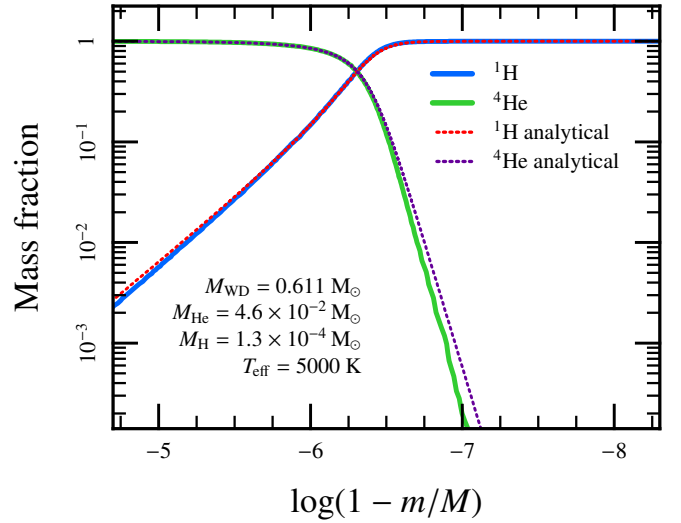


Figure 23. A comparison of time-dependent diffusion calculations for a $M = 0.611 M_{\odot}$ WD with $M_{\text{H}} = 1.3 \times 10^{-4} M_{\odot}$ and $M_{\text{He}} = 4.6 \times 10^{-2} M_{\odot}$ with MESA star (solid lines) to those assuming diffusive equilibrium and an ideal gas equation of state (dashed lines).

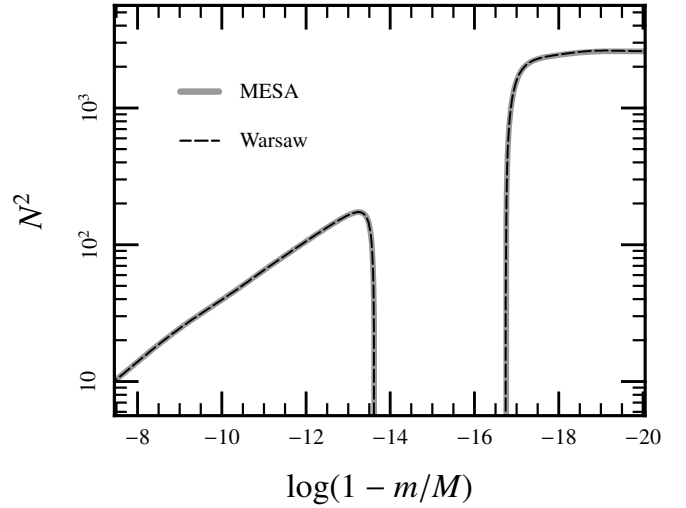


Figure 24. A comparison of the Brunt-Väisälä frequency calculated with MESA (solid grey line) to that using the Warsaw envelope code `pig35.f` (dashed line) for the same WD in Figure 23, but at a cooler $T_{\text{eff}} = 11,354$ K.

necessary at $T_{\text{eff}} \lesssim 6000$ K, where WDs develop deeper convection zones. When the convection zone comes in contact with the degenerate, nearly isothermal core, energy is able to flow out of the core much more efficiently. The use of non-grey atmosphere models results in shallower convection zones, so this convective coupling of the core and envelope is delayed. For reliable cooling ages, we therefore recommend using non-grey atmospheres when $T_{\text{eff}} \lesssim 6000$ K. Figure 25 demonstrates the impact of non-grey atmospheres with the $0.535 M_{\odot}$ WD, which was cooled with and without the non-grey atmosphere.

MESA currently treats crystallization by employing the Potekhin & Chabrier (2010) EOS (PC EOS). The phase transition is first-order, so the EOS exhibits a latent heat between the solid and liquid phases, i.e., the entropy and internal energy both experience finite jumps. This energy is included in MESA star models of cooling white dwarfs through the grav-

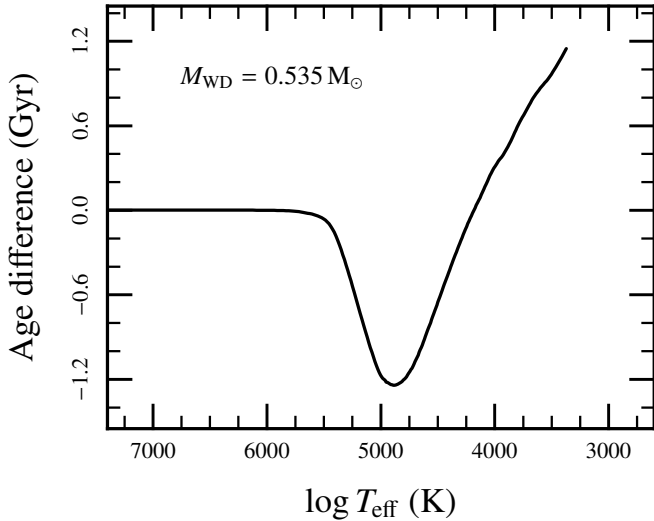


Figure 25. The age difference (non-grey minus grey) in Gyr as a function of T_{eff} .

itional source term in the energy equation,

$$\epsilon_{\text{grav}} \equiv -T \frac{dS}{dt}. \quad (15)$$

This form for ϵ_{grav} replaces the default one (see eq. (16) below) in cells where $\Gamma \geq 160$, and is smoothly interpolated with the default form in cells where $130 \leq \Gamma < 160$. The PC EOS uses the criterion $\Gamma = 175$ to determine crystallization, but it is straightforward to include explicit crystallization curves for C/O and other mixtures (e.g., Schneider et al. 2012; Medin & Cumming 2010). For example, using the parameters of the model in Figure 23, the age difference at late times ($T_{\text{eff}} < 3,500$ K) between a model with and without the latent heat of crystallization is ≈ 0.8 Gyr; a slightly larger value would be obtained using the phase diagram of Schneider et al. (2012). MESA does not currently treat phase separation of different chemical species upon crystallization.

Low mass WDs ($M \lesssim 0.4 M_{\odot}$) with helium cores and hydrogen envelopes may be produced in binary systems when the envelope is stripped by the companion as the primary evolves up the giant branch (Iben 1991, and references therein). He-core WDs of mass $M \approx 0.4\text{--}0.5 M_{\odot}$ may also be produced through strong RGB winds (D’Cruz et al. 1996), although we do not discuss this possibility further here.

Here we discuss the prescription for stripping the envelope used in the test case `make_he_wd`. The first step is to evolve a star, $M = 3.0 M_{\odot}$ in this example, from the PMS until a He core of the correct size has been made. The remnant total mass is determined by the mass interior to where the H abundance has dropped below a preset value, for example, $X_{\text{H}} = 0.1$, moving in from the surface. Next, the routine `relax_mass` is used to remove mass from the model until it has the desired remnant mass. After the initial remnant has been constructed, diffusion can then be turned on to allow an outer H layer to form. After this stage, normal evolution of the WD occurs, as shown in Figures 20 and 22.

5.3. Compressional Heating and Accretion

As discussed in §6.2 of Paper I, MESA star calculates ϵ_{grav} of eq. (15) in terms of the local thermodynamic variables (T

and ρ) used by MESA,

$$\epsilon_{\text{grav}} = -C_p T \left[\left(1 - \nabla_{\text{ad}} \chi_T \right) \frac{d \ln T}{dt} - \nabla_{\text{ad}} \chi_{\rho} \frac{d \ln \rho}{dt} \right]. \quad (16)$$

MESA star takes the quantities in this equation as provided by EOS, and computes the Lagrangian time derivatives to find ϵ_{grav} . MESA star can alternatively work under the assumption that $P = P_{\text{gas}} + P_{\text{rad}}$, in which case MESA star treats P_{gas} rather than ρ as its basic variable (see §B.2 for a discussion). In that case,

$$\epsilon_{\text{grav}} = -C_p T \left[\left(1 - 4 \nabla_{\text{ad}} \frac{P_{\text{rad}}}{P} \right) \frac{d \ln T}{dt} - \nabla_{\text{ad}} \frac{P_{\text{gas}}}{P} \frac{d \ln P_{\text{gas}}}{dt} \right]. \quad (17)$$

Either formulation can be used deep within the star, as long as the location is safely removed from any phase transition. Paper I described the validation of these formulations.

A complication arises when ϵ_{grav} needs to be evaluated in material that was not present in the previous timestep. Defining the envelope mass coordinate $\Delta M \equiv M - m$, we need to resolve the entropy for $\Delta M < \delta M = \dot{M} \delta t$, as the explicit Lagrangian time derivatives of eqs. (16) and (17) cannot be numerically evaluated. Since there can be important physics that needs to be resolved for these mass shells for $\Delta M \ll \delta M$, an approximation must be derived that allows for accurate modeling of the star’s outermost layers without having to result to a dramatic shortening of δt .

The luminosity $L_{\text{acc}} = GM\dot{M}/R$ from the accretion shock (or boundary layer) goes outwards and does not determine the entropy of the material as it becomes part of the hydrostatically adjusting star. Rather, the entropy of the material at $\Delta M \ll \delta M$ is determined by the transport of L (Nomoto & Sugimoto 1977; Nomoto 1982; Townsley & Bildsten 2004). Consider such an outermost layer, where there are two relevant timescales, the thermal time, $t_{\text{th}} = C_p T \Delta M / L$, and the local accretion time, $t_{\text{acc}} = \Delta M / \dot{M}$. In nearly all relevant cases, the ratio $t_{\text{th}} / t_{\text{acc}} = C_p T \dot{M} / L \ll 1$; this implies that the fluid element adjusts its temperature to that needed to transport the stellar luminosity from deep within. This simplifies ϵ_{grav} in that part of the star (following Townsley & Bildsten 2004) to

$$\epsilon_{\text{grav}} = \frac{C_p T G m \dot{M}}{4\pi r^4 P} (\nabla_{\text{ad}} - \nabla_T), \quad (18)$$

enabling accurate modeling within MESA star of nearly all fluid elements that become part of the star during each timestep, many of which have envelope mass coordinates $\Delta M \ll \dot{M} \delta t$.

We give an explicit example of this thin-shell radiative calculation of ϵ_{grav} in a C/O white dwarf accreting hydrogen-rich material and undergoing classical nova (CN) cycles. We present two models accreting at rates of $\dot{M} = 10^{-11} M_{\odot} \text{ yr}^{-1}$ and $10^{-10} M_{\odot} \text{ yr}^{-1}$. Both cases were evolved from a $0.6 M_{\odot}$ starting model with $T_c = 10^7$ K which had undergone a few flashes while accreting at $\dot{M} = 10^{-11} M_{\odot} \text{ yr}^{-1}$. The accreted material has solar-like composition $X = 0.70$, $Y = 0.26$, and $Z = 0.04$ where the metal mass fractions are taken from Lodders (2003).

Profiles of the envelope during the mass accumulation phase between CN outbursts for the two accretion rates are displayed in Figures 26 and 27. Each line represents a different time in the accumulation cycle up to the unstable ignition, when the hydrogen mass reaches $M_{\text{H}} = M_{\text{ign}}$. All material at pressures smaller than that shown by the open circle is new to

the model in that timestep (e.g., it has $\Delta M < \delta M$) and employs the modified ϵ_{grav} of eq. (18). This highlights the significance of this approximation as it allows MESA star to calculate material properties at $\Delta M \sim 10^{-8} \delta M$. The solid points show where ϵ_{grav} switches to the explicit form employing the Lagrangian time derivatives, such as eq. (16).

The middle panel shows $\epsilon_{\text{grav}} P \propto \epsilon_{\text{grav}} \Delta M$, which reflects the contribution of ϵ_{grav} to the outward luminosity. The discontinuity of ϵ_{grav} at the solid point reflects the error associated with the abrupt transition in the calculational approach. The substantially larger luminosity of the early ($M_{\text{H}}/M_{\text{ign}} = 0.22$) stages is due to the ongoing transfer of heat from the previous outburst. The near-discontinuous drop in ϵ_{grav} occurs at the base of the hydrogen-rich envelope, and reflects the jump in composition from the accreted material to the nearly pure ${}^4\text{He}$ layer. The expected amplitude of the jump in ϵ_{grav} depends on both the composition jump and the local degree of electron degeneracy (see Appendix B of Townsley & Bildsten 2004 for a discussion).

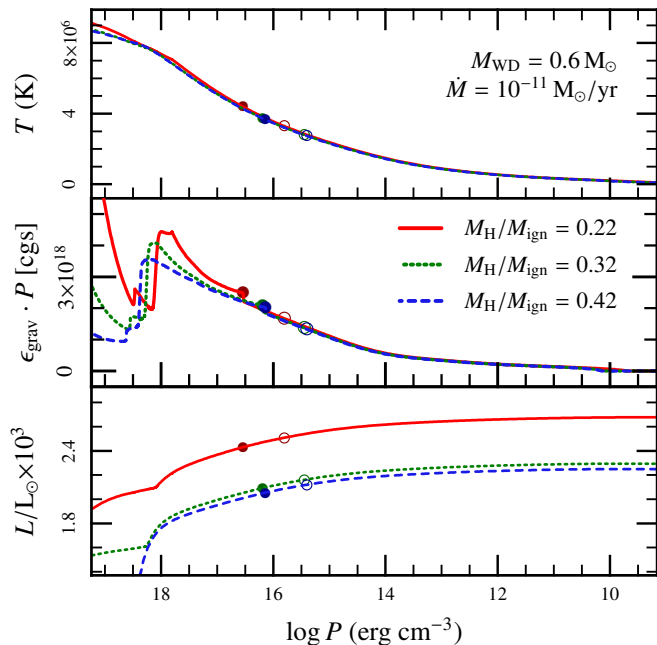


Figure 26. Envelope profiles as a function of pressure of the accreting white dwarf for three instants during the mass accumulation phase; $\dot{M} = 10^{-11} M_{\odot} \text{yr}^{-1}$ model. The top panel shows temperature, the central panel shows the gravitational energy release rate, and the bottom shows the luminosity. Material to the right of the open circle is newly accreted. The code treats material to the right of the filled circle using the thin-shell radiative calculation of ϵ_{grav} .

6. ROTATION

A star’s rotational energy is usually a small fraction of the gravitational energy: for the Sun it is $\sim 10^{-5}$ and for a $25 M_{\odot}$ star rotating with a typical equatorial velocity $v_{\text{eq}} = 200 \text{ km s}^{-1}$ on the main sequence it is ~ 0.04 . Therefore the effects on the stellar hydrostatic equilibrium are marginal, with the exception of stars close to critical rotation (see §6.3). Even in the case of a small perturbation to hydrostatic equilibrium, rotation induces a modification to the star’s thermal equilibrium (von Zeipel 1924). Together with the emergence of rotationally-induced dynamical and secular instabilities, this can significantly affect the evolution of stars (Maeder &

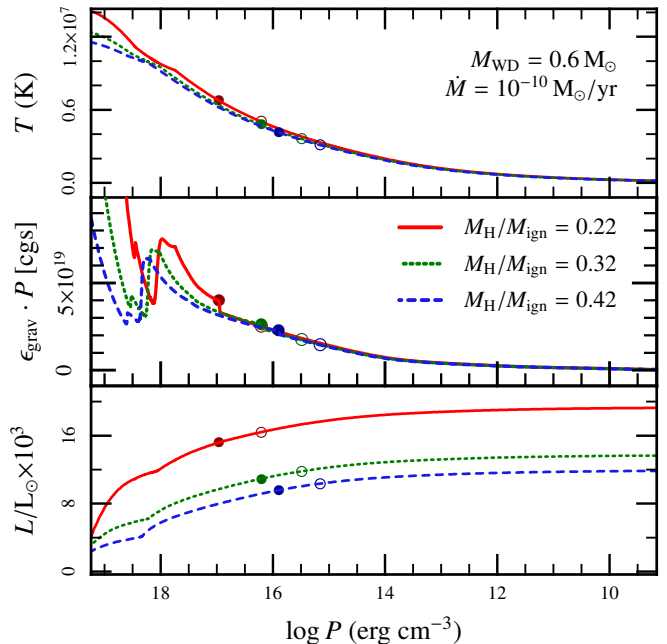


Figure 27. Same as Fig. 26, but for model accreting $10^{-10} M_{\odot} \text{yr}^{-1}$.

Meynet 2000b). Due to the destabilizing effect of increasing radiation pressure, rotation is particularly important in massive stars (see, e.g., Heger et al. 2000; Meynet & Maeder 2000). Moreover, the final fate of a massive star depends chiefly on the relative importance of rotation during its evolution (e.g., Heger et al. 2000; Hirschi et al. 2004; Heger et al. 2005; Yoon et al. 2006; Woosley & Heger 2006; Ekström et al. 2012; Georgy et al. 2012; Langer 2012).

Here we describe the implementation of rotation in MESA star. We briefly discuss the modification to the stellar structure equations and the inclusion of rotationally- and magnetically-induced mixing. Magnetic fields generated by differential rotation in radiative regions have been implemented following the work of Spruit (2002) and in the same fashion as in Petrovic et al. (2005) and Heger et al. (2005). Rotationally enhanced mass loss is also discussed.

We compare rotating massive-star models calculated with MESA star to previous calculations performed with KEPLER (Heger et al. 2005). We also directly compare runs from MESA star and STERN (Petrovic et al. 2005; Yoon & Langer 2005; Brott et al. 2011). The purpose of these tests is to verify our implementation of rotation, which is derived from STERN. We do not compare to codes that have a different implementation of rotation (e.g., Hirschi et al. 2004; Ekström et al. 2012; Georgy et al. 2012; Potter et al. 2012b,a). Although beyond the scope of this paper, such comparisons are critical when coupled to observations of the effects of rotation in stars (e.g., Hunter et al. 2007; Evans et al. 2011) and asteroseismology (Beck et al. 2012; Mosser et al. 2012).

6.1. Implementation of Shellular Rotation

Stellar structure deviates from spherical symmetry in the presence of rotation. While the structure is inherently three-dimensional, it suffices to solve the stellar structure equations in one dimension if the angular velocity, ω , is constant over isobars (the so-called shellular approximation; see, e.g., Meynet & Maeder 1997). This is expected in the presence of strong anisotropic turbulence acting along isobars. In radiative regions such turbulence is a consequence of differential

rotation (Zahn 1992) and efficiently erases gradients along isobars and enforces shellular rotation (Meynet & Maeder 1997). Turbulence in the vertical direction (i.e., perpendicular to the isobars) is much weaker due to the stabilizing effect of stratification. In MESA star we adopt the shellular approximation (Meynet & Maeder 1997) and calculate the modification to the stellar equations due to centrifugal acceleration (Kippenhahn & Thomas 1970; Endal & Sofia 1976).

Transport of angular momentum and chemicals due to rotationally-induced instabilities is implemented in a diffusion approximation (e.g., Endal & Sofia 1978; Pinsonneault et al. 1989; Heger et al. 2000). This choice has also been adopted by other stellar evolution codes (e.g., KEPLER, Heger et al. 2000; STERN, Yoon & Langer 2005). We stress that this is not the only possibility, and other groups have implemented a diffusion-advection approach (e.g., GENEVA, Eggenberger et al. 2008; RoSE, Potter et al. 2012b). The RoSE code can switch between the two different implementations. The two approaches are equivalent for the transport of chemicals. Potentially large differences can arise, however, for the transport of angular momentum. A detailed description of the advection-diffusion equation for angular momentum is given in Zahn (1992) and Maeder & Zahn (1998).

In MESA star the turbulent viscosity ν is determined as the sum of the diffusion coefficients for convection, semiconvection, and rotationally-induced instabilities. MESA star calculates diffusion coefficients for five different rotationally-induced mixing processes: dynamical shear instability, Solberg-Høiland instability, secular shear instability, Eddington-Sweet circulation, and the Goldreich-Schubert-Fricke instability. See Heger et al. (2000) for a detailed description of the physics of the different instabilities and the calculation of the respective diffusion coefficients. These enter the angular momentum and abundance diffusion equations that are solved at each timestep (see §B.6).

6.2. Magnetic Fields

Differential rotation in the radiative layers of a star can amplify a seed magnetic field. Such a dynamo process has been suggested by Spruit (2002, Spruit-Tayler dynamo); a debate on this is still ongoing (Braithwaite 2006; Zahn et al. 2007; Denissenkov & Pinsonneault 2007). Observations of the final spins of both WDs and neutron stars (Heger et al. 2005; Suijs et al. 2008) suggest that angular momentum transport with an efficiency similar to the torques provided by the Spruit-Tayler dynamo operates. Models that only include angular momentum transport through rotational instabilities do not produce the core-envelope ratio of angular velocity observed through the splitting of mixed modes in red giant stars (Eggenberger et al. 2012).

MESA star accounts for transport by magnetic fields of angular momentum and chemicals due to the Spruit-Tayler dynamo. We refer to Spruit (2002) for a description of the physics of the dynamo loop and to Maeder & Meynet (2003), Maeder & Meynet (2004) and Heger et al. (2005) for a discussion of its inclusion in stellar evolution codes. We implement the Spruit-Tayler dynamo in MESA star following KEPLER (Heger et al. 2005) and STERN (Petrovic et al. 2005).

6.3. Rotationally-Enhanced Mass Loss

We include the rotational modification to the mass loss rate (Friend & Abbott 1986; Langer 1998; Heger & Langer 1998; Maeder & Meynet 2000a). Similar to other codes (e.g.,

Heger et al. 2000; Brott et al. 2011; Potter et al. 2012a), in MESA star the stellar mass loss is enhanced as the rotation rate increases according to the prescription

$$\dot{M}(\Omega) = \dot{M}(0) \left(\frac{1}{1 - \Omega/\Omega_{\text{crit}}} \right)^{\xi}, \quad (19)$$

where Ω is the value of the surface angular velocity and Ω_{crit} is the critical angular velocity at the surface. This last quantity is defined as $\Omega_{\text{crit}}^2 = (1 - L/L_{\text{Edd}})GM/R^3$, where $L_{\text{Edd}} = 4\pi cGM/\kappa$ is calculated as a mass-weighted average in a user-specified optical depth range (default value $\tau \in [1 - 100]$). In MESA star the default value for the exponent ξ is 0.43 (Langer 1998). Other implementations of rotationally enhanced mass loss can be found in Maeder & Meynet (2000a) and Georgy et al. (2011).

For stars approaching $\Omega/\Omega_{\text{crit}} = 1$, the mass loss calculated using equation (19) diverges. Notice that luminous stars can approach this limit without having to rotate very rapidly as $\Omega_{\text{crit}} \rightarrow 0$ when $L/L_{\text{Edd}} \rightarrow 1$. Following Yoon et al. (2010) we limit the mass loss timescale to the thermal timescale of the star τ_{KH}

$$\dot{M} = \min \left[\dot{M}(\Omega), f \frac{M}{\tau_{\text{KH}}} \right] \quad (20)$$

where f is an efficiency factor of order unity (default value is $f = 0.3$).

6.4. Test Cases: 15 M_{\odot} and 25 M_{\odot}

As a first test we initialize a 15 M_{\odot} model with $Z = 0.02$ and initial equatorial rotational velocity $v_{\text{eq}} = 200 \text{ km s}^{-1}$ and run two calculations:

- 15MAG includes the effects of rotation and Spruit-Tayler magnetic fields on both the transport of chemicals and angular momentum.
- 15ROT includes only the effect of rotation on both the transport of chemicals and angular momentum;

The initial conditions have been calibrated to match as closely as possible the KEPLER 15 M_{\odot} models (Heger et al. 2005). Moreover, we directly compare the MESA star models with calculations from STERN (see e.g., Yoon & Langer 2005; Yoon et al. 2006). In particular we adopt a value of $f_c = 1/30$ for the ratio of the turbulent viscosity to the diffusion coefficient and a value $f_{\mu} = 0.1$ for the sensitivity to μ -gradients (see Heger et al. 2000, for a discussion of these calibration parameters). The Ledoux criterion is used for the treatment of convective boundaries, together with semiconvection ($\alpha_{\text{sc}} = 1$). We use $\alpha_{\text{MLT}} = 1.6$, mass loss as in Yoon et al. (2006) with rotational enhancement as described in § 6.3.

In Fig. 28 we show the evolutionary track and the evolution of surface equatorial rotational velocity for the 15MAG model. Results of a similar calculation using STERN are shown as a dashed curve. The two results are in excellent agreement. Small differences in luminosity and lifetimes are not unexpected, as we have only matched the physics of rotation between the two calculations and not other ingredients. Values for the diffusion coefficients for rotationally induced mixing and magnetic torques during the main sequence of 15MAG are shown in Fig. 29. The comparison reveals a very good agreement. Both stars are kept in solid-body rotation during the main sequence by the efficient transport of angular

momentum provided by the Eddington-Sweet circulation and Spruit-Taylor magnetic fields.

The amplitude and location of the azimuthal (B_ϕ) and radial (B_r) components of the magnetic fields during different phases of the evolution of 15MAG are shown in Fig. 30. As expected, these fields are generated only in radiative regions of the star and $B_\phi > B_r$ (Spruit 2002). As the star evolves away from the main sequence its structure departs from solid-body rotation with the core rotating faster than the envelope. During this stage the role of magnetic fields is very important in transporting angular momentum from the core to the envelope. The effect can be seen in Fig. 31, which shows the evolution of the internal specific angular momentum in models 15ROT and 15MAG. The presence of magnetic torques results in a dramatic spin-down of the core of 15MAG with respect to 15ROT (see also Table 4). These results are in very good agreement with the ones obtained by STERN and KEPLER.

As a second test, we now evolve a 25 M_\odot model (25MAG) with the same physics as in 15MAG. Figure 32 directly compare results with calculations performed with STERN. In Fig. 33 we show a detailed comparison of the evolution of the internal specific angular momentum profile. We find a very good quantitative agreement between MESA star and STERN down to He depletion in the core. The timescale for nuclear burning decreases substantially after He-burning and becomes shorter than the angular momentum transport timescale after C depletion. Thus only minor changes in the final angular momentum content of the stellar core are expected after this stage. Figure 34 shows the full evolution of the specific angular momentum profile of the MESA star calculation from ZAMS to Si exhaustion.

6.5. Rapidly Rotating Massive Stars

MESA star can calculate the evolution to core collapse of rapidly rotating massive stars. Rotational instabilities can be efficient enough to erase the compositional gradients built by nuclear burning. In such cases the model never develops a compositional stratification and remains almost completely mixed throughout its evolution (Maeder 1987b; Yoon & Langer 2005; Woosley & Heger 2006). This process leads to a bifurcation in the HR-diagram, with stars above a certain mass and rotation rate becoming more luminous and hotter. The threshold required for this bifurcation depends mostly on the initial mass of the star (Yoon et al. 2006). Metallicity also plays an important role, as angular momentum is lost through line-driven stellar winds, with mass-loss rates depending on the metallicity at the stellar surface (Vink et al. 2001). For the calculations in this section, we adopt the same mass-loss prescription of Yoon et al. (2006).

Figure 35 shows the evolution of two 16 M_\odot models at metallicity $Z = 0.0002$ with rotation initialized at the ZAMS. One model is rotating very rapidly, with $v_{\text{eq}} = 450 \text{ km s}^{-1}$ (corresponding to $\Omega/\Omega_{\text{crit}} = 0.55$ and $J = 3.23 \times 10^{52} \text{ ergs s}$), while the other rotates at $v_{\text{eq}} = 280 \text{ km s}^{-1}$ (corresponding to $\Omega/\Omega_{\text{crit}} = 0.4$ and $J = 2.52 \times 10^{52} \text{ ergs s}$). The model with $\Omega/\Omega_{\text{crit}} = 0.55$ avoids the core-envelope structure and becomes a compact Wolf-Rayet star. The absence of a RSG phase eliminates the large magnetic torques from an extended envelope. The evolution of the internal profile of specific angular momentum in the two models clarify this point: the model with $\Omega/\Omega_{\text{crit}} = 0.4$ becomes a RSG, and the core spins down rapidly. When it reaches core-collapse its struc-

ture is extended, as implied by the large free-fall timescale shown in the left panel of Fig. 35. As a consequence, there is not enough angular momentum in its core to build an accretion disk around a newly formed compact object. This model is expected to produce a Type IIP supernova. On the contrary, the model with $\Omega/\Omega_{\text{crit}} = 0.55$ is compact (the free-fall timescale is on the order of seconds, right panel of Fig. 35) and has enough angular momentum to produce an accretion disk around the central compact object. Therefore this model is a candidate progenitor for a long gamma-ray burst (Woosley 1993). This last calculation can be directly compared to the KEPLER model 16TI in Woosley & Heger (2006).

We further test MESA capabilities by evolving two rotating 40 M_\odot models at $Z = 10^{-5}$. One model is initialized at the ZAMS with $v_{\text{eq}} = 260 \text{ km s}^{-1}$, while the other has $v_{\text{eq}} = 630 \text{ km s}^{-1}$. The results of these calculations can be compared with the models shown in Yoon & Langer (2005). Figure 36 shows that for the more rapidly rotating model, rotational mixing (mainly due to the Eddington-Sweet circulation) is large enough that the star evolves blueward in the HR-diagram. This evolution results in a compact configuration and enough angular momentum to fulfill the requirements of the collapsar scenario for long gamma-ray bursts, as shown in Fig. 37 (right panel). On the other hand, the slower rotating model becomes a RSG and loses most of its core angular momentum, as shown in Fig. 37 (left panel).

7. MASSIVE STELLAR EVOLUTION

Modeling massive stars is numerically difficult. One problem is they develop loosely bound, radiation pressure dominated envelopes that can cause density and gas pressure inversions. This environment poses a physical and numerical challenge that all stellar evolution codes must address to evolve massive stars past the main sequence. In this section we discuss MESA star's capability to evolve rotating massive stars from their zero age main sequence to core-collapse.

7.1. Evolution of Massive Stars with MESA

Previous computations with MESA star found these envelopes to be numerically (and probably physically) unstable. This is a known issue in the literature (e.g., Maeder 1987a), which reveals the limitations of the 1D treatment of late phases of evolution of massive stars. The evolution of stars with radiation-dominated envelopes can require prohibitively short timesteps in MESA star if the standard mixing length theory is adopted. This problem usually appears during the evolution of high mass and/or high metallicity stars after hydrogen-core burning and prevents evolution to core collapse. We discuss in 7.2 our treatment of superadiabatic convection in these envelopes, which allows uninterrupted evolution, from ZAMS to core collapse.

Since it is relevant to later discussions we start with a plot of the OPAL opacity data (Iglesias & Rogers 1996) and 60 M_\odot ZAMS models in Figure 38. The plot is inspired by Figure 1 of Cantiello et al. (2009). The left-hand panel of Figure 38 shows the OPAL data for five different Z values at constant $X = 0.7$ and $\log(\rho/T_6^3) = -5$, where T_6 is the temperature in units of 10^6 K . The right-hand panel shows the opacity profiles of five 60 M_\odot ZAMS models for the same five Z values. The model profiles exhibit the same general behavior in the opacity-temperature profile as the raw opacity data. Of particular importance are the iron opacity bumps that occur at

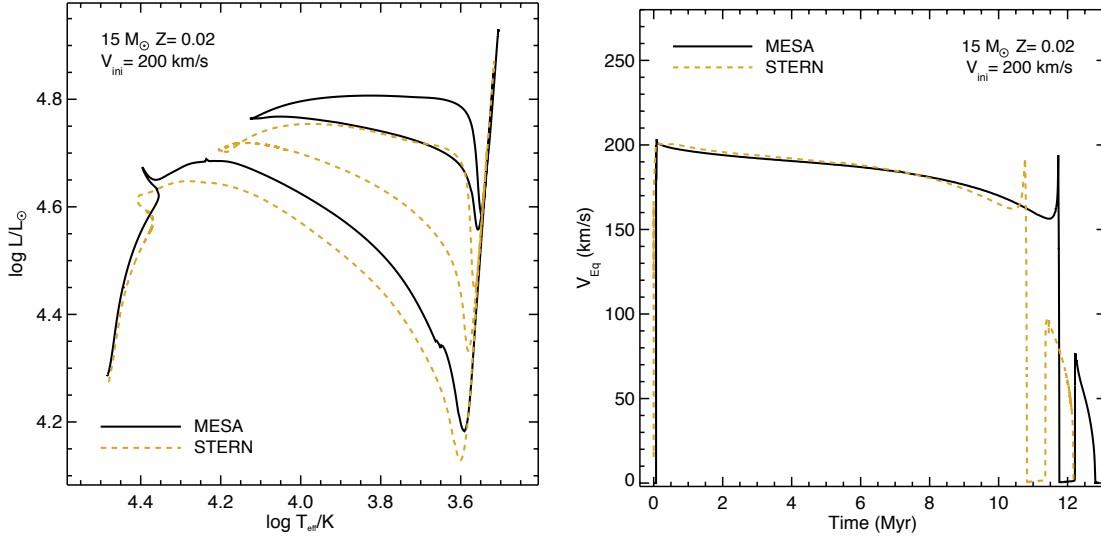


Figure 28. Comparison of evolutionary tracks (left) and equatorial rotational velocities (right) for a $15 M_{\odot}$ model with $Z = 0.02$ rotating initially with $v_{\text{eq}} = 200 \text{ km s}^{-1}$ (15MAG). The solid black line shows MESA star results, and the dashed gold line shows the STERN calculations.

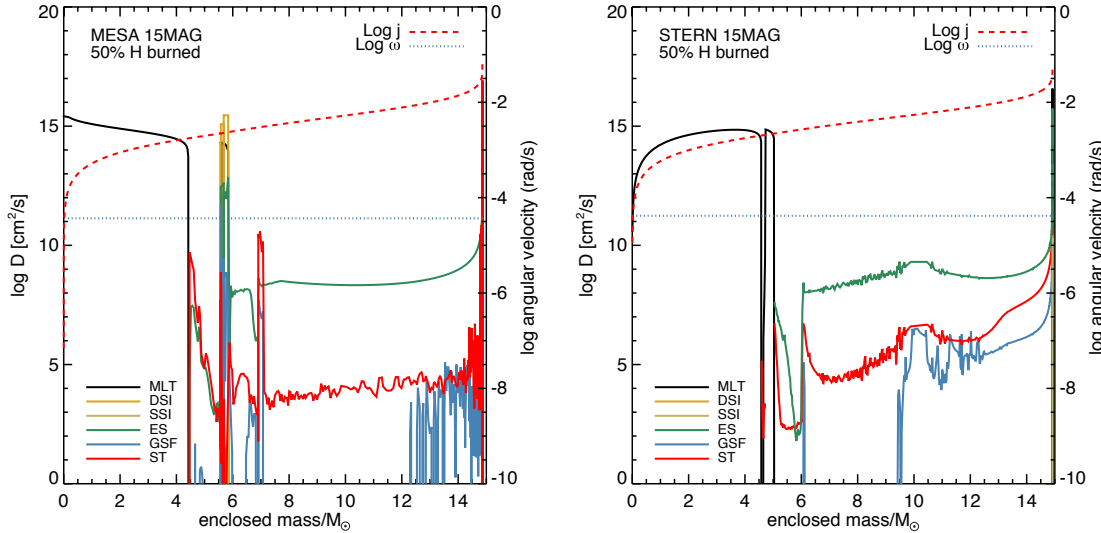


Figure 29. Same as Fig. 28. As function of mass coordinate we plot the values of the diffusion coefficient for convection (MLT), Eddington-Sweet circulation (ES), magnetic torques by dynamo generated fields (TS), Dynamical Shear (DSI), Secular Shear (SSI) and Goldreich-Schubert-Fricke (GSF) instability. Following STERN, we turn off the Solberg-Høiland instability (SH) for this comparison. This does not affect the results, as the diffusion coefficient for SH is usually smaller than the ones for ES and TS. The values of the specific angular momentum j and the angular velocity ω are also plotted. Left panel shows the results using MESA star, while the right panel shows analogous STERN calculations.

$\log T \approx 5.3$ and 6.3 . These bumps cause both the local radiation pressure to dominate and the luminosity to approach the Eddington luminosity L_{Edd} .

Where both the pressure is dominated by radiation and L_{rad} approaches L_{Edd} , specific conditions can be reached that cause convection and inversions in density and gas pressure. To define the conditions under which these occur, we follow the discussion of Joss et al. (1973), going from high to low L_{rad} . We assume that $dT/dr < 0$, $dP/dr < 0$, and that the inertial terms in the momentum equation are small. First, we establish a condition for the occurrence of an inversion in the gas pressure P_{gas} . Recasting the equation for the temperature gradient gives

$$L_{\text{rad}} = -\frac{4\pi r^2 c}{\rho \kappa} \frac{dP_{\text{rad}}}{dr}, \quad (21)$$

and using the equation of hydrostatic equilibrium, one obtains

$$\frac{dP_{\text{rad}}}{dP} = \frac{L_{\text{rad}}}{L_{\text{Edd}}}. \quad (22)$$

Writing $dP_{\text{gas}}/dr = d(P - P_{\text{rad}})/dr$ and using equation (22) and the fact that both P_{rad} and P monotonically decrease with r , one obtains

$$\frac{dP_{\text{gas}}}{dr} = \left(\frac{dP_{\text{rad}}}{dr} \right) \left[\frac{L_{\text{Edd}}}{L_{\text{rad}}} - 1 \right]. \quad (23)$$

Since $dP_{\text{rad}}/dr < 0$, equation (23) implies that for $L_{\text{rad}} > L_{\text{Edd}}$, the gas pressure gradient will increase outward, $dP_{\text{gas}}/dr > 0$, as shown by Joss et al. (1973).

The next step is to establish the condition for a density inversion to occur. Writing the gas equation of state as $P_{\text{gas}} =$

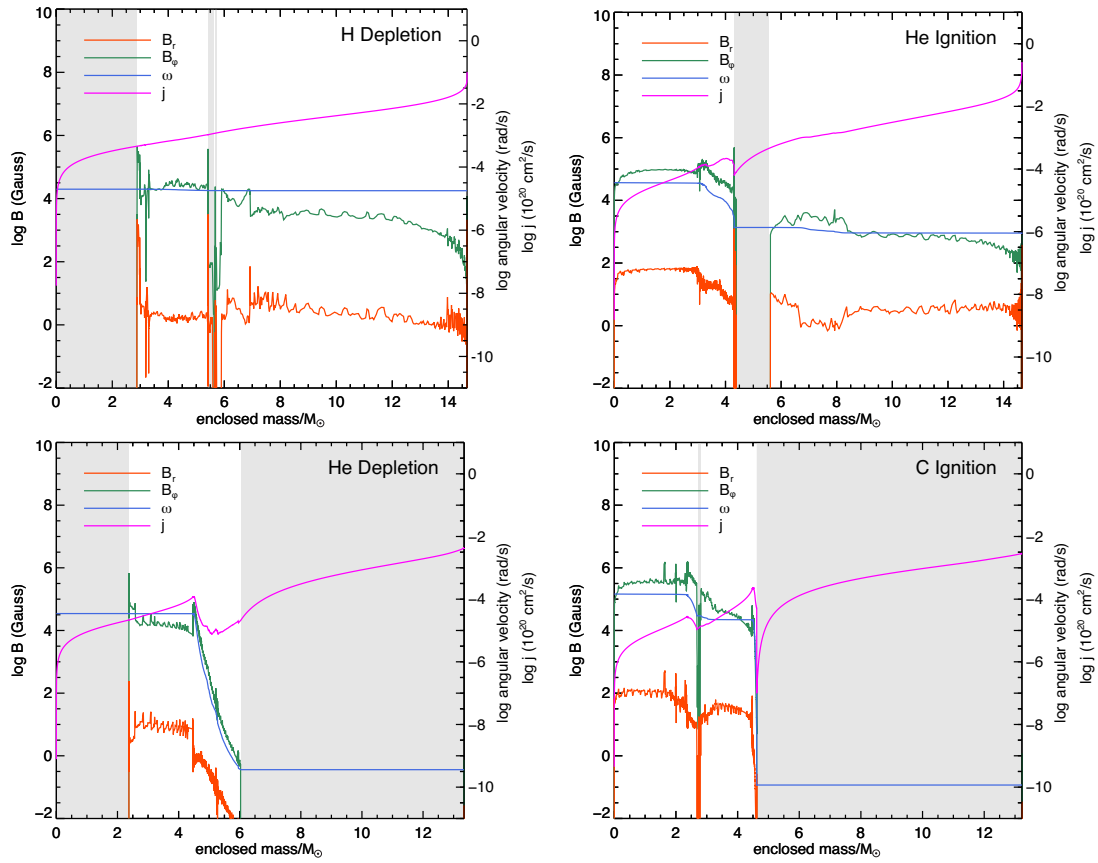


Figure 30. Magnetic field structure and angular momentum distribution for model 15MAG at different evolutionary stages (see Table 4). The curves show profiles for specific angular momentum (j), angular velocity (ω), azimuthal and radial components of magnetic field (B_{ϕ} and B_r). The shaded regions represent convective parts of the star. Compare with Fig. 1 in Heger et al. (2005).

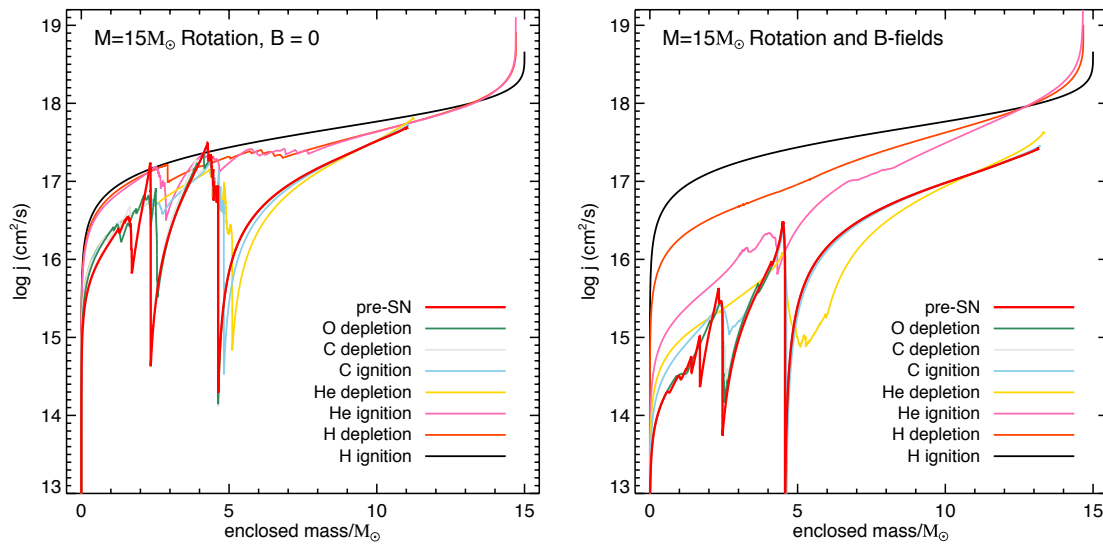


Figure 31. Specific angular momentum distribution at different evolutionary stage for 15MAG and 15ROT. See Table 4 for the definitions of these times. Compare with Fig. 2 in Heger et al. (2005).

Table 4

Evolution of Angular Momentum at Fiducial Mass Coordinates for a $Z = 0.02$, $15 M_{\odot}$ star initially rotating with $v_{\text{eq}} = 200 \text{ km s}^{-1}$ with and without the inclusion of magnetic fields.

Evolution Stage		15MAG			15ROT		
		J(1.5)	J(2.5)	J(3.5)	J(1.5)	J(2.5)	J(3.5)
ZAMS	MESA	1.82×10^{50}	4.38×10^{50}	7.90×10^{50}	1.82×10^{50}	4.38×10^{50}	7.90×10^{50}
	KEPLER ^a	1.75×10^{50}	4.20×10^{50}	7.62×10^{50}	2.30×10^{50}	5.53×10^{50}	1.00×10^{51}
	STERN ^b	1.76×10^{50}	4.27×10^{50}	7.74×10^{50}	1.76×10^{50}	4.28×10^{50}	7.76×10^{50}
H-burn ^c	MESA	1.25×10^{50}	3.03×10^{50}	5.51×10^{50}	1.64×10^{50}	3.99×10^{50}	7.26×10^{50}
	KEPLER	1.31×10^{50}	3.19×10^{50}	5.83×10^{50}	1.51×10^{50}	3.68×10^{50}	6.72×10^{50}
	STERN	1.21×10^{50}	2.96×10^{50}	5.40×10^{50}	1.62×10^{50}	3.97×10^{50}	7.25×10^{50}
H-dep ^d	MESA	4.32×10^{49}	1.08×10^{50}	2.03×10^{50}	1.54×10^{50}	3.86×10^{50}	6.44×10^{50}
	KEPLER	5.02×10^{49}	1.26×10^{50}	2.37×10^{50}	1.36×10^{50}	3.41×10^{50}	6.37×10^{50}
	STERN	4.81×10^{49}	1.21×10^{50}	2.29×10^{50}	1.48×10^{50}	3.74×10^{50}	6.99×10^{50}
He-ign ^e	MESA	4.56×10^{48}	1.36×10^{49}	3.46×10^{49}	1.37×10^{50}	3.63×10^{50}	5.35×10^{50}
	KEPLER	4.25×10^{48}	1.21×10^{49}	2.57×10^{49}	1.16×10^{50}	2.98×10^{50}	4.87×10^{50}
	STERN	4.10×10^{48}	1.16×10^{49}	3.25×10^{49}	1.33×10^{50}	3.47×10^{50}	6.36×10^{50}
He-burn ^f	MESA	2.71×10^{48}	7.23×10^{48}	1.52×10^{49}	7.48×10^{49}	1.98×10^{50}	3.93×10^{50}
	KEPLER	2.85×10^{48}	7.84×10^{48}	1.83×10^{49}	7.06×10^{49}	1.85×10^{50}	3.86×10^{50}
	STERN	3.30×10^{48}	8.57×10^{48}	1.87×10^{49}	8.46×10^{49}	2.16×10^{50}	4.39×10^{50}
He-dep ^g	MESA	2.10×10^{48}	5.65×10^{48}	1.22×10^{49}	5.40×10^{49}	1.44×10^{50}	2.81×10^{50}
	KEPLER	2.23×10^{48}	5.95×10^{48}	1.21×10^{49}	4.72×10^{49}	1.26×10^{50}	2.52×10^{50}
	STERN	2.70×10^{48}	7.17×10^{48}	1.51×10^{49}	6.80×10^{49}	1.75×10^{50}	3.41×10^{50}
C-ign ^h	MESA	1.54×10^{48}	5.21×10^{48}	8.89×10^{48}	5.40×10^{49}	1.44×10^{50}	2.58×10^{50}
	KEPLER	1.88×10^{48}	5.52×10^{48}	1.12×10^{49}	4.69×10^{49}	1.26×10^{50}	2.46×10^{50}
	STERN	1.56×10^{48}	5.58×10^{48}	1.04×10^{49}	5.85×10^{49}	1.59×10^{50}	2.79×10^{50}
C-dep ⁱ	MESA	7.54×10^{47}	3.84×10^{48}	6.71×10^{48}	5.11×10^{49}	1.39×10^{50}	2.09×10^{50}
	KEPLER	8.00×10^{47}	3.26×10^{48}	9.08×10^{48}	4.06×10^{49}	1.25×10^{50}	2.24×10^{50}
	STERN	9.04×10^{47}	4.48×10^{48}	9.33×10^{48}	5.04×10^{49}	1.56×10^{50}	2.61×10^{50}
O-dep ^j	MESA	7.52×10^{47}	3.71×10^{48}	6.41×10^{48}	4.61×10^{49}	1.37×10^{50}	1.97×10^{50}
	KEPLER	7.85×10^{47}	3.19×10^{48}	8.43×10^{48}	3.94×10^{49}	1.20×10^{50}	1.99×10^{50}
Si-dep ^k	MESA	7.28×10^{47}	3.64×10^{48}	5.90×10^{48}	4.03×10^{49}	1.22×10^{50}	1.76×10^{50}
	KEPLER	7.76×10^{47}	3.05×10^{48}	7.23×10^{48}	3.75×10^{49}	1.16×10^{50}	1.95×10^{50}

NOTE: ^a Results from Table 1 of Heger et al. (2005); ^b See e.g., Petrovic et al. (2005); Yoon & Langer (2005); Yoon et al. (2006); ^c 40% central hydrogen mass fraction; ^d 1% hydrogen left in the core; ^e 1% helium burnt; ^f 50% central helium mass fraction; ^g 1% helium left in the core; ^h central temperature of $5 \times 10^8 \text{ K}$; ⁱ central temperature of $1.2 \times 10^9 \text{ K}$; ^j central oxygen mass fraction drops below 5%; ^k central Si mass fraction drops below 10^{-4} ;

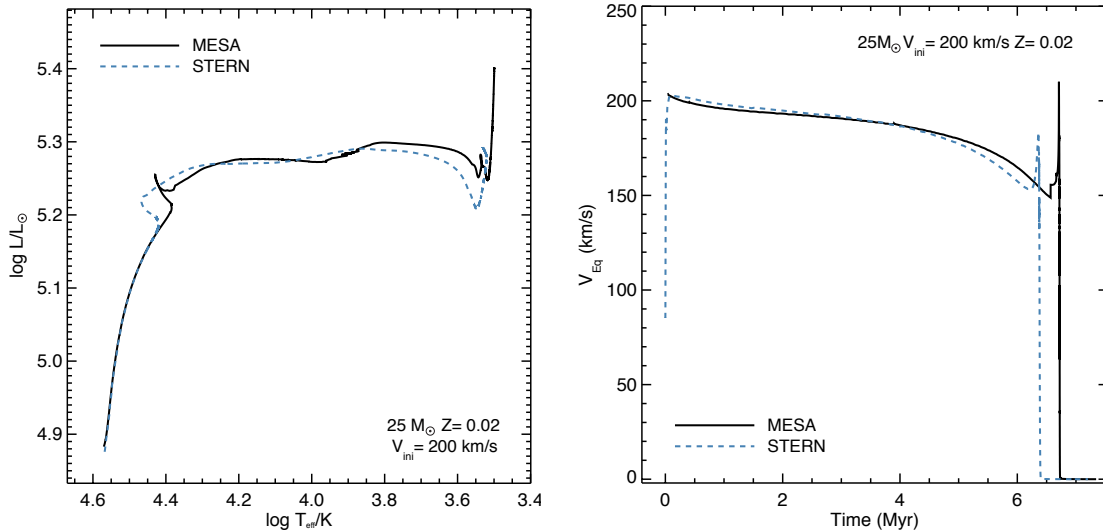


Figure 32. Same as Fig. 28, except for the 25MAG model.

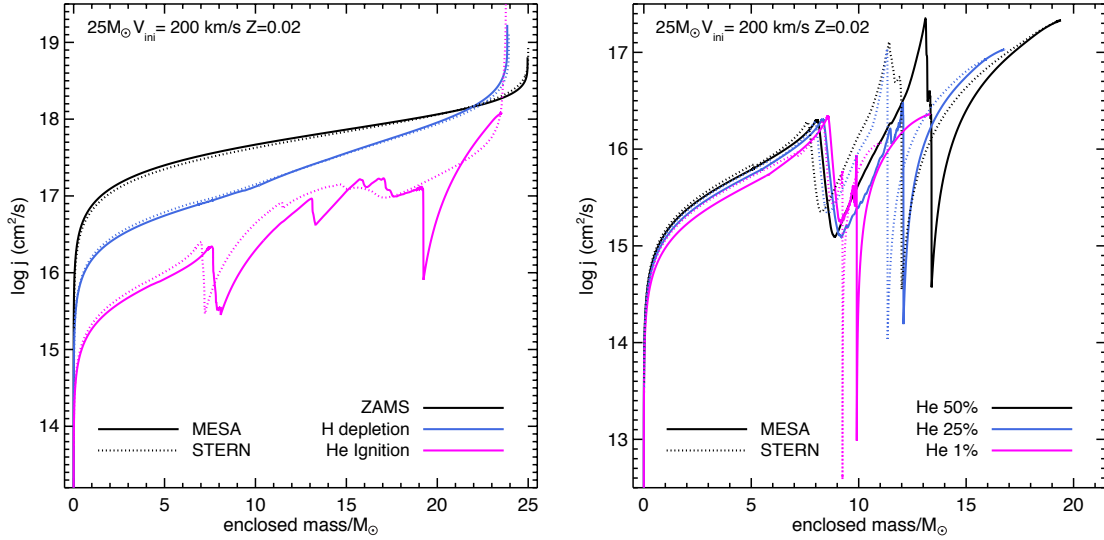


Figure 33. Evolution of internal specific angular momentum for the 25MAG model. Solid lines show MESA star result, while dashed lines refer to STERN. Left panel shows the evolution from zero age main sequence to He ignition. Right panel shows the evolution during core He-burning (from 50% of He in the core to He depletion). Notice the different axis range in the two plots.

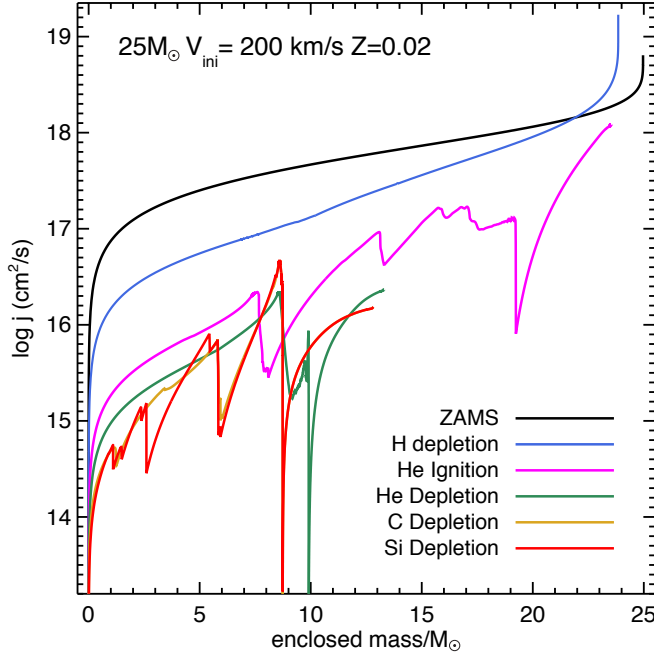


Figure 34. Evolution to Si-depletion of the internal specific angular momentum for the 25MAG model.

$P_{\text{gas}}(\rho, P_{\text{rad}})$ gives

$$\frac{dP_{\text{gas}}}{dr} = \left(\frac{\partial P_{\text{gas}}}{\partial \rho} \right)_{P_{\text{rad}}} \frac{d\rho}{dr} + \left(\frac{\partial P_{\text{gas}}}{\partial P_{\text{rad}}} \right)_{\rho} \frac{dP_{\text{rad}}}{dr}. \quad (24)$$

Solving eq. (24) for $d\rho/dr$ and using eq. (23) eliminates dP_{gas}/dr . Gas equations of state have $(\partial P_{\text{gas}}/\partial \rho)_T > 0$, so that for $d\rho/dr > 0$ (a density inversion), one must have

$$\left(\frac{dP_{\text{rad}}}{dr} \right) \left[\frac{L_{\text{Edd}}}{L_{\text{rad}}} - 1 - \left(\frac{\partial P_{\text{gas}}}{\partial P_{\text{rad}}} \right)_{\rho} \right] > 0.$$

Recognizing that $dP_{\text{rad}}/dr < 0$, we find that a density inversion

occurs when

$$\frac{L_{\text{rad}}}{L_{\text{Edd}}} > \frac{L_{\text{inv}}}{L_{\text{Edd}}} \equiv \left[1 + \left(\frac{\partial P_{\text{gas}}}{\partial P_{\text{rad}}} \right)_{\rho} \right]^{-1}. \quad (25)$$

This equation is identical to eq. (8) of Joss et al. (1973). Since under conditions of interest $(\partial P_{\text{gas}}/\partial P_{\text{rad}})_{\rho} > 0$, we have $L_{\text{inv}} < L_{\text{Edd}}$. For $L_{\text{inv}} < L_{\text{rad}} < L_{\text{Edd}}$, a density inversion will occur even though $dP_{\text{gas}}/dr < 0$.

Next, we shall consider the luminosity L_{onset} at which convection occurs. In a convective region, the entropy is either constant or declining with radius. Hence, convection will occur once

$$\frac{d \ln P_{\text{rad}}}{d \ln P} > \left(\frac{\partial \ln P_{\text{rad}}}{\partial \ln P} \right)_s; \quad (26)$$

using equation (22) and solving for the luminosity, we find that convection starts once

$$\frac{L_{\text{rad}}}{L_{\text{Edd}}} > \frac{L_{\text{onset}}}{L_{\text{Edd}}} \equiv \left(1 - \frac{P_{\text{gas}}}{P} \right) \left(\frac{\partial \ln P_{\text{rad}}}{\partial \ln P} \right)_s. \quad (27)$$

Equation (27) corresponds to eq. (9) of Joss et al. (1973). As argued in that paper, entropy decreases as density increases; therefore a density inversion implies a superadiabatic gradient, and as a result, $L_{\text{onset}} < L_{\text{inv}}$. This can be shown explicitly for a chemically homogenous mixture of an ideal gas and radiation. For such a mixture, equation (25) becomes

$$\frac{L_{\text{rad}}}{L_{\text{Edd}}} > \frac{L_{\text{inv}}}{L_{\text{Edd}}} = \left[\frac{1 - P_{\text{gas}}/P}{1 - 3P_{\text{gas}}/4P} \right], \quad (28)$$

and equation (27) becomes

$$\frac{L_{\text{rad}}}{L_{\text{Edd}}} > \frac{L_{\text{onset}}}{L_{\text{Edd}}} = \frac{8(1 - P_{\text{gas}}/P)(4 - 3P_{\text{gas}}/P)}{32 - 24P_{\text{gas}}/P + 3(P_{\text{gas}}/P)^2}, \quad (29)$$

allowing one to show that $L_{\text{onset}} < L_{\text{inv}}$. At high luminosities where the gas becomes radiation-dominated, however, the difference between L_{onset} and L_{inv} becomes small. Expanding equations (28) and (29) for $P_{\text{gas}}/P \ll 1$ gives $L_{\text{inv}} - L_{\text{onset}} \approx (3/4) \times (P_{\text{gas}}/P) \times L_{\text{Edd}}$. For such high-luminosity,

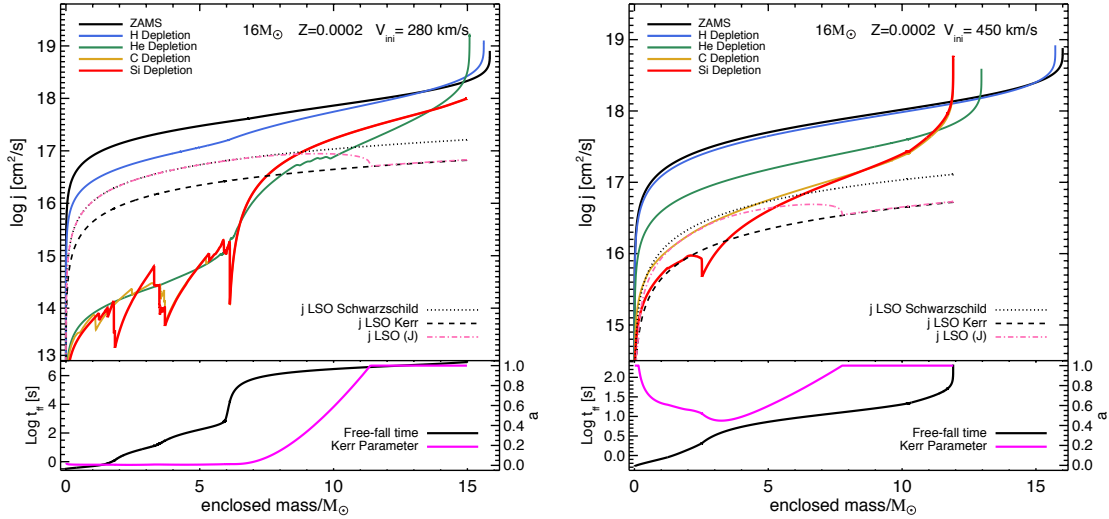


Figure 35. Specific angular momentum distribution for the two $16 M_{\odot}$ models. In the top panels, the solid curves show the distribution of specific angular momentum at different evolutionary stages. The other curves in the top panel show the specific angular momentum of the last stable orbit around a Schwarzschild black hole, a maximally rotating Kerr black hole ($a = 1$), and a black hole with a Kerr parameter corresponding to the angular momentum content of the stellar progenitor at that mass coordinate. The bottom panels show the free-fall time at the relative mass coordinate at the end of Si-burning. Notice the different ranges of the y-axis. These models can be compared to the calculations of Woosley & Heger (2006), in particular their models 16SG and 16TI respectively.

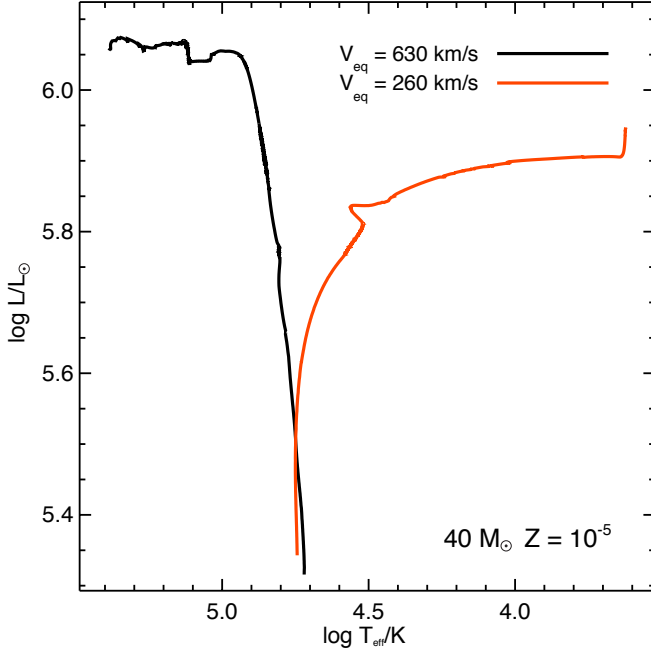


Figure 36. Evolution in the HR diagram for two rotating $40 M_{\odot}$ models at $Z = 10^{-5}$. The slower rotating model evolves toward the red part of the HRD; the other model evolves toward the blue part of the HRD. The internal evolution of the angular momentum is shown in Fig. 37. This can be compared to Fig. 2 of Yoon & Langer (2005).

radiation-dominated stars, a small inefficiency in convection is sufficient to drive a density inversion.

We now demonstrate that such inefficient convection can arise in the convective, radiation-dominated, envelopes of massive stars. In order of magnitude the convective and radiative fluxes are, respectively, $F_{\text{conv}} \sim \rho c_s^3 (\nabla_T - \nabla_{\text{ad}})^{3/2}$ and $F_{\text{rad}} \sim c P_{\text{rad}} / \tau$. To carry the flux, we need $F_{\text{conv}} \sim F_{\text{rad}}$; equating and substituting $\rho c_s^2 \sim P \sim P_{\text{gas}}$, we arrive at an expression that sets the level of superadiabaticity,

$$(\nabla_T - \nabla_{\text{ad}})^{3/2} \sim \frac{c}{c_s} \frac{P_{\text{rad}}}{P_{\text{gas}}} \tau^{-1}. \quad (30)$$

Under typical conditions in massive star envelopes, $c/c_s \sim 10^4$ at the iron opacity bump, but at this location, τ is not large enough to prevent the superadiabaticity from triggering a density inversion.

The lines in Fig. 39 show these luminosity conditions as a function of P_{gas}/P , and reveal that as the stellar conditions become radiation dominated, there is only a small gap between a convective model that is adiabatically stratified and a model with a density inversion. This corresponds to the region between the curves $L_{\text{rad}} = L_{\text{onset}}$ (dot-dashed line) and $L_{\text{rad}} = L_{\text{inv}}$ (dashed line). The gas pressure does not invert until $L > L_{\text{Edd}}$, which in Fig. 39 is the region above the solid horizontal line. We show profiles from a $30 M_{\odot}$ (left panel) and a $70 M_{\odot}$ model (right panel). These are from the first crossing of the Hertzsprung gap when $T_{\text{eff}} = 5000$ K. Each dot corresponds to a zone in the calculation; as the profile moves outward from center to surface the traces go from bottom to top in the plot. The blue dots indicate zones where the star is radiative; red indicates convection; a black border denotes a density inversion, $d\rho/dr > 0$; and yellow indicates a gas pressure inversion, $dP_{\text{gas}}/dr > 0$. There is excellent agreement between the detailed MESA evolutionary calculations and the analytical conditions (eq. [28] and [29]). The $70 M_{\odot}$ profile goes into the low P_{gas}/P , high $L_{\text{rad}}/L_{\text{Edd}}$ regime.

Figure 40 displays the physical conditions in the $70 M_{\odot}$ model where the density and gas pressure inversions develop. The panels display, from top to bottom, density, gas pressure, total pressure, and entropy, all as functions of radius. The total radius is $R = 1330 R_{\odot}$. Regions with $\nabla > \nabla_{\text{ad}}$ and $L_{\text{rad}} < L_{\text{inv}} < L_{\text{Edd}}$ are marked with a small red dot. Regions where $L_{\text{inv}} < L_{\text{rad}} < L_{\text{Edd}}$ (cf. eq. [28]) are marked with a large red dot with a black border. Regions where $L_{\text{rad}} > L_{\text{Edd}}$ are marked with a large yellow dot with black border. Although the pressure (panel c) is well-behaved in this superadiabatic (panel d) region, a density inversion does develop where $L_{\text{rad}} > L_{\text{rad}} > L_{\text{inv}}$ (panel a) and a gas pressure inversion develops (panel b) where $L_{\text{rad}} > L_{\text{Edd}}$, as predicted. In this region the superadiabaticity $\nabla_T - \nabla_{\text{ad}} > 10^{-2}$ and is greater than unity for $r/R_{\odot} \gtrsim 1300$. This is much larger than a typical value ($\sim 10^{-6}$) where convection is efficient and results in the

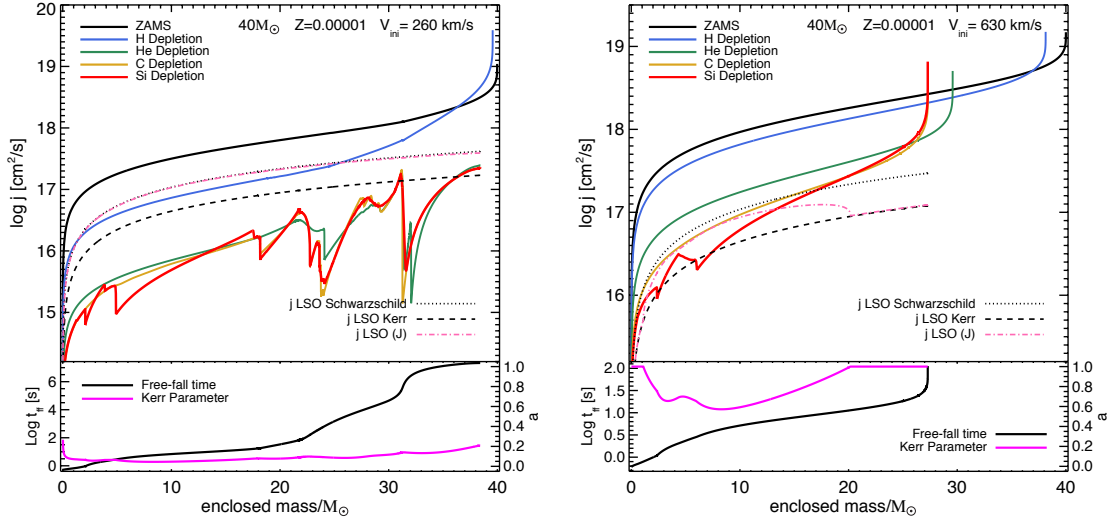


Figure 37. Specific angular momentum distribution for two $40 M_{\odot}$ models at $Z = 10^{-5}$ with $v_{\text{eq}} = 260 \text{ km s}^{-1}$ (top panel) and 630 km s^{-1} (bottom panel). Lines are showing the distribution of specific angular momentum at different stages of the evolution, together with the specific angular momentum of the last stable orbit around a Schwarzschild black hole, a maximally rotating Kerr black hole ($a = 1$) and a black hole with a Kerr parameter corresponding to the angular momentum content of the stellar progenitor at that mass coordinate. Note the different ranges of the y-axis. The evolutionary tracks for these models are shown in Fig. 36. These calculations should be compared to Fig. 5 of Yoon & Langer (2005).

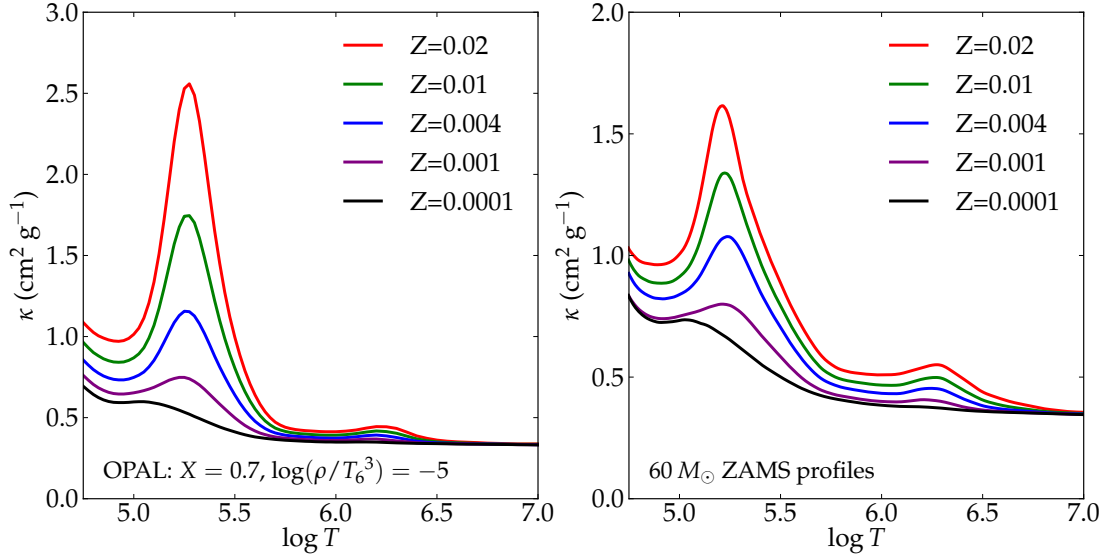


Figure 38. *Left:* A plot of the OPAL opacity data for five Z values at $X = 0.7$ and $\log(\rho/T_6^3) = -5$. These curves show the increase in the iron opacity bumps at $\log T \approx 5.3$ and 6.3 as Z increases from 10^{-4} to 0.02 . *Right:* The opacity-temperature profiles of $60 M_{\odot}$ ZAMS models for the same Z values.

entropy decreasing with r as shown in panel c.

7.2. Treatment of Superadiabatic Convection in Radiation-Dominated Regions

In MESA star the superadiabatic gradient arising in radiation-dominated envelopes can force the adoption of prohibitively short timesteps. Energy is mostly transported by radiation, and the convective velocities resulting from MLT approach the sound speed. The stability of such radiation-dominated envelopes has been questioned in the past, and is still a matter of debate (see, e.g., Langer 1997; Bisnovatyi-Kogan & Dorodnitsyn 1999; Maeder 2009). Hydrodynamical instabilities and the transport of energy from waves excited by near-sonic turbulent convection are important for energy transport, and three-dimensional hydrodynamical calculations are required to capture fully the complex physics occurring in this regime.

Here we develop a treatment that allows MESA star to calculate models of massive stars up to core collapse. For every model, MESA star computes the values of

$$\lambda_{\text{max}} \equiv \max\left(\frac{L_{\text{rad}}}{L_{\text{Edd}}}\right) \quad \text{and} \quad \beta_{\text{min}} \equiv \min\left(\frac{P}{P_{\text{gas}}}\right). \quad (31)$$

When β_{min} is small and λ_{max} is large, and MLT yields a $\delta_{\nabla} > \delta_{\nabla, \text{thresh}}$, we artificially decrease the superadiabaticity, $\delta_{\nabla} \equiv \nabla_T - \nabla_{\text{ad}}$, implied by MLT. The default of the user-specified parameter $\delta_{\nabla, \text{thresh}}$ is sufficiently large, $\sim 10^{-3}$, much larger than the typical values for efficient convection.

MESA star sets ∇_T to reduce the $\delta_{\nabla} - \delta_{\nabla, \text{thresh}}$ by a factor $\alpha_{\nabla} f_{\nabla}$, where f_{∇} is specified by the user, and α_{∇} is updated at each timestep to a linear combination of its previous value and a value $\tilde{\alpha}_{\nabla}(\lambda_{\text{max}}, \beta_{\text{min}})$. For large values of λ_{max} and small values of β_{min} , $\tilde{\alpha}_{\nabla} \rightarrow 1$; in typical usage, the transition happens

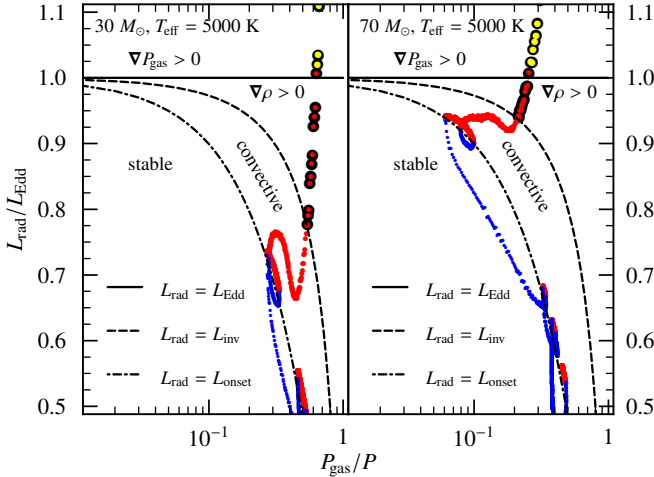


Figure 39. The critical luminosities $L_{\text{rad}} = L_{\text{onset}}$ (eq. [29], dot-dashed line), $L_{\text{rad}} = L_{\text{inv}}$ (eq. [28], dashed line), and $L_{\text{rad}} = L_{\text{Edd}}$ (solid line) as a function of P_{gas}/P for an ideal gas-radiation mixture. Compare this with Fig. 1 of Joss et al. (1973). For $L_{\text{rad}} < L_{\text{onset}}$, the gas is convectively stable; for $L_{\text{onset}} < L_{\text{rad}} < L_{\text{inv}}$, the gas is convective; for $L_{\text{inv}} < L_{\text{rad}} < L_{\text{Edd}}$, the density is inverted, $d\rho/dr > 0$; and for $L_{\text{Edd}} < L_{\text{rad}}$, the gas pressure is inverted, $dP_{\text{gas}}/dr > 0$. Overlaid on the plots are the profiles from a $30 M_{\odot}$ (left panel) and a $70 M_{\odot}$ (right panel) model with $Z = 0.02$: blue dots indicate zones that are radiative; red dots indicate $\nabla_{\text{rad}} > \nabla_{\text{ad}}$; dots with a black border have a density inversion; and the yellow dots with black borders indicate a gas pressure inversion. As the profile moves out from the stellar center it traces out the points on the plot from bottom to top. Only a part of the model profiles are visible in the plot. The calculations correspond to the first crossing of the Hertzsprung gap when $T_{\text{eff}} = 5000$ K.

where $\lambda_{\text{max}} \approx 0.5$ and $\beta_{\text{min}} \approx 0.3$. For small values of λ_{max} and large values of β_{min} , $\alpha_{\nabla} \rightarrow 0$. Thus f_{∇} sets the maximum reduction of $\delta_{\nabla} - \delta_{\nabla, \text{thresh}}$. Figure 41 shows how MESA star turns on the reduction in δ_{∇} as a star evolves. Tracks in the HR diagram are shown for four stellar models: 15, 25, 30, and $70 M_{\odot}$. The color of each line indicates the value of α_{∇} at each point.

Such a decrease of the temperature gradient reduces L_{rad} and implies additional physical transport. Potential agents for the excess transport include waves excited by turbulent convection (see, e.g., Maeder 1987a) and radiative diffusion enhanced by porous clumping of the envelope (e.g., Owocki et al. 2004). As these radiation-dominated envelopes might be physically unstable, with a resulting strong enhancement of mass loss, we caution that the results of any 1D stellar evolution calculation for the late evolutionary phases of massive stars should be considered highly uncertain.

We now show a comparison of MESA star calculations of rotating massive stars done with and without MLT++. We used the $25 M_{\odot}$ model described in §6.4, which at $Z = 0.02$ is around the upper mass limit that can converge using a reasonably short timestep without having to rely on the MLT++. The most prominent difference between the calculations is the evolutionary track in the HR-diagram (Fig. 42). This is not surprising, as MLT and MLT++ result in different efficiencies of energy transport in radiation-dominated stellar envelopes. The sharp drop in L for the MLT++ case is the result of a brief period of enhanced mass loss due to super-critical rotation. The structure and the angular momentum content of the collapsing core are weakly dependent, however, on the choice of MLT vs. MLT++ (Fig. 43).

7.3. Core-Collapse Progenitor Models

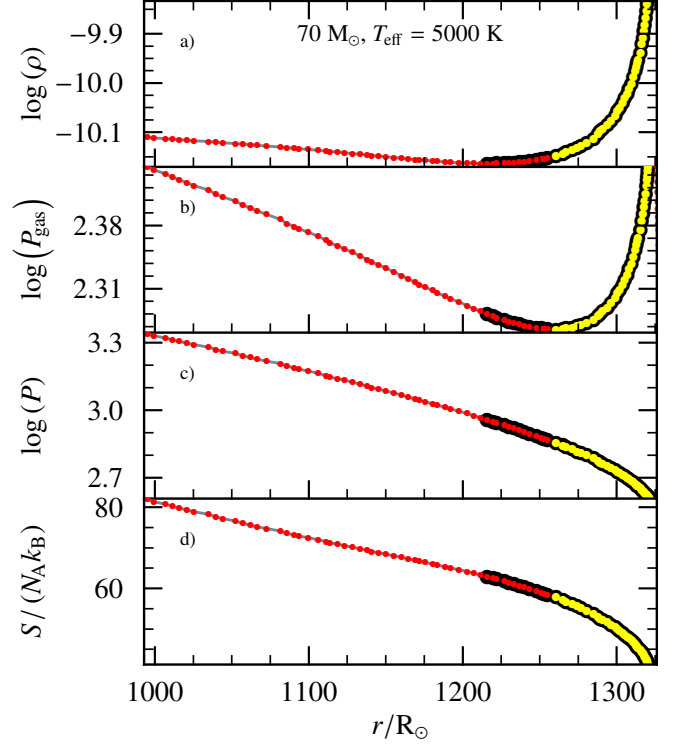


Figure 40. The panels display, from top to bottom, the density, gas pressure, total pressure, and entropy as functions of radius for the $70 M_{\odot}$ model shown in Fig. 39. The range of radii is restricted to the region where density and gas pressure inversions develop. Each zone is marked by a dot; a small red dot indicates convection with no predicted gas or gas pressure inversion ($L_{\text{rad}} < L_{\text{inv}}$); a large red dot with black border indicates a predicted density inversion but no gas pressure inversion ($L_{\text{inv}} < L_{\text{rad}} < L_{\text{Edd}}$); and a yellow dot with black border indicates a convective region with a predicted gas pressure inversion ($L_{\text{rad}} > L_{\text{Edd}}$). The total pressure (panel c) is well-behaved at all radii. Note also the decrease in entropy (panel d): the region is superadiabatic.

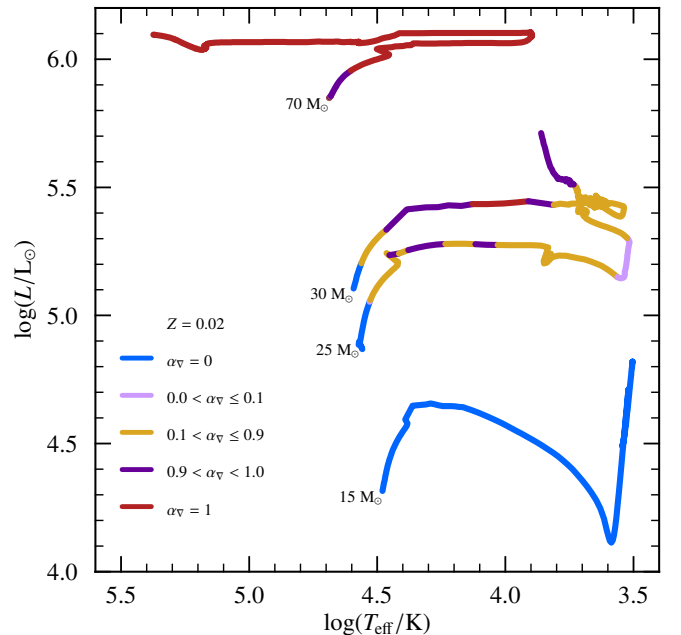


Figure 41. HR diagram of 15, 25, 30, and $70 M_{\odot}$ models. The color indicates the value of α_{∇} at that point in the star's evolution. For the $25 M_{\odot}$ and $30 M_{\odot}$ stars, there is a sharp spike in α_{∇} as the star crosses the Hertzsprung gap followed by a sharp drop at the base of the red giant branch. The $70 M_{\odot}$ model has $\alpha_{\nabla} > 0.9$ for its entire evolution.

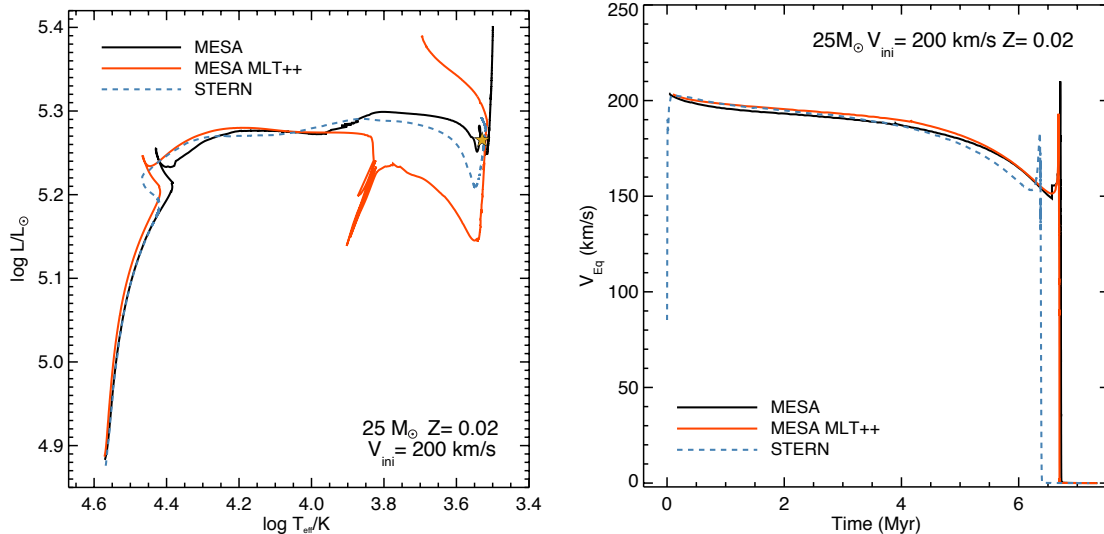


Figure 42. Comparison of evolutionary tracks (left) and equatorial rotational velocity (right) for a $25 M_{\odot}$ model with $Z = 0.02$ and $v_{\text{eq}} = 200 \text{ km s}^{-1}$. The solid black lines show MESA star results with MLT (black) and MLT++ (orange), while the dashed blue line refers to STERN calculations. The star symbol shows the location where we started the calculation for the RSG pulsations discussed in §7.4.

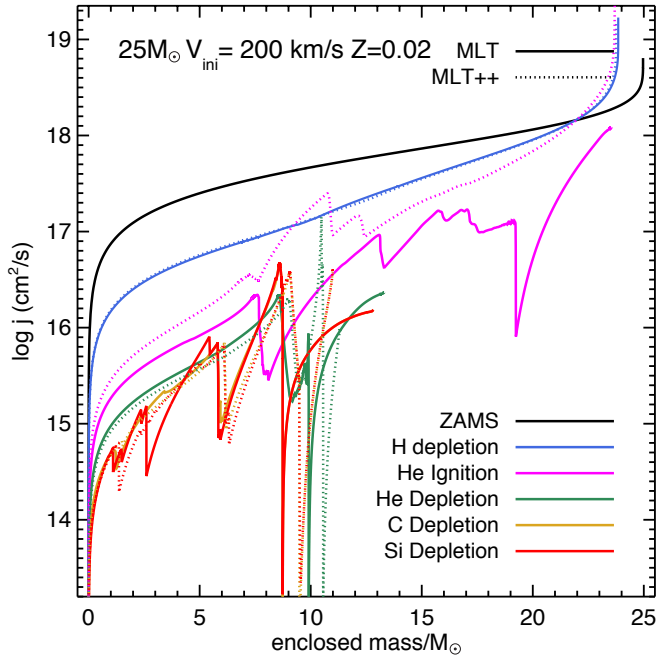


Figure 43. Evolution of internal specific angular momentum for the two $25 M_{\odot}$ models of Fig. 42. The dashed lines show models calculated with MLT++. Due to different excursions in the HRD (see Fig. 28) calculations with MLT and MLT++ end with different final masses. There are no substantial changes, however, in the specific angular momentum content of the stellar cores.

We evolve a grid of massive stars initially rotating with $\Omega/\Omega_{\text{crit}} = 0.2$. The models have been initialized using solid body rotation. Models with initial $M/M_{\odot} = 30, 40, 50, 60, 70, 80, 90$ and 100 have initial $Z = 0.02$, while models with initial $M/M_{\odot} = 120, 150, 250, 500$ and 1000 have been initialized with $Z = 0.001$. To calculate convective boundaries we adopt the Ledoux criterion including the impact of semi-convection (with $\alpha_{\text{sc}} = 0.02$, see §4.1). The transport of angular momentum and chemicals by rotational instabilities and magnetic torques is included and calibrated following Heger et al. (2000, 2005) and Yoon & Langer (2005). Wind mass-loss is implemented following the recipe of Glebbeek

et al. (2009). For $T_{\text{eff}} > 10^4 \text{ K}$ and H-surface fraction > 0.4 , the mass-loss prescription of Vink et al. (2001) is used. In the same temperature range, but when the H-surface fraction decreases below 0.4, Nugis & Lamers (2000) determine the mass-loss rate. At low temperatures ($T_{\text{eff}} < 10^4 \text{ K}$) the mass-loss rate of de Jager et al. (1988) is used.

Figure 44 shows the central conditions of these massive rotating models. For each model the calculation stops when any part of the collapsing core reaches an infall velocity of 1000 km s^{-1} . Some of the initial and final properties are summarized in Table 5. These calculations are performed to reveal the new capabilities of MESA star. The values of the parameters for these calculations have not been calibrated against existing calculations or observations.

7.4. Radial Instability of Red Supergiants

Massive red supergiants (RSG) are unstable to radial pulsations driven by the κ -mechanism in the hydrogen ionization zone. Both linear and non-linear calculations show the occurrence of oscillations with the period and growth rate of the dominant fundamental mode increasing with L/M (Li & Gong 1994; Heger et al. 1997; Yoon & Cantiello 2010). The periods are of the order of years. As discussed by Yoon & Cantiello (2010) the occurrence of RSG pulsations can impact stellar mass-loss rates and modify the evolution of massive stars above a certain mass. We study the occurrence of RSG pulsations with MESA star and compare results with existing non-linear calculations.

In Fig. 45 we show the capability of MESA star to exhibit radial oscillations in luminous RSGs. We use the same $25 M_{\odot}$ rotating model discussed in § 6.4, and we restart the calculation when the He mass fraction in the core is $Y_c = 0.7$. For non-rotating RSG with $Z = 0.02$, Yoon & Cantiello (2010) found pulsation periods in the range 1–8 yr. To resolve the RSG pulsations we force the timestep to $< 0.01 \text{ yr}$, much shorter than the usual timestep during He-burning ($\delta t \gtrsim 10^2 \text{ yr}$, see Appendix B.3). This explains why RSG pulsations are usually not found during the evolution of massive stars. Before the code stops due to the emergence of supersonic radial velocities in the envelope, we find a pulsational period $\approx 4 \text{ yr}$, in good agreement with the results of Yoon &

Table 5
Initial (ZAMS) and final (core-collapse) properties.

M_{ini} [M_{\odot}]	Z_{ini}	$\Omega/\Omega_{\text{crit}}^{\text{a}}$	$v_{\text{eq,ini}}^{\text{b}}$ [km s^{-1}]	$J_{\text{ini}}^{\text{c}}$ [ergs s]	Δt^{d} [Myr]	$\Delta t_{\text{H}}^{\text{e}}$ [Myr]	$\Delta t_{\text{He}}^{\text{e}}$ [Myr]	M_{f}^{f} [M_{\odot}]	M_{Fe}^{g} [M_{\odot}]	J_{f}^{h} [ergs s]	J_{Fe}^{i} [ergs s]
30	0.020	0.20	129.69	3.28×10^{52}	6.30	5.87	0.36	17.77	1.41	2.87×10^{50}	1.03×10^{48}
40	0.020	0.20	122.86	4.87×10^{52}	5.06	4.71	0.31	19.37	1.81	3.77×10^{50}	1.61×10^{48}
50	0.020	0.20	112.02	6.30×10^{52}	4.41	4.08	0.29	25.04	1.38	5.39×10^{50}	1.09×10^{48}
60	0.020	0.20	98.37	7.34×10^{52}	4.04	3.66	0.35	22.88	1.76	7.81×10^{50}	2.76×10^{48}
70	0.020	0.20	78.76	7.53×10^{52}	3.90	3.57	0.29	26.19	1.75	5.30×10^{50}	1.54×10^{48}
80	0.020	0.20	50.10	5.88×10^{52}	3.70	3.38	0.29	29.20	1.78	6.16×10^{50}	1.44×10^{48}
90	0.020	0.20	2.27	3.57×10^{52}	3.10	2.80	0.27	44.90	1.71	4.39×10^{50}	5.23×10^{47}
100	0.020	0.20	2.34	3.91×10^{51}	2.98	2.69	0.26	49.02	1.92	5.50×10^{50}	6.58×10^{47}
120	0.001	0.20	145.41	2.93×10^{53}	3.26	2.99	0.23	79.38	–	4.79×10^{51}	–
150	0.001	0.20	134.75	3.84×10^{53}	3.03	2.77	0.23	95.52	–	6.80×10^{51}	–
250	0.001	0.20	69.30	4.39×10^{53}	2.56	2.32	0.21	167.49	–	9.13×10^{51}	–
500	0.001	0.20	3.78	6.40×10^{52}	2.19	1.96	0.20	410.28	–	7.92×10^{51}	–
1000	0.001	0.20	4.42	2.09×10^{53}	1.99	1.77	0.19	860.48	–	2.44×10^{52}	–

^a Initial rotation rate, see definition in §. 6.3.

^b Initial equatorial rotational velocity.

^c Total initial angular momentum.

^d Stellar lifetime.

^e Main sequence and core He-burning lifetimes. These are defined as the interval between onset of core burning and depletion of central hydrogen (or helium) to 1% by mass.

^f Final mass.

^g Mass of the Iron core (if present).

^h Final total angular momentum.

ⁱ Final total angular momentum of the iron-core.

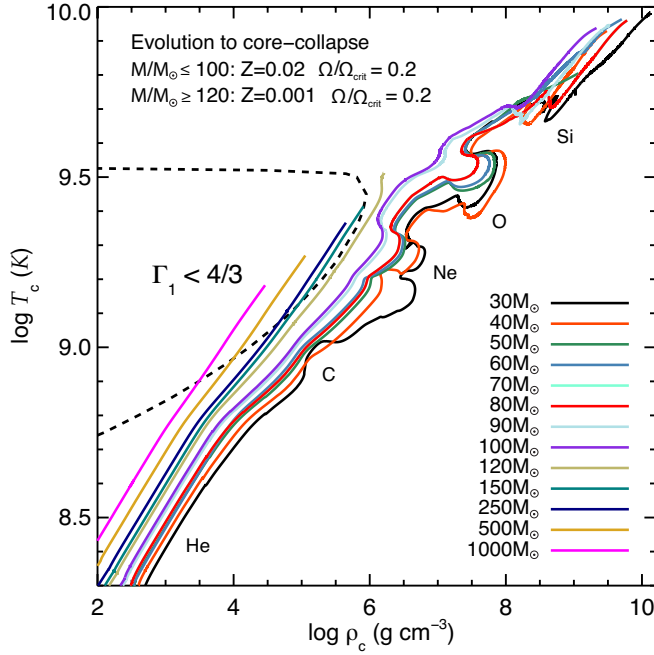


Figure 44. Evolution of T_c and ρ_c in the massive rotating models. The locations of core helium, carbon, neon, oxygen, and silicon burning are labeled. A dashed curve marks the electron-positron pair-instability region where $\Gamma_1 < 4/3$. All models are rotating initially at 20% of critical rotation. The calculations include the effects of rotation and Spruit-Tayler magnetic fields as discussed in §6. Models with initial mass $\leq 100 M_{\odot}$ have initial metallicity $Z = 0.02$, while models with mass $\geq 120 M_{\odot}$ have initial metallicity $Z = 0.001$. The end of the line for each mass corresponds to the time of core-collapse, defined as when any part of the collapsing-core exceeds an in-fall velocity of 1000 km s^{-1} . The tracks for the $80 M_{\odot}$ and $90 M_{\odot}$ overlap in this plot.

Cantiello (2010).

8. SUMMARY AND CONCLUSIONS

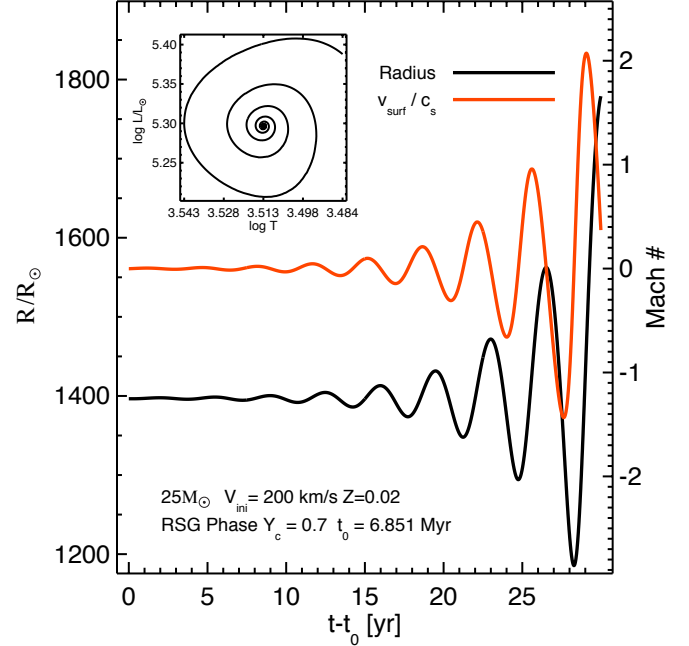


Figure 45. Surface properties of a pulsating RSG. This is the same $25 M_{\odot}$ model discussed in Sec. 6.4, evolved from $t_0 = 6.851 \text{ Myr}$ (corresponding to $Y_c = 0.7$, star symbol in Fig. 32) with timesteps $\delta t \leq 0.01 \text{ yr}$. The black line shows the evolution of the stellar radius, while the orange line shows the value of the surface radial velocity (in units of the local sound speed). The inset shows the corresponding evolution in the HR-diagram.

We have explained and, where possible, verified the improvements and major new capabilities implemented in MESA since the publication of Paper I. These advancements include evolutionary modeling for giant planets (§2), tools for asteroseismology (§3), implementation of composition gradients in stellar interiors and their impact on convective mixing (§4), the evolution of intermediate mass stars and white dwarfs

(§5) the treatment of rotation during stellar evolution (§6), addressing the onset of radiation pressure dominance in the envelopes of evolving massive stars due to the iron opacity bump, and evolving massive stars to the onset of core collapse (§7). The enhancements include the physics modules (Appendix A), the algorithms (Appendix B), and the addition of a MESA Software Development Kit (Appendix C). MESA star input files and related materials for all the figures are available at <http://mesastar.org>.

These hitherto unpublished advancements have already enabled a number of studies in planets (e.g., Passy et al. 2012; Huang & Cumming 2012; Carlberg et al. 2012), classical novae (Denissenkov et al. 2013), asteroseismology (e.g., Yang et al. 2012; Burkart et al. 2012b; Moravveji et al. 2012), rotationally induced mixing (e.g., Denissenkov 2010; Chatzopoulos et al. 2012; Chatzopoulos & Wheeler 2012) and enabled the discovery of new features in the evolution of low-mass stars (Denissenkov 2012). In addition, these enhanced capabilities have allowed for applications of MESA star that were not initially envisioned, such as explorations of stars under modified gravity (Chang & Hui 2011; Davis et al. 2012), and stellar oscillations induced by tidal disturbances in double white dwarf binaries (Fuller & Lai 2012a,b; Burkart et al. 2012a).

As an open source “instrument” for stellar astrophysics, it is difficult to predict all the ways in which future development of MESA will occur. We do know, however, that future versions of MESA will include advances in physics modules, features driven by the MESA user community, and architectural refinements. For example, the plethora of asteroseismological data is driving new initiatives to incorporate non-adiabatic pulsation codes, where possible, into MESA. The prevalence of interacting binary star systems, especially for massive stars, has increased the pressure for MESA development efforts that would yield the capability to simultaneously evolve two interacting stellar models. Physics module developments will likely include general relativistic corrections to the stellar structure equations (e.g., difference between gravitational and baryonic mass), the mass diffusion coefficients in electron degenerate environments, phase separation in cooling white dwarfs, and nuclear statistical equilibrium solvers. We also expect the transition from multicore systems (with order 10 cores) to many-core architectures (with order 100 cores) to drive new directions in MESA’s algorithmic and architectural development.

It is a pleasure to thank Falk Herwig for significant contributions to the MESA project and Jørgen Christensen-Dalsgaard for kindly providing the ADIPLS code for inclusion in MESA and assisting with its integration. We likewise thank Jared Brooks for documenting the MESA test suite, Tristan Guillot for providing the CEPAM evolutionary tracks, Alexander

Potekhin for an update to his EOS code, Didier Saumon and Jim MacDonald for providing EOS tables, René Rohrman for providing atmosphere tables, Richard Freedman for providing opacity tables, Evert Glebbeek, Alex Heger, and Norbert Langer for providing code for implementing rotation, and Haili Hu for providing code for implementing diffusion.

We also thank David Arnett, Tim Bedding, Kent Budge, Phil Chang, Pieter DeGroot, Pavel Denisenkov, Jonathan Fortney, Chris Fryer, Gustavo Hime, Raphael Hirschi, Sam Jones, Steve Kawaler, Phillip Macias, Pablo Marchant, Travis Metcalfe, Kevin Moore, Ehsan Moravveji, Jean-Claude Passy, Hideyuki Saio, Josiah Schwab, Aldo Serenelli, Josh Shiode, Steinn Sigurdsson, Anne Thoul, Roni Waldman, Achim Weiss, Stan Woosley, Sung-Chul Yoon, and Patrick Young for providing valuable discussions and correspondence. Some of the simulations for this work were made possible by the Triton Resource, a high performance research computing system operated by San Diego Supercomputer Center at UC San Diego.

We thank the participants of the 2012 MESA Summer School for their willingness to experiment with the new capabilities: Jeff Andrews, Umberto Battino, Keaton Bell, Harshal Bhadkamkar, Kristen Boydston, Emmanouil Chatzopoulos, Eugene Chen, Jieun Choi, Alex Deibel, Luc Dessart, Ian Dobbs-Dixon, Tassos Fragos, Samuel Harold, Daniel Huber, Joe Hughto, Max Katz, Agnes Kim, Io Kleiser, Shri Kulkarni, Gongjie Li, Christopher Lindner, Jing Luan, Mia Lundkvist, Morgan MacLeod, João Marques, Grant Newsham, Rachel Olson, Richard O’Shaughnessy, Kuo-Chuan Pan, Ilka Petermann, Theodore Sande, Ken Shen, Natalia Shabalta, Dave Spiegel, Jie Su, Tuguldur Sukhbold, David Tsang, Bill Wolf, Angie Wolfgang, Tsing Wai Wong, and Alexey Zinger.

This project was broadly supported by the NSF under grants PHY 11-25915 and AST 11-09174. M.C. acknowledges partial support from the “Alberto Barlettani” Prize 2012. P.A. acknowledges support by NSF AST-0908873 and NASA NNX09AF98G. L.B. acknowledges support from the Wayne Rosing, Simon and Diana Raab Chair in Theoretical Astrophysics at KITP. E.F.B. acknowledges support by the Joint Institute for Nuclear Astrophysics under NSF PHY grant 08-22648. A.L.D. received support from the Australian Research Council under grant FL110100012. M.H.M. acknowledges support by the NSF grant AST-0909107, the Norman Hackerman Advanced Research Program under grant 003658-0252-2009, and the Delaware Asteroseismic Research Center. D.S. acknowledges support by the Australian Research Council. F.X.T. acknowledges support from the NSF under grants AST 08-06720, AST 6736821, AST 09-07919, AST 10-07977, PHY 08-22648, and from NASA under grants 08-NAI5-0018 and NNX11AD31G. R.T. acknowledges support by NSF grants AST-0908688 and AST-0904607, and NASA grant NNX12AC72G.

APPENDIX

UPDATES TO INPUT PHYSICS MODULES

There have been many updates and improvements to the physics modules since Paper I. In this appendix, we describe the changes that have been made to the microphysics modules `chem` (§ A.1), `eos` (§ A.2), `kap` (§ A.3), and `net` (§ A.4). We conclude by listing updates to the atmosphere boundary conditions (§ A.5).

Atomic and Nuclear Data

The `chem` module now has the latest version (v2.0) of the JINA `reacLib` nuclide data (Cyburt et al. 2010). This contains updated mass evaluations, and now includes 7853 nuclides up to ³³⁷Cn. For precision work, the `chem` module now distinguishes

between the atomic mass number A_i —the number of nucleons in a given isotope—and the atomic mass W_i . The abundance of a species i is defined as

$$Y_i \equiv \frac{n_i}{n_B}, \quad (\text{A1})$$

where n_B is the baryonic number density. The *baryon fraction* X_i is then

$$X_i = Y_i A_i = \frac{n_i A_i}{n_B}, \quad (\text{A2})$$

Note that $\sum_i X_i = n_B/n_B = 1$ and is invariant under nuclear reactions. We then define the baryon density (in mass units) as

$$\rho = n_B m_u, \quad (\text{A3})$$

where $m_u = 1.660538782 \times 10^{-24}$ g is the atomic mass unit (CODATA 2006 value; Mohr et al. 2008). Note that the numerical value m_u , along with other physics constants, are defined in the `const` module. The atomic mass of isotope i is defined in MESA as

$$W_i = A_i + \frac{\Delta_i}{m_u c^2}, \quad (\text{A4})$$

where Δ_i/c^2 is the mass excess of isotope i . This treatment neglects the electronic binding energy, and Δ is therefore independent of the ionization state of a given species. The electron rest masses are, however, included in this definition, since the W_i are atomic masses.

The MESA microphysics modules—`kap`, `eos`, `neu`, and `net`—use ρ , T , and $\{X_i\}$ as inputs. MESA star multiplies ρ by a mass correction factor $\bar{W}/\bar{A} = \sum_i W_i Y_i / \sum_i A_i Y_i$ to distinguish between A_i and W_i before starting the calculation for a timestep. A call to the routine `composition.info` in the `chem` module returns the following averaged quantities: the mean atomic mass number, $\bar{A} \equiv \sum_i Y_i A_i / \sum_i Y_i$, mean atomic charge number, $\bar{Z} \equiv \sum_i Z_i Y_i / \sum_i Y_i$, mean square atomic charge number, $\sum_i Z_i^2 Y_i / \sum_i Y_i$, the electron abundance, $Y_e = \bar{Z}/\bar{A}$, and the mass correction term, \bar{W}/\bar{A} . In addition, the routine returns the derivatives of \bar{A} , \bar{Z} , and \bar{W}/\bar{A} with respect to the baryon fractions X_i :

$$\left. \frac{\partial \bar{A}}{\partial X_i} \right|_{\rho, X_{j \neq i}} = \frac{\bar{A}}{A_i} (A_i - \bar{A}) \frac{1}{\sum_i X_i}; \quad (\text{A5})$$

$$\left. \frac{\partial \bar{Z}}{\partial X_i} \right|_{\rho, X_{j \neq i}} = \frac{\bar{A}}{A_i} (Z_i - \bar{Z}) \frac{1}{\sum_i X_i}; \quad (\text{A6})$$

$$\left. \frac{\partial (\bar{W}/\bar{A})}{\partial X_i} \right|_{\rho, X_{j \neq i}} = \left(\frac{W_i}{A_i} - \frac{\bar{W}}{\bar{A}} \right) \frac{1}{\sum_i X_i}. \quad (\text{A7})$$

Note that the routine does not make any assumption in these derivatives that $\sum_i X_i \equiv \sum_i A_i Y_i = 1$; in this formulation, $\sum_i X_i$ is not explicitly set to unity.

At the beginning of each Newton iteration, the abundances are checked. A mass fraction is considered good if its value exceeds `min_xa_hard_limit`. If all mass fractions meet this standard, then the mass fractions are clipped to range from 0 to 1, and the mass fractions are summed. If the sum differs from unity by less than a value `sum_xa_tolerance`, then the mass fractions are renormalized to sum to unity; otherwise, the code reports an error. Currently composition derivatives are ignored in the `eos` and `kap` routines. Equations (A5)–(A7) allow, however, future additions to these routines to compute these derivatives analytically.

Equation of State

The only significant change to the `eos` module since Paper I is the addition of tables for $Z > 0.04$, where Z is the mass fraction of all elements heavier than He. The `eos` module as described in Paper I supplied equation of state (EOS) tables for $Z = 0.0$, 0.02 , and 0.04 at temperatures and densities for which neutral and partially-ionized species are present (see Paper I, Figure 1). For $Z > 0.04$ MESA switched to the HELM EOS (Timmes & Swesty 2000), which assumes full ionization. In order to rectify the inconsistent treatment of the partially-ionized region at high Z , new EOS tables have been computed (J. MacDonald, priv. comm.) using the MacDonald EOS code (MacDonald & Mullan 2012) for $Z = 0.2$ (scaled-solar), and two $Z = 1.0$ compositions: one with 49.5% C, 49.5% O, and 1% scaled-solar by mass; and one with 50% C and 50% O by mass. Here “scaled-solar” refers to the Grevesse & Noels (1993) solar heavy element distribution adopted in the OPAL EOS tables (Rogers & Nayfonov 2002).

Opacities

The `kap` module now divides the opacity tables into a high-temperature domain, $\log(T/\text{K}) \gtrsim 4$, and a low-temperature domain, $\log(T/\text{K}) \lesssim 4$; the exact range of $\log T$ over which the tables are blended can be adjusted at runtime. This treatment differs from the opacity tables described in Paper I, which combined high- and low-temperature opacities into a single set of tables. The motivation for separating the tables is to facilitate using different sources of low- T opacity data. The `kap` module now supports low- T opacities from either Ferguson et al. (2005) or Freedman et al. (2008) with updates to the molecular hydrogen pressure-induced opacity (Frommhold et al. 2010) and the ammonia opacity (Yurchenko et al. 2011). Either set may be selected at run time. The electron conduction opacity tables, based on Cassisi et al. (2007), have been expanded (Potekhin 2011, priv. comm.) to cover higher temperatures (up to 10^{10} K, originally 10^9 K) and densities (up to $10^{11.5}$ g cm $^{-3}$, originally $10^{9.75}$ g cm $^{-3}$).

Atmosphere Boundary Conditions

The `atm` module provides the surface boundary condition for the interior model. A collection of four new options that extend the set described in Paper I are now available.

1. `solar_hopf_grey`: Implements the solar-calibrated Hopf $T(\tau)$ relation, where

$$T^A(\tau) = \frac{3}{4} T_{\text{eff}}^4 [\tau + q(\tau)], \quad (\text{A8})$$

and

$$q(\tau) = q_1 + q_2 \exp(-q_3 \tau) + q_4 \exp(-q_5 \tau). \quad (\text{A9})$$

The q_i are fit to the solar atmosphere with resulting values $q_1 = 1.0361$, $q_2 = -0.3134$, $q_3 = 2.448$, $q_4 = -0.2959$, and $q_5 = 30.0$ (J. Christensen-Dalsgaard, 2011, priv. comm.).

2. `grey_and_kap`: Expands on the simple assumption that $P \simeq \tau g / \kappa$ by iterating to find a consistent solution among P , T , and $\kappa(\rho, T)$.
3. `grey_irradiated`: Implements the Guillot (2010) $T(\tau)$ relation that includes both external irradiation by the star and cooling flux from the interior; see Guillot (2010, eq. 49) along with the discussion and results in §2.4. In addition to the external and internal fluxes, this boundary condition requires two constant opacity values: κ_v for the external radiation, and κ_{th} for the thermal radiation generated within the atmosphere. This boundary condition is unique in that it is applied at a specified pressure level, as opposed to optical depth. This pressure must be chosen sufficiently high to capture any heating of the atmosphere by the irradiation.
4. `WD_tau_25_tables`: Provides as outer boundary conditions the values of P_{gas} and T at $\log(\tau) = 1.4$ as extracted from pure hydrogen model atmospheres of WDs (Rohrmann et al. 2012; Rohrmann 2001). The tables span a range of effective temperatures and surface gravities: $2,000 \text{ K} \leq T_{\text{eff}} \leq 40,000 \text{ K}$ and $5.5 \leq \log g \leq 9.5$. See § 5.2 for an example of the use of these tables.

NUTS AND BOLTS

We now briefly describe the primary components of evolution calculations. MESA star first reads the input files and initializes the physics modules to create a nuclear reaction network and access the EOS and opacity data. The specified starting model is then loaded into memory and the evolution loop is entered.

Evolve a Step

The top level routine for evolving a star for a single timestep is `do_evolve_step`. If this is the first attempt to do a step starting from the current state, the model is remeshed (see §B.4), and information for MLT++ is prepared by the routine `set_gradT_excess_alpha` (see §7.2). Sufficient information is saved so that if necessary it will be possible to make other attempts (i.e., after a redo, a retry, or a backup). In addition to the current state, we keep the previous state (called “old”), and the one that came before “old” (called “older”). During the step, the current state is modified, and the old one holds the state at the start of the step. If we do a redo or a retry, we copy old to current to restore the starting state. If we do a backup, we copy older to old before copying old to current, making us start at the state prior to the current one. Note that the duration of the timestep is determined before the call on `do_evolve_step` by the process described in §B.3.

After remeshing and the other initial preparations, `do_evolve_step` begins the operations that are done on every attempt. It first calls the routine `do_winds` which sets \dot{M} based on the current radius, luminosity, mass, metallicity, and other properties as needed. During the evaluation of `do_winds` there is a call on the user-defined `other_wind` routine giving users an easy way to define different schemes for setting \dot{M} .

Information for evaluating the Lagrangian time derivatives is stored by a call to `save_for_d_dt`. The ensuing call to `do_adjust_mass` adds or removes mass without changing the number of grid points (see §B.5). Information for evaluating the Lagrangian time derivatives is updated at this point. Variables for the model are evaluated to reflect the changes made by remeshing and changing mass. This includes evaluation of the Brunt-Väisälä frequency (see §3.3), and the diffusion coefficients for the mixing of composition (see §4.1 and 4.2). The user-defined routines `other_brunt`, `other_mlt`, and `other_mixing` are called as part of this. If rotation is enabled, there is a call to `set_rotation_mixing_info` (see §6) which in turn calls `other_am_mixing`. If element diffusion from gravitational settling and chemical diffusion is active, the routine `do_element_diffusion` adjusts the composition and includes a call on `other_diffusion`. The ensuing call to `do_struct_burn_mix` solves for the new structure and composition of the star through repeated Newton iterations (see §B.2). Non-convergence causes `do_evolve_step` to return with a result indicating a failure. Convergence is followed by a call to the routine `do_solve_omega_mix` which adjusts the total angular momentum by solving a diffusion equation (see §B.6); it calls `other_torque`. There is an option to repeat the operations described in this paragraph in case rotationally enhanced mass loss (see §6.3) has not been sufficient to eliminate super-critical surface velocities. In such a situation, the mass loss is adjusted iteratively until slightly sub-critical velocities result. In effect, this is an implicit solution for the appropriate \dot{M} when super-critical rotation occurs.

Next, if specified by the user, `smooth_convective_bdy` is called to smooth abundances behind retreating convection boundaries. Finally, a call to `do_report` gathers information and metrics about the timestep for the user. This information will then be available to the user’s `extras_check_model` routine.

Solving the Coupled Structure, Burn, and Mix Equations

A call to `do_struct_burn_mix` invokes a Newton method—an N -dimensional root find—to solve a system of N nonlinear differential-algebraic equations for the new structure and composition of the stellar model. Here N is the number of zones in the current model times the number of basic variables per zone and can exceed 100,000.

The equations to be solved are written as the relation $F(\text{basic_vars}) = 0$, where F is the vector-valued function of the residuals. If the `basic_vars` were a perfect solution to the equations, we would have $F = 0$; in practice, the solution is never perfect. The solution strategy is to iteratively adjust the values of the `basic_vars` to reduce F towards zero. An approximate solution is accepted depending on both the magnitude of F and the relative size of the adjustments to `basic_vars`. Adjustments are chosen using the Jacobian matrix of partial derivatives of all the F equations with respect to all the `basic_vars`.

Figure 47 figure shows the three blocks making up the row of the block tridiagonal Jacobian matrix for the tenth from the center cell of a $2.5 M_{\odot}$ ZAMS model, with black dots showing non-zero entries. The partial derivatives of the equations for cell k form the rows of the blocks. In this case, we have 4 equations for the structure of the model (P , T , L , and r) and 8 equations for the chemical abundances (^1H through ^{24}Mg). Each block of the tridiagonal matrix is demarcated by dashed black vertical lines. The block matrix on the left shows the dependencies of the equations for cell k on the variables of cell $k - 1$, the one in the middle shows the dependencies of the equations for cell k on the variables of cell k , and the one on the right shows the dependencies of the equations for cell k on the variables of cell $k + 1$. The dashed lines partition each each block into four sub-blocks to highlight the structure and abundance portions of each block.

The structure of the lower-right subblocks in the left and right blocks shows that the chemical abundance of a particular species in cell k depends on the chemical abundances of that species in cells $k - 1$ and $k + 1$; this is because of mixing between neighboring cells. The lower-right subblock of the center block also shows the interdependencies of abundances due to nuclear reactions in the cell. The bottom-left subblocks are zero in the left and right blocks but show dependencies on the P and T variables of the center block. This is because the nuclear reactions that change the abundances depend of P and T of that cell but do not depend on P and T in the neighboring cells. The columns for L and r are zero in the center lower-left subblock because the equations for the abundances do not directly depend on those variables. The upper-right subblocks are zero in the left and right blocks but show that the equation for L depends on the abundance variables in the center block. This is because the L equation includes results from nuclear burning, and that depends directly on the composition of cell k but not on the composition in neighboring cells. The other rows in the center upper-right subblock are zero because the equations for P , T , and r do not directly depend on composition.

Finally, consider the upper-left subblocks that show the dependencies of structure equations on structure variables. The upper-left subblock in the center shows that each structure equation in k depends on 3 or 4 of the structure variables in k . The P and T equations for cell k also depend on both of the variables P and T in $k - 1$. While the L and r equations for k depend on the corresponding variables in $k - 1$. This pattern reflects the form of the finite differences in the implementation of the structure equations: P and T differences use the outer neighbor ($k - 1$) while L and r differences use the inner neighbor ($k + 1$). The L and r equations for innermost cell $k = n$ use L_{center} and R_{center} ; the P and T equations for the outermost cell $k = 1$ use the surface boundary conditions.

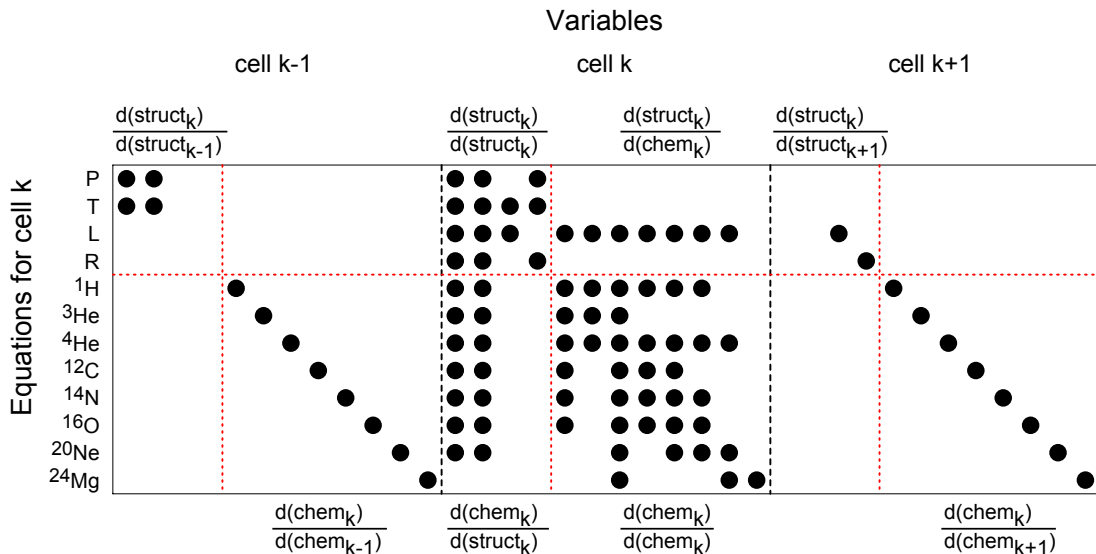


Figure 47. One row of the block tridiagonal Jacobian matrix for a $2.5 M_{\odot}$ ZAMS model, with black dots showing the locations of non-zero entries.

The structure variables for each zone always include the zone average of the natural logarithm of the temperature, $\ln T$, the luminosity at the outer edge of the zone, L , the natural logarithm of the radius at the outer edge of the zone, $\ln r$, and a second thermodynamic variable—either the zone average of the natural logarithm of the mass density, $\ln \rho$, or the the zone average of the natural logarithm of the gas pressure, $\ln P_{\text{gas}}$. Ideally it would not matter whether $\ln \rho$ or $\ln P_{\text{gas}}$ was used as the second thermodynamic variable—for a given temperature and composition the equation of state permits going back and forth between the

two. Microphysics packages tend to use mass density as a primary input (i.e., they use a Helmholtz free energy basis) leading to the common choice of $\ln \rho$. However, the structure equations are solved only to within a finite but non-zero residual (see above). Approximately correct values for the density and temperature can then lead to anomalous pressure profiles, with tiny violations of hydrostatic balance. These local violations tend to appear near large jumps in density, such as at a sharp H/He boundary. Using P_{gas} as the second thermodynamic variable (effectively using a Gibbs free energy basis) removes these anomalous pressure profiles. For example, in stellar models without overshooting or semiconvection, the H/He boundary is extremely sharp. Using the gas pressure as the second thermodynamic variable results in single zone step function transitions in the abundances and in the density, while the temperature and pressure are smooth across the transition. Applications that demand smooth pressure profiles, such as pulsation analysis (see §3), should generally specify the gas pressure as the second thermodynamic variable.

If the optional hydrodynamic mode is activated, then the radial velocity at the outer edge of the cell, v , is added to the structure variables. Figure 47 shows the order of the model variables in the Jacobian: each cell includes the structure variables followed by the mass fraction X_i of each isotope. Mass and the local angular velocity ω are not treated as structure variables because they are held constant during the Newton iterations. The mass is set before the iterations, while ω is determined after convergence. This is computed taking into account loss/gain of angular momentum during the time step, the new stellar structure and internal transport of angular momentum calculated by a diffusion equation (see § B.6).

The program flow to solve the coupled structure, burning, and mixing equations is to first create the matrix of partial derivatives using the current candidate solution, solve the block tridiagonal system of linear equations for the corrections to the basic variables, apply the possibly damped corrections (see next paragraph) to update the candidate solution, and calculate the residual F . Then, if the residual is small enough, we declare victory, otherwise we repeat the general flow with the updated candidate solution.

Each iteration of the Newton solver uses a linear approximation to create a vector of corrections to the model. These corrections do not include the physical requirement that the abundance mass fractions need to remain positive. To reduce the possible occurrence of negative abundances MESA star now uses a damped Newton scheme. This checks for proposed corrections that would produce negative abundances and multiplies the entire correction vector by a factor less than one, so that only part of the full correction is applied. In many cases, this is sufficient to significantly improve the convergence properties of a model. In other cases, the damped correction scheme may force so many small corrections that the Newton solver cannot converge within the user-specified maximum number of iterations, forcing the previous model to be attempted again with a smaller timestep (termed “a backup”). On balance, this is usually a small price to pay for an improved conservation of species and more accurate solutions.

The modules in star provide routines to evaluate the residual equations and create the Jacobian matrix. Given a candidate solution (i.e., the set of basic variables for each cell), the microphysics for each cell (EOS, thermal neutrino loss, opacity, nuclear reaction rates) are evaluated in parallel (see §B.8). The Jacobian matrix is then further populated with elements from rotation, artificial viscosity, and mixing length theory for the temperature gradient, and these are also evaluated in parallel. Each of the routines that evaluate these components returns output values and partial derivatives of the output values with respect to the input values. Analytic partial derivatives are used whenever feasible, otherwise numerical partial derivatives are supplied.

Timestep Controls

Control of the timestep is a critical part of stellar evolution and requires careful trade-offs. The timesteps must be small enough to allow convergence in comparatively few iterations but large enough to allow sufficiently efficient evolutions. Changes to the timestep must respond rapidly to varying structure or composition conditions, but they need to be controlled to avoid large jumps that can reduce the convergence rate or the accuracy of the results. The routine `pick_next_timestep` performs timestep control as a two-stage process. The first stage proposes a new timestep using the H211B low-pass filter (Söderlind & Wang 2006), a scheme based on digital control theory. The second stage implements a wide range of tests that can reduce the proposed timestep if certain selected properties of the model are changing too much in a single timestep.

For the first stage, routine `hydro_timestep` sets the variable for the next timestep, `dt_next`, according to the relative magnitude of changes to the `basic_vars`. The variable reflecting the size of these changes is called `varcontrol` and is calculated by the routine `eval_varcontrol`. For improved stability and response, the low-pass controller uses previous and current values of `varcontrol` to make the next timestep match the `varcontrol_target`, v_t , which is 10^{-4} by default. To make this explicit, let δt_{i-1} , δt_i , and δt_{i+1} be the previous, current, and next timestep, respectively, while $v_{c,i-1}$ and $v_{c,i}$ are the previous and current values of `varcontrol`. The maximum timestep for model $i + 1$ is then determined by

$$\delta t_{i+1} = \delta t_i f \left[\frac{f(v_t/v_{c,i})f(v_t/v_{c,i-1})}{f(\delta t_i/\delta t_{i-1})} \right]^{1/4}, \quad (\text{B1})$$

where $f(x) = 1 + 2 \tan^{-1}[0.5(x - 1)]$. This control scheme allows rapid changes in the timestep without undesirable fluctuations.

The timestep proposed by this low-pass filtering scheme can be reduced in the second stage according to a variety of special tests that have hard and soft limits. If a change exceeds its specified hard limit, the current trial solution for the new step is rejected, and the code is forced to do a retry or a backup. If a change exceeds its specified soft limit, the next timestep is reduced proportionally. The current classes of special cases that can reduce the next timestep are limits based on:

1. Number of Newton iterations required to converge.
2. Maximum absolute change in the mass fraction of hydrogen or helium in any cell.
3. Maximum relative change in any mass fraction at any cell.

4. Magnitude in the relative change in the structure variables in each cell.
5. Nuclear energy generated in each cell for several categories of nuclear reactions.
6. Changes in the luminosity resulting from nuclear burning.
7. Changes at the photosphere in $\ln L$ and T_{eff} .
8. Changes in $\ln \rho_{\text{center}}$, $\ln T_{\text{center}}$, $X(\text{H})_{\text{center}}$, $X(\text{He})_{\text{center}}$.
9. Magnitude of the change in $\log(M/M_{\odot})$ due to winds or accretion.
10. Mass accreted so that compressional heating is correct (see §5.3).
11. Changes in the logarithm of the total angular momentum.
12. Distance moved in the HR diagram.
13. Maximum allowed timestep under any circumstance.
14. Any user specified timestep limit, accomplished by setting `max_years_for_timestep`, in the optional routine `extras_check_model`.

For convergence studies with respect to the timestep it is vital to change the control parameters that are actually setting the timestep. Often, this is just `varcontrol_target`, but in many situations the timestep will be set by one of the special timestep control parameters.

Mesh Controls

Control of the spatial mesh is a key ingredient of a stellar evolution instrument, and requires careful trade-offs. The mesh must respond to gradients in the structure, chemical composition, and energy generation, in order to give an accurate result, but it should not be overly dense since that will unnecessarily increase the cost of the calculation.

Since MESA star allows for simulations with a fixed inner core mass, M_c , the total mass M is $M_c + M_m$ where M_m is the modeled mass. For cell k , MESA star stores the relative cell mass $dq_k = dm_k/M_m$ where dm_k is the mass contained in cell k . The relative mass interior to the outer cell face is $q_k = 1 - \sum_{i=1}^{i=k-1} dq_i$, and the total mass interior to the outer cell face is $m_k = q_k * M_m + M_c$. In all cases, $m_1 = M$ and $q_1 = 1$. We explicitly keep dq_k in addition to q and define q in terms of dq_k to avoid the need for evaluating $q_k - q_{k+1}$ since that can involve the subtraction of almost equal numbers leading to an undesirable loss of precision (Lesaffre et al. 2006). For example, in the outer envelope of a star where the q_k approach 1, the dq_k can be 10^{-12} or smaller. By storing dq_k we have 16 digit precision, whereas in this case, $q_k - q_{k+1}$ would only give us 4 digits at best for the relative cell mass.

MESA star checks the structure and composition profiles of the model at the beginning of each timestep and, if necessary, adjusts the mesh. A single cell can be split into two or more cells and two or more adjacent cells can be merged. In practice, only a small fraction of the cells are changed during a remesh. This minimizes numerical diffusion, aids convergence, and keeps the cost of remeshing relatively small. Remeshing is divided into a planning stage and an adjustment stage.

The planning stage determines which cells to split or merge based on the magnitude of allowed cell-to-cell changes in a variety of mesh functions. Built-in mesh functions include gradients of the mass, radius, pressure, temperature, adiabatic gradient, angular velocity and mass fractions above some threshold. Users can add others by defining their own `other_mesh_functions` routine.

Other controls are provided to increase the sensitivity in regions selected by the user. Examples include increasing the spatial resolution in regions with changes in user-specified abundances with respect to pressure, changes in the energy generation rate with respect to pressure for different types of burning (e.g., the pp chains, CNO cycles, triple- α , and others), for regions near burning or non-burning convective boundaries, and others.

After the mesh functions are evaluated, the relative magnitude of the changes between adjacent cells are determined. The magnitude of change is multiplied by `mesh_delta_coeff` to obtain a weighted mesh function. Cells where the weighted changes are “too large” are marked for splitting, and cells where the changes are “too small” are marked for merging. For example, if the weighted changes in all mesh functions from cells k to $k + n$ are less than 1, the series of cells from k to $k + n$ are marked for merging. If any weighted mesh function changes from cell k to $k + 1$ by an amount greater than 1, the larger of cell k and cell $k + 1$ is marked for splitting. Finally, if adjacent cells have too large of a relative size difference (as defined by `mesh_max_allowed_ratio` which defaults to 2.5), the larger cell is marked for splitting and the check for excessive ratios is repeated. This can lead to a cascade of splitting in order to ensure that cells sizes do not have excessive jumps.

The adjustment stage executes the remesh plan by performing the merge and split operations to calculate new values for basic variables. Special care is taken to use physical knowledge whenever possible when setting new values. For example, conservation of mass is accounted for when determining new densities, and species conservation is used when setting new mass fractions. Energy conservation is used when setting the temperature (see Paper I), and conservation of angular momentum plays a role in determining the angular velocity. Cells to be split are constructed by first performing a monotonicity-preserving cubic interpolation (Steffen 1990) in mass to obtain the luminosities and $\ln r$ values at the new cell boundaries. The new densities are then calculated from the new cell masses and volumes. Next, new composition mass fraction vectors are calculated. For

cells being merged, the mass averaged abundances are used. For cells being split, neighboring cells are used to form a linear approximation of mass fraction for each species as a function of mass coordinate within the cell. The slopes are adjusted so that the mass fractions sum to one everywhere, and the functions are integrated over the new cell mass to determine the abundances.

Mass Adjustment

Mass adjustment for mass loss or accretion is performed at each timestep when `do_evolve_step` calls the routine `do_adjust_mass` (see §B.1). MESA star offers several ways to set the rate of mass change \dot{M} . A constant mass accretion rate (positive \dot{M}) or mass loss rate (negative \dot{M}) can be specified in the input files, a wind can produce a mass loss, the user can set \dot{M} in an `other_wind` routine or in an `other_check_model` routine. When `do_adjust_mass` is called, the timestep dt and the rate of mass change \dot{M} are known, and thus the change in mass, $\delta M = \dot{M} \delta t$.

When there is a change in mass, instead of adding or removing cells, the total mass is changed by modifying the modeled mass M_m , and cell mass sizes are changed by revisions to dq_k which in turn changes cell mass locations q_k (see §B.4). The mass structure is divided into an inner region where the m_k and dm_k are unchanged but the q_k and dq_k change, an outer region where the q_k and dq_k are unchanged but the m_k and dm_k change, and an intermediate blending region where all of these change. The selection of the region boundaries is discussed in detail in Paper I. The implementation of ϵ_{grav} in the newly accreted matter is described in §5.3.

Once the three regions have been defined, the dq_k are updated. In the inner region they are rescaled by $M/(M + \delta M)$. Thus, dm_k , m_k , and X_k have the same value before and after a change in mass. This eliminates the possibility of unwanted numerical diffusion causing unphysical mixing in the center region. In the outer region, cells retain the same value of dq_k to improve convergence in the high entropy parts of the star (Sugimoto et al. 1981). In the intermediate region, the dq_k are uniformly scaled to make $\sum dq_k = 1$.

The chemical mass fractions of cells in the intermediate and outer regions are then updated by summing the abundances between the new cell mass boundaries. This step is not necessary for the inner region since those cells have not changed mass location. In the case of mass accretion, the composition of the outermost cells whose enclosed mass totals δM is set to match the specified accretion abundances. The single cell that is part old material and part newly accreted material is given an appropriately mixed composition.

Finally, to create a somewhat better starting model for the Newton iterations (see §B.2), the $\ln T$ and $\ln \rho$ and $\ln P_{\text{gas}}$ values are revised by monotonic cubic interpolating to the cell center by mass from the values prior to mass adjustment. The $\ln r$ and material speed v are also set by monotonic cubic interpolation to the value at the new outer mass boundary. The angular velocity is set by integrating the angular momentum between the new cell mass boundaries and using the new $\ln r$ values, conserving the total angular momentum to the floating point limit of the arithmetic.

Evolving the Angular Velocity

Initialization of rotation in MESA star begins from a non-rotating model. The angular velocity ω is added to the set of model variables and initialized to a constant value throughout the model (i.e., solid body rotation). The initial value of ω can be specified as a surface rotational velocity (in km/s) or as a fraction of the critical rotation rate (see §6). During the subsequent evolution, ω is changed at each timestep by remeshing, mass adjustment, radius adjustment (as part of the structure evolution), optional extra angular momentum removal in the outer layers, and the transport of angular momentum optionally with user-defined source terms for external torques.

The angular velocity ω is defined at cell boundaries. Thus $\text{omega}(\mathbf{k})$ is at the outer boundary of cell \mathbf{k} , which is the same location as the radius, $r(\mathbf{k})$, the specific moment of inertia, $i_{\text{rot}}(\mathbf{k})$, and the specific angular momentum, $j_{\text{rot}}(\mathbf{k})$. The mass associated with $\text{omega}(\mathbf{k})$ spans the range from the center by mass of cell \mathbf{k} outward to the center by mass of cell $\mathbf{k}-1$ and is referred to as $\text{dm_bar}(\mathbf{k})$ to distinguish it from the cell mass $\text{dm}(\mathbf{k})$.

The remeshing operation splits and merges cells but does not change the physical stellar structure (see §B.4). For regions where there has been a change in the mesh, the values of ω are adjusted to give the same angular momentum as before. More specifically, the angular momentum from the original model is summed over the mass range encompassed by the new $\text{dm_bar}(\mathbf{k})$, and $\text{omega}(\mathbf{k})$ is adjusted to give the same total for the new model.

During the mass adjustment operation, when mass is added or removed from the model, cells in the outer layers are moved to new mass locations (see §B.5). As part of this process, the angular velocity values are updated to conserve angular momentum using the same scheme as for remeshing: sum the angular momentum in the original model and set $\text{omega}(\mathbf{k})$ in the new model to conserve it. Newly added material from accretion is given the current surface angular velocity. In the case of mass loss, this operation removes the amount of angular momentum contained in the lost mass at the start of the timestep; it does not deal with possible transport of angular momentum into the lost mass during the timestep. That is dealt with by an optional, user-specified removal prior to the angular momentum transport.

MESA star performs the transport of angular momentum as a separate operation from the evolution of structure and composition. This is done in order to obtain high accuracy in the angular momentum transport by using substeps and quad-precision linear algebra. It does not introduce additional operator splitting errors since ω is not used in the structure and abundance equations. So we solve for the new structure and composition after any mass change and before the transport of angular momentum. Calculation of the new stellar structure changes the radii but does not change the mass partitioning of the model (see §B.2). Given the new radius $r(\mathbf{k})$, we calculate the new $i_{\text{rot}}(\mathbf{k})$. Then using the unchanged $j_{\text{rot}}(\mathbf{k})$, $\text{omega}(\mathbf{k})$ is set to $j_{\text{rot}}(\mathbf{k})/i_{\text{rot}}(\mathbf{k})$ to conserve specific angular momentum. Since $\text{dm_bar}(\mathbf{k})$ has not changed, this also conserves total angular momentum.

Next, MESA star applies an optional, user-specified amount of angular momentum loss in the outer surface layers. This is to account for possible transport of angular momentum during the timestep from these outer layers into the mass removed by the mass adjustment operation.

The final operation is the transport of angular momentum within the star, which is treated with a diffusion approximation (Endal & Sofia 1978; Pinsonneault et al. 1989; Heger et al. 2000)

$$\left(\frac{\partial\omega}{\partial t}\right)_m = \frac{1}{i} \left(\frac{\partial}{\partial m}\right)_i \left[(4\pi r^2 \rho)^2 \nu \left(\frac{\partial\omega}{\partial m}\right)_i \right] - \frac{2\omega}{r} \left(\frac{\partial r}{\partial t}\right)_m \left(\frac{1}{2} \frac{d \ln i}{d \ln r}\right), \quad (\text{B2})$$

where i is the specific moment of inertia of a shell at mass coordinate m , and ν is the turbulent viscosity determined as the sum of the diffusion coefficients for convection, double diffusion, overshooting and rotationally-induced instabilities (see §6). The diffusive transport is carefully implemented to accurately conserve angular momentum. The angular momentum associated with location k is $\text{dm.bar}(k) * \text{i.rot}(k) * \text{omega}(k)$. The change in angular momentum for k is determined by the flux in angular momentum from $k - 1$ to k and from $k + 1$ to k . The flux from $k - 1$ to k is set by $\nu(k - 1)$ and the difference between $\text{omega}(k)$ and $\text{omega}(k-1)$. The flux from $k + 1$ to k is found similarly using $\nu(k)$ and the difference between $\text{omega}(k)$ and $\text{omega}(k+1)$. Source terms for location k are applied by user-supplied values for `extra_jdot(k)` or `extra_omegadot(k)`. The finite difference equation for the effects of the transport and source terms is solved over the stellar timestep with an implicit time integration that uses multiple smaller timesteps. The sizes of these substeps are determined by the timescale set by the diffusion coefficients and the differences in ω . It is not unusual to use 10 or more substeps to evolve $\text{omega}(k)$ over the stellar timestep. Each implicit substep is solved using a quad-precision tridiagonal matrix routine. The conservation of total angular momentum is monitored and the stellar timestep is rejected if there is any deviation from conservation by more than a user-specified factor. In practice, we find the total angular momentum is conserved over the stellar timestep to within a few digits of the floating point limit of the arithmetic.

Nuclear Reactions

A reaction network is defined by a set of isotopes and a set of reactions; these sets are specified in a reaction network definition file. MESA comes with many predefined reaction networks in `data/net_data/nets` and can also incorporate user-defined networks. To use a custom network, a user creates a reaction network definition file containing the command `add_isos_and_reactions(isos_list)`, which will automatically add all reactions linking the isotopes in `isos_list`. The sequence of isotopes in `isos_list` may be specified by the name of the isotope: for example, `add_isos_and_reactions(he4)` adds ${}^4\text{He}$. Alternatively, one can specify the name of element followed by the desired minimum and maximum nucleon number. For example, the command `add_isos_and_reactions(o 16 18)` adds ${}^{16}\text{O}$, ${}^{17}\text{O}$, and ${}^{18}\text{O}$. Note that because many of the predefined networks may use effective rates—that is, using one reaction rate to represent a reaction sequence or group of reaction sequences—it is not recommended that the user extend one of the pre-existing networks with this command.

MESA creates and stores reaction rate tables for each reaction whose entries are derived from evaluating standard analytic fitting formulas (see §A.4), but these reaction rates may be replaced with user-specified values. To change a rate for a given reaction,

1. create a file with two columns: the temperature in units of 10^8 K and the rate $N_A \langle \sigma v \rangle$ in units of $\text{cm}^3 \text{g}^{-1} \text{s}^{-1}$;
2. list the file name in a local file `rate_list.txt` along with its “handle” for the reaction rate in question (see discussion below); and
3. set the parameter `rate_tables_dir` in the namelist `star_job` to the name of the directory in which `rate_list.txt` is located; by default this is `data/rates/rate_tables`.

The handle for a reaction is derived from the input and output channel isotopes according to a few rules. Capture reactions, such as $x(p, \gamma)y$, have handles of the form `r_x_pg_y` and exchange reactions, such as $x(\alpha, p)y$, have handles of the form `r_x_ap_y`. Other arbitrary reactions may be added by listing them in a form `r_inputs_to_outputs` where `inputs` and `outputs` are isotopes separated by “-”. If the same isotope appears two or more times, the isotope name may be repeated. For example, the triple- α reaction is specified as `r_he4_he4_he4_to_c12`. Isotopes are ordered by increasing Z and N , e.g., `r_h3_be7_to_neut_h1_he4_he4`. To see a list of reactions used, the parameter `show_net_reactions_info` in namelist `star_job` should be set to `.true.`

Multicore Performance

MESA implements shared memory multiprocessing via OpenMP¹¹. Paper I explored the runtime scaling of MESA `star` which at that time used a banded matrix linear algebra solver that did not benefit from multiple cores. A large part of the performance improvement in MESA `star` since Paper I comes from converting to a parallel block tridiagonal linear algebra solver derived from BCYCLIC (Hirshman et al. 2010). This improved solver is particularly important since linear algebra is typically the largest part of the runtime in MESA `star`. In addition, the new algorithm has the desirable property of producing numerically identical results independent of the number of cores, an attribute that is not generally true of parallel matrix solvers.

Our test case is a $1.5 M_\odot$ model with $Z = 0.02$ that is evolved from the ZAMS until the central H mass fraction falls to 0.35. This model includes 25 isotopes and 4 structure variables per cell with a variable number of zones typically exceeding 1700. The test takes ~ 55 time steps to cover ~ 1.4 Gyr and uses the default amount of I/O.

Figure 48 shows the scaling behavior of some key components of MESA `star` under GFORTRAN 4.7.2. on a 12 core 2010 Apple MacPro. The dotted line shows the ideal scaling relation where doubling the number of cores cuts the run time in half. The linear algebra, labeled “mtx,” dominates the total run time as the number of cores increases. For example, in the case of 12 cores it accounts for about half the total and is 2.5 times larger than “net”, the evaluation of the nuclear reaction network. The

¹¹ <http://www.openmp.org>

net evaluations closely approach the ideal scaling behavior because they can be done in parallel, each cell independent of the others, with one core working on one cell at a time. The equation of state component, labeled “eos,” also closely approaches the ideal scaling law while consuming less than a third of the run time for the net. The component labeled “eqns,” which includes the evaluation of the structure equations and the creation of the block tridiagonal matrix, also is close to the ideal scaling law and costs about the same as the eos. The “other” component is everything else. It is dominated by processes that currently are not efficient to parallelize because of the relatively large overhead for OpenMP operations. Consequently it remains at roughly a constant run time independent of the number of cores. When a significantly larger number of cores per processor becomes available, the larger operations in this category will have to be reworked or they will dominate the total run time.

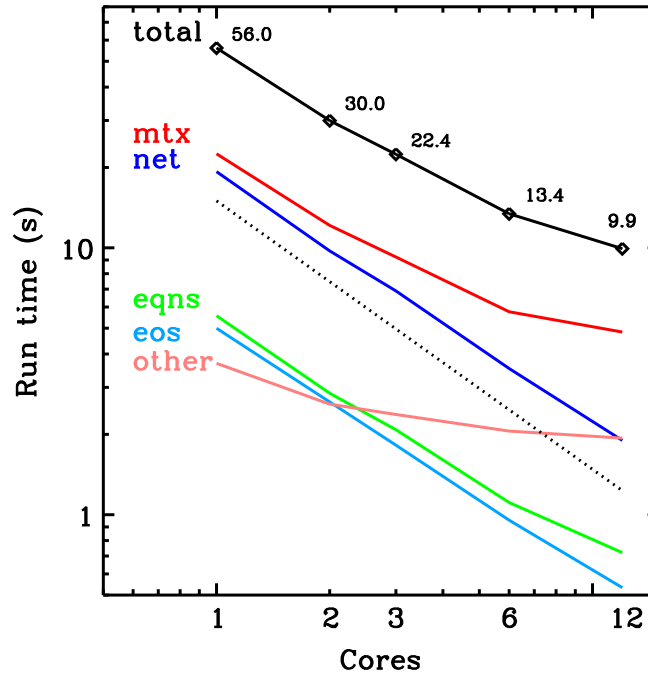


Figure 48. Scaling behavior of various components of MESA star using 1, 2, 3, 6, and 12 cores. The top curve shows the total run time, and the lower solid curves show the run times for the components of the total. The dotted line shows the ideal scaling relation.

The run time also depends on the hardware, the quality of the compiled code, and the efficiency of the OpenMP implementation. For example, when the test case was rerun using IFORT 12.0.4 on the same 12-core machine, we found that GFORTRAN was 6% faster than IFORT on one core but took 19% longer than IFORT on 12 cores. As another example, we ran the test case under GFORTRAN 4.7.2 on a 40-core server. While we obtained a speedup of 5.6 in going from 1 to 12 cores for the 12 core machine (see Figure 48), we find a speedup of only 4.8 on the 40-core server in going from 1 to 12 cores. Moreover, the speedup per core dropped steeply beyond 8–12 cores on the 40-core server, confirming the expectation that much work will be required to make full use of machines with many cores.

Operating System and Compiler Considerations

We next consider the range of values that are obtained when running on different operating systems and with different compilers and options. Such a comparison is important because computer hardware and software are heterogeneous and, under some circumstances, may give different answers.

For this comparison we use two different systems, both with Intel Xeon processors, and either Linux (Cent OS 5.7) or Mac OS X (10.7.5). Both systems have Fortran compilers from GNU (version 4.7.2) and Intel (version 12). In addition to these operating system and compiler configurations, we consider effects of optimization and OpenMP multiprocessing. The default for compiling MESA is to enable OpenMP and use optimization at the `-O2` level. Here we compare results across the different operating systems, compilers, and without OpenMP or without optimization (i.e., `-O0`). These comparisons were carried out with MESA revision 4692. The test run is the solar calibration `test_suite` case with an absolute tolerance of 10^{-5} .

The following is a summary of our findings. On both operating systems MESA compiled by the GNU compiler with optimization and OpenMP support produces runs that are identical, to machine precision, with runs compiled by the same compiler but with either OpenMP or optimization disabled. The same is not true of the Intel compiler, for which we find that the calibrated values vary slightly, but within the specified tolerances, for runs with different numbers of threads. MESA running on the Linux system compiled with either compiler and the default options gives calibrated values that are compatible within the specified tolerances, but not identical to, those obtained using the same compiler and compiler options on the Mac OS X system.

We found that the GNU and Intel compilers with optimization and OpenMP support produce somewhat different results. The difference is present on both Mac OS X and Linux operating systems. For our test configuration, MESA compiled with the Intel compiler produced values for the solar-calibrated model that are smaller than those obtained from MESA compiled with the GNU

Table 6
Principal components of the MESA Software Development Kit

Name	Purpose	Version	License ^a
GFORTTRAN	Compiler	4.7.2	Open source (GPL ver. 2)
BLAS	Matrix algebra	2011-04-19	Open source (other)
LAPACK	Matrix algebra	3.4.2	Open source (other)
HDF5	File storage	1.8.9	Open source (other)
NDIFF	Numerical comparison	2.00	Open source (GPL ver. 2)
PGPLOT	Plotting	5.2.2	Open source (non-commercial)
SE	File storage	1.2.1	Open source (other)

^a“GPL” denotes the GNU General Public License (with the version in parentheses); “non-commercial” denotes an open-source license with restrictions on commercial distribution; and “other” denotes to a variety of open-source licenses which permit largely unrestricted distribution.

compiler by ~ 0.01 in both initial Y and α_{MLT} . Efforts will be made in the future to uncover the causes of these differences and eliminate them if possible.

Visualization

MESA star provides alphanumeric output at user-specified regular intervals. In addition, the routines in module `star/public/pgstar.f` provide an option for concurrent graphical output with the PGPLOT¹² library to create on-screen plots that can be saved for post-processing into animations of an evolutionary sequence. A variety of options are provided and are all configurable through the PGstar inlist. For example, a PGstar X11 window can simultaneously hold an H-R diagram, a T_c - ρ_c diagram, and interior profiles of physical variables, such as nuclear energy generation and composition. The PGstar inlist is read at each timestep, so the display options can be changed without have to stop MESA star.

Since Paper I, a number of MESA star users have developed and released toolkits¹³ to visualize the alphanumeric output with common graphical packages including: Mathematica scripts (contributed by Richard O’Shaughnessy) and the intuitive and efficient graphical user interface MESAface (Giannotti et al. 2012); MatLab utilities (contributed by Dave Spiegel and Gongjie Li); IDL functions (contributed by Rich Townsend); Python scripts (contributions from Falk Herwig and the NuGrid collaboration, David Kaplan, Alfred Gautschy, William Wolf); and Tioga scripts (contributed by Christopher Mankovich and Bill Paxton).

THE MESA SOFTWARE DEVELOPMENT KIT

MESA is provided as source code, allowing users access to all of the implementation details. Installation necessarily involves building the code from source, which is a non-trivial task. A successful build requires cooperation between the operating system, compiler, libraries, and utilities.

To address this issue we have created the MESA Software Development Kit (SDK), which packages everything necessary to establish a unified and maintained build environment. The principal components of the SDK are summarized in Table 6; all of these are distributed under an open-source license (detailed in the table), permitting their redistribution without financial or copyright encumbrances. Perhaps the most important component is the GFORTRAN compiler, part of the GNU Compiler Collection. GFORTRAN implements almost all of the Fortran 2003 (F2003) standard, and benefits from a high level of community support.

The SDK is available for Intel x86 and x86-64 CPU architectures running the Linux and Mac OS X operating systems (these platforms comprise most of the MESA user base). Installation of the kit is straightforward, requiring a tar archive to be unpacked (Linux) or an application folder to be copied (OS X), followed by the initialization of a few environment variables. By default, MESA is configured to compile “out-of-the-box” with the SDK. MESA can also be compiled without the SDK, using any alternate compiler which supports the F2003 standard. In this respect, GFORTRAN should not be viewed as *the* MESA compiler (nor the full SDK as *the* MESA build environment). MESA will adhere to Fortran standards rather than rely on vendor-specific extensions.

Uptake of the SDK has been very rapid: at the time of writing, we estimate over 90% of the MESA community (over 500 users) are using the SDK. This growth has been matched by a significant decline in the number of installation support requests, and a corresponding reduction in the time taken to resolve these requests. With these maintenance overheads curbed, the MESA developers are able to devote more of their time to refining and extending the code.

REFERENCES

- Alibert, Y., Mordasini, C., & Benz, W. 2011, *A&A*, 526, A63
Allard, F., Hauschildt, P. H., Alexander, D. R., Tamanai, A., & Schweitzer, A. 2001, *ApJ*, 556, 357
Althaus, L. G., Serenelli, A. M., Córscico, A. H., & Montgomery, M. H. 2003, *A&A*, 404, 593
Angulo, C., et al. 1999, *Nuclear Physics A*, 656, 3
Arcoragi, J.-P., & Fontaine, G. 1980, *ApJ*, 242, 1208
Böhm-Vitense, E. 1958, *Zeitschrift für Astrophysik*, 46, 108
Baglin, A., Auvergne, M., Barge, P., Deleuil, M., Michel, E., & CoRoT Exoplanet Science Team. 2009, in *IAU Symposium*, Vol. 253, IAU Symposium, 71–81
Bahcall, J. N., Basu, S., & Pinsonneault, M. H. 1998, *Physics Letters B*, 433, 1
Balbus, S. A., Latter, H., & Weiss, N. 2012, *MNRAS*, 420, 2457
Bass, G., Orosz, J. A., Welsh, W. F., Windmiller, G., Ames Gregg, T., Fetherolf, T., Wade, R. A., & Quinn, S. N. 2012, *ArXiv e-prints*
Beck, P. G., et al. 2012, *Nature*, 481, 55
Bergeron, P., Wesemael, F., Lamontagne, R., Fontaine, G., Saffer, R. A., & Allard, N. F. 1995, *ApJ*, 449, 258
Bildsten, L., Paxton, B., Moore, K., & Macias, P. J. 2012, *ApJ*, 744, L6
Bisnovatyi-Kogan, G. S., & Dorodnitsyn, A. V. 1999, *A&A*, 344, 647
Bloeker, T. 1995, *A&A*, 297, 727
Böhm, K. H., & Cassinelli, J. 1971, *A&A*, 12, 21

¹² <http://www.astro.caltech.edu/~tjp/pgplot/>.

¹³ See <http://mesastar.org/tools-utilities>.

- Bonanno, A., Küker, M., & Paternò, L. 2007, *A&A*, 462, 1031
- Borucki, W., et al. 2009, in *IAU Symposium*, Vol. 253, *IAU Symposium*, 289–299
- Boss, A. P. 2011, *ApJ*, 731, 74
- Braithwaite, J. 2006, *A&A*, 449, 451
- Brassard, P., Fontaine, G., Wesemael, F., Kawaler, S. D., & Tassoul, M. 1991, *ApJ*, 367, 601
- Brott, I., et al. 2011, *A&A*, 530, A115
- Burkert, J., Quataert, E., Arras, P., & Weinberg, N. N. 2012a, *ArXiv e-prints* — 2012b, *MNRAS*, 421, 983
- Calder, A. C., et al. 2007, *ApJ*, 656, 313
- Cantiello, M., & Langer, N. 2010, *A&A*, 521, A9
- Cantiello, M., et al. 2009, *A&A*, 499, 279
- Carlberg, J. K., Cunha, K., Smith, V. V., & Majewski, S. R. 2012, *ApJ*, 757, 109
- Carter, J. A., et al. 2011, *Science*, 331, 562
- Cassisi, S., Potekhin, A. Y., Pietrinferni, A., Catelan, M., & Salaris, M. 2007, *ApJ*, 661, 1094
- Chang, P., & Hui, L. 2011, *ApJ*, 732, 25
- Charbonnel, C., & Zahn, J.-P. 2007, *A&A*, 467, L15
- Chatzopoulos, E., Robinson, E. L., & Wheeler, J. C. 2012, *ApJ*, 755, 95
- Chatzopoulos, E., & Wheeler, J. C. 2012, *ApJ*, 748, 42
- Christensen-Dalsgaard, J. 2008a, *Ap&SS*, 316, 113
- 2008b, *Ap&SS*, 316, 13
- Christensen-Dalsgaard, J., & Thompson, M. J. 1997, *MNRAS*, 284, 527
- Christensen-Dalsgaard, J., et al. 1996, *Science*, 272, 1286
- Cox, J. P., & Giuli, R. T. 1968, *Principles of stellar structure* (New York: Gordon and Breach)
- Cybur, R. H., et al. 2010, *ApJS*, 189, 240
- Davis, A.-C., Lim, E. A., Sakstein, J., & Shaw, D. J. 2012, *Phys. Rev. D*, 85, 123006
- de Bruijne, J. H. J. 2012, *Ap&SS*, 341, 31
- de Jager, C., Nieuwenhuijzen, H., & van der Hucht, K. A. 1988, *A&AS*, 72, 259
- Deheuvels, S., & Michel, E. 2011, *A&A*, 535, A91
- Deheuvels, S., et al. 2010, *A&A*, 515, 87
- Denissenkov, P. A. 2010, *ApJ*, 723, 563
- 2012, *ApJ*, 753, L3
- Denissenkov, P. A., Herwig, F., Bildsten, L., & Paxton, B. 2013, *ApJ*, 762, 8
- Denissenkov, P. A., & Pinsonneault, M. 2007, *ApJ*, 655, 1157
- 2008, *ApJ*, 684, 626
- Dotter, A., Chaboyer, B., Jevremović, D., Kostov, V., Baron, E., & Ferguson, J. W. 2008, *ApJS*, 178, 89
- Eggenberger, P., Meynet, G., Maeder, A., Hirschi, R., Charbonnel, C., Talon, S., & Ekström, S. 2008, *Ap&SS*, 316, 43
- Eggenberger, P., Montalbán, J., & Miglio, A. 2012, *A&A*, 544, L4
- Ekström, S., et al. 2012, *A&A*, 537, A146
- Endal, A. S., & Sofia, S. 1976, *ApJ*, 210, 184
- 1978, *ApJ*, 220, 279
- Evans, C. J., et al. 2011, *A&A*, 530, A108
- Ferguson, J. W., Alexander, D. R., Allard, F., Barman, T., Bodnarik, J. G., Hauschildt, P. H., Heffner-Wong, A., & Tamanai, A. 2005, *ApJ*, 623, 585
- Fischer, D. A., & Valentí, J. 2005, *ApJ*, 622, 1102
- Fortney, J. J., Saumon, D., Marley, M. S., Lodders, K., & Freedman, R. S. 2006, *ApJ*, 642, 495
- Freedman, R. S., Marley, M. S., & Lodders, K. 2008, *ApJS*, 174, 504
- Friend, D. B., & Abbott, D. C. 1986, *ApJ*, 311, 701
- Frommhold, L., Abel, M., Wang, F., Gustafsson, M., Li, X., & Hunt, K. 2010, *Molecular Physics*, 108, 2265
- Fuller, J., & Lai, D. 2012a, *ArXiv e-prints* — 2012b, *ApJ*, 756, L17
- Georgy, C., Ekström, S., Meynet, G., Massey, P., Levesque, E. M., Hirschi, R., Eggenberger, P., & Maeder, A. 2012, *A&A*, 542, A29
- Georgy, C., Meynet, G., & Maeder, A. 2011, *A&A*, 527, A52
- Giannotti, M., Wise, M., & Mohammed, A. 2012, *ArXiv e-prints*
- Glebbeek, E., Gaburov, E., de Mink, S. E., Pols, O. R., & Portegies Zwart, S. F. 2009, *A&A*, 497, 255
- Gough, D. O. 1986, in *Hydrodynamic and Magnetodynamic Problems in the Sun and Stars*, ed. Y. Ōsaki, 117
- Grevesse, N., & Noels, A. 1993, in *Origin and Evolution of the Elements*, ed. N. Prantzos, E. Vangioni-Flam, & M. Casse, 15–25
- Grevesse, N., & Sauval, A. J. 1998, *Space Sci. Rev.*, 85, 161
- Guillot, T. 2010, *A&A*, 520, A27
- Guillot, T., & Morel, P. 1995, *A&AS*, 109, 109
- Hairer, E., & Wanner, G. 1996, *Solving Ordinary Differential Equations. II. Stiff and Differential-Algebraic Problems*, 2nd edn. (Berlin: Springer)
- Heger, A., Jeannin, L., Langer, N., & Baraffe, I. 1997, *A&A*, 327, 224
- Heger, A., & Langer, N. 1998, *A&A*, 334, 210
- 2000, *ApJ*, 544, 1016
- Heger, A., Langer, N., & Woosley, S. E. 2000, *ApJ*, 528, 368
- Heger, A., Woosley, S. E., & Spruit, H. C. 2005, *ApJ*, 626, 350
- Henry, L., Vardya, M. S., & Bodenheimer, P. 1965, *ApJ*, 142, 841
- Herwig, F. 2000, *A&A*, 360, 952
- 2004, *ApJS*, 155, 651
- Hirschi, R., Meynet, G., & Maeder, A. 2004, *A&A*, 425, 649
- Hirshman, S. P., Perumalla, K. S., Lynch, V. E., & Sanchez, R. 2010, *J. Comput. Phys.*, 229, 6392
- Hooke, R., & Jeeves, T. A. 1961, *J. ACM*, 8, 212
- Huang, X., & Cumming, A. 2012, *ApJ*, 757, 47
- Hubickyj, O., Bodenheimer, P., & Lissauer, J. J. 2005, *Icarus*, 179, 415
- Hunter, I., et al. 2007, *A&A*, 466, 277
- Iben, Jr., I. 1991, *ApJS*, 76, 55
- Iglesias, C. A., & Rogers, F. J. 1993, *ApJ*, 412, 752
- 1996, *ApJ*, 464, 943
- Iglesias, C. A., Rogers, F. J., & Wilson, B. G. 1992, *ApJ*, 397, 717
- Imbriani, G., et al. 2004, *A&A*, 420, 625
- Irwin, J. M., et al. 2011, *ApJ*, 742, 123
- Ivezic, Z., et al. 2008, *ArXiv e-prints*
- Joss, P. C., Salpeter, E. E., & Ostriker, J. P. 1973, *ApJ*, 181, 429
- Kaiser, N., et al. 2010, in *Society of Photo-Optical Instrumentation Engineers (SPIE) Conference Series*, Vol. 7733, *Society of Photo-Optical Instrumentation Engineers (SPIE) Conference Series*
- Kippenhahn, R., Ruschenplatt, G., & Thomas, H.-C. 1980, *A&A*, 91, 175
- Kippenhahn, R., & Thomas, H.-C. 1970, in *IAU Colloq. 4: Stellar Rotation*, ed. A. Slettebak, 20
- Kjeldsen, H., & Bedding, T. R. 1995, *A&A*, 293, 87
- Kjeldsen, H., Bedding, T. R., & Christensen-Dalsgaard, J. 2008, *ApJ*, 683, L175
- Koch, D. G., et al. 2010, *ApJ*, 713, L79
- Krishnamurti, R. 2003, *Journal of Fluid Mechanics*, 483, 287
- Küker, M., Rüdiger, G., & Kitchatinov, L. L. 2011, *A&A*, 530, A48
- Kunz, R., Fey, M., Jaeger, M., Mayer, A., Hammer, J. W., Staudt, G., Harissopoulos, S., & Paradelis, T. 2002, *ApJ*, 567, 643
- Langer, N. 1997, in *Astronomical Society of the Pacific Conference Series*, Vol. 120, *Luminous Blue Variables: Massive Stars in Transition*, ed. A. Nota & H. Lamers, 83
- Langer, N. 1998, *A&A*, 329, 551
- 2012, *ARA&A*, 50, 107
- Langer, N., Fricke, K. J., & Sugimoto, D. 1983, *A&A*, 126, 207
- Langer, N., Heger, A., Wellstein, S., & Herwig, F. 1999, *A&A*, 346, L37
- Laughlin, G., Bodenheimer, P., & Adams, F. C. 2004, *ApJ*, 612, L73
- Law, N. M., et al. 2009, *PASP*, 121, 1395
- Lesaffre, P., Han, Z., Tout, C. A., Podsiadlowski, P., & Martin, R. G. 2006, *MNRAS*, 368, 187
- Li, Y., & Gong, Z. G. 1994, *A&A*, 289, 449
- Liu, C., Bailer-Jones, C. A. L., Sordo, R., Vallenari, A., Borrachero, R., Luri, X., & Sartoretti, P. 2012, *MNRAS*, 426, 2463
- Lloyd, J. P. 2011, *ApJ*, 739, L49
- Lodders, K. 2003, *ApJ*, 591, 1220
- MacDonald, J., & Mullan, D. J. 2012, *MNRAS*, 421, 3084
- Maeder, A. 1987a, *A&A*, 173, 247
- 1987b, *A&A*, 178, 159
- 2009, *Physics, Formation and Evolution of Rotating Stars* (Berlin: Springer)
- Maeder, A., & Meynet, G. 2000a, *A&A*, 361, 159
- 2000b, *ARA&A*, 38, 143
- 2003, *A&A*, 411, 543
- 2004, *A&A*, 422, 225
- Maeder, A., & Zahn, J.-P. 1998, *A&A*, 334, 1000
- Medin, Z., & Cumming, A. 2010, *Phys. Rev. E*, 81, 036107
- Metcalfe, T. S., et al. 2012, *ApJ*, 748, L10
- Meynet, G., & Maeder, A. 1997, *A&A*, 321, 465
- 2000, *A&A*, 361, 101
- Mihalas, D. 1978, *Stellar atmospheres /2nd edition/* (San Francisco, W. H. Freeman and Co.)
- Mohr, P. J., Taylor, B. N., & Newell, D. B. 2008, *Reviews of Modern Physics*, 80, 633
- Monteiro, M. J. P. F. G., ed. 2009, *Astrophysics and Space Science*, Vol. 316, *Evolution and Seismic Tools for Stellar Astrophysics* (Springer)
- Moravvejhi, E., Moya, A., & Guinan, E. F. 2012, *ApJ*, 749, 74
- Mosser, B., et al. 2012, *A&A*, 548, A10
- Mugrauer, M., & Neuhäuser, R. 2009, *A&A*, 494, 373
- Nomoto, K. 1982, *ApJ*, 253, 798
- Nomoto, K., & Sugimoto, D. 1977, *PASJ*, 29, 765
- Nugis, T., & Lamers, H. J. G. L. M. 2000, *A&A*, 360, 227
- Owocki, S. P., Gayley, K. G., & Shaviv, N. J. 2004, *ApJ*, 616, 525
- Paczyński, B. 1969, *Acta Astron.*, 19, 1
- 1970, *Acta Astron.*, 20, 47
- Pamyatnykh, A. A. 1999, *Acta Astron.*, 49, 119
- Passy, J.-C., Mac Low, M.-M., & De Marco, O. 2012, *ApJ*, 759, L30
- Patience, J., et al. 2002, *ApJ*, 581, 654
- Paxton, B., Bildsten, L., Dotter, A., Herwig, F., Lesaffre, P., & Timmes, F. 2010, *ApJS*, 192, 3
- Petrovic, J., Langer, N., Yoon, S.-C., & Heger, A. 2005, *A&A*, 435, 247
- Pinsonneault, M. H., Kawaler, S. D., Sofia, S., & Demarque, P. 1989, *ApJ*, 338, 424
- Pollack, J. B., Hubickyj, O., Bodenheimer, P., Lissauer, J. J., Podolak, M., & Greenzweig, Y. 1996, *Icarus*, 124, 62
- Potekhin, A. Y., & Chabrier, G. 2010, *Contributions to Plasma Physics*, 50, 82
- Potter, A. T., Tout, C. A., & Brott, I. 2012a, *MNRAS*, 2883
- Potter, A. T., Tout, C. A., & Eldridge, J. J. 2012b, *MNRAS*, 419, 748

- Powell, M. 2009, The BOBYQA algorithm for bound optimization without derivatives, Tech. rep., Department of Applied Mathematics and Theoretical Physics, University of Cambridge
- Rauscher, T., & Thielemann, F. 2000, *At. Data Nucl. Data Tables*, 75, 1
- Reimers, D. 1975, in *Problems in stellar atmospheres and envelopes.*, ed. B. Baschek, W. H. Kegel, & G. Traving (New York: Springer-Verlag), 229–256
- Roell, T., Neuhäuser, R., Seifahrt, A., & Mugrauer, M. 2012, *A&A*, 542, A92
- Rogers, F. J., & Nayfonov, A. 2002, *ApJ*, 576, 1064
- Rohrman, R. D. 2001, *MNRAS*, 323, 699
- Rohrman, R. D., Althaus, L. G., García-Berro, E., Corsico, A. H., & Miller Bertolami, M. M. 2012, *ArXiv e-prints*
- Ruediger, G., von Rekowski, B., Donahue, R. A., & Baliunas, S. L. 1998, *ApJ*, 494, 691
- Saumon, D., Chabrier, G., & van Horn, H. M. 1995, *ApJS*, 99, 713
- Schneider, A. S., Hughto, J., Horowitz, C. J., & Berry, D. K. 2012, *Phys. Rev. E*, 85, 066405
- Seager, S., & Deming, D. 2010, *ARA&A*, 48, 631
- Söderlind, G., & Wang, L. 2006, *J. Comput. Appl. Math.*, 185, 225
- Spruit, H. C. 2002, *A&A*, 381, 923
- Steffen, M. 1990, *A&A*, 239, 443
- Stello, D., et al. 2009, *ApJ*, 700, 1589
- Straniero, O., Domínguez, I., Imbriani, G., & Piersanti, L. 2003, *ApJ*, 583, 878
- Sugimoto, D., Nomoto, K., & Eriguchi, Y. 1981, *Progress of Theoretical Physics Supplement*, 70, 115
- Suijs, M. P. L., Langer, N., Poelarends, A.-J., Yoon, S.-C., Heger, A., & Herwig, F. 2008, *A&A*, 481, L87
- Tassoul, M. 1980, *ApJS*, 43, 469
- Thompson, M. J., Christensen-Dalsgaard, J., Miesch, M. S., & Toomre, J. 2003, *ARA&A*, 41, 599
- Timmes, F. X. 1999, *ApJS*, 124, 241
- Timmes, F. X., & Swesty, F. D. 2000, *ApJS*, 126, 501
- Torres, G., Andersen, J., & Giménez, A. 2010, *A&A Rev.*, 18, 67
- Townsley, D. M., & Bildsten, L. 2004, *ApJ*, 600, 390
- Traxler, A., Garaud, P., & Stellmach, S. 2011, *ApJ*, 728, L29
- Udry, S., & Santos, N. C. 2007, *ARA&A*, 45, 397
- Ulrich, R. K. 1972, *ApJ*, 172, 165
- Unno, W., Osaki, Y., Ando, H., Saio, H., & Shibahashi, H. 1989, *Nonradial Oscillations of Stars* (Tokyo: University of Tokyo Press)
- Ushomirsky, G., Matzner, C. D., Brown, E. F., Bildsten, L., Hilliard, V. G., & Schroeder, P. C. 1998, *ApJ*, 497, 253
- van Saders, J. L., & Pinsonneault, M. H. 2012, *ApJ*, 751, 98
- Vink, J. S., de Koter, A., & Lamers, H. J. G. L. M. 2001, *A&A*, 369, 574
- von Zeipel, H. 1924, *MNRAS*, 84, 665
- Wachlin, F. C., Miller Bertolami, M. M., & Althaus, L. G. 2011, *A&A*, 533, A139
- Woosley, S. E. 1993, *ApJ*, 405, 273
- Woosley, S. E., & Heger, A. 2006, *ApJ*, 637, 914
- Yang, X. H., Fu, J. N., & Zha, Q. 2012, *AJ*, 144, 92
- Yoon, S.-C., & Cantiello, M. 2010, *ApJ*, 717, L62
- Yoon, S.-C., & Langer, N. 2005, *A&A*, 443, 643
- Yoon, S.-C., Langer, N., & Norman, C. 2006, *A&A*, 460, 199
- Yoon, S.-C., Woosley, S. E., & Langer, N. 2010, *ApJ*, 725, 940
- York, D. G., et al. 2000, *AJ*, 120, 1579
- Young, P. A., Liebst, K., & Pagano, M. 2012, *ApJ*, 755, L31
- Yurchenko, S. N., Barber, R. J., & Tennyson, J. 2011, *MNRAS*, 413, 1828
- Zahn, J.-P. 1992, *A&A*, 265, 115
- Zahn, J.-P., Brun, A. S., & Mathis, S. 2007, *A&A*, 474, 145
- Zapolsky, H. S., & Salpeter, E. E. 1969, *ApJ*, 158, 809